

AD-A184 254

MUTUAL ADMITTANCE BETWEEN SLOTS IN CYLINDERS OF  
ARBITRARY SHAPE(U) ILLINOIS UNIV AT URBANA COORDINATED  
SCIENCE LAB A F PETERSON ET AL AUG 87

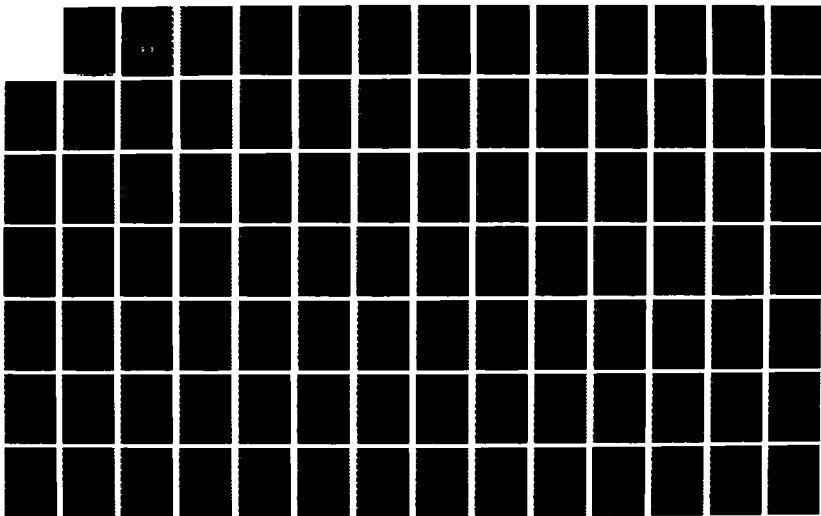
1/2

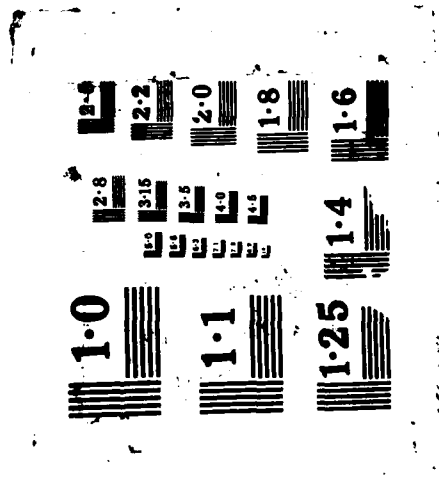
UNCLASSIFIED

UIIU-ENG-87-2247 N00014-84-C-0149

F/G 9/1

NL





August 1987

UILU-ENG-87-2247

2

**COORDINATED SCIENCE LABORATORY**  
*College of Engineering*

**DTIC FILE COPY**

**AD-A184 254**

# MUTUAL ADMITTANCE BETWEEN SLOTS IN CYLINDERS OF ARBITRARY SHAPE

**A. F. Peterson**  
**R. Mittra**

**S** DTIC  
ELECTE **D**  
SEP 10 1987  
D

**UNIVERSITY OF ILLINOIS AT URBANA-CHAMPAIGN**

Approved for Public Release. Distribution Unlimited.

**87 9 8 035**

## REPORT DOCUMENTATION PAGE

1a. REPORT SECURITY CLASSIFICATION Unclassified		1b. RESTRICTIVE MARKINGS None	
2a. SECURITY CLASSIFICATION AUTHORITY		3. DISTRIBUTION / AVAILABILITY OF REPORT Approved for public release; distribution unlimited	
2b. DECLASSIFICATION / DOWNGRADING SCHEDULE			
4. PERFORMING ORGANIZATION REPORT NUMBER(S) UILU-ENG-87-2247		5. MONITORING ORGANIZATION REPORT NUMBER(S)	
6a. NAME OF PERFORMING ORGANIZATION Coordinated Science Lab University of Illinois	6b. OFFICE SYMBOL (If applicable) N/A	7a. NAME OF MONITORING ORGANIZATION Office of Naval Research	
6c. ADDRESS (City, State, and ZIP Code) 1101 W. Springfield Ave. Urbana, IL 61801		7b. ADDRESS (City, State, and ZIP Code) 800 N. Quincy St. Arlington, VA 22217	
8a. NAME OF FUNDING / SPONSORING ORGANIZATION Joint Services Electronics Program	8b. OFFICE SYMBOL (If applicable)	9. PROCUREMENT INSTRUMENT IDENTIFICATION NUMBER N00014-84-C-0149	
8c. ADDRESS (City, State, and ZIP Code) 800 N. Quincy St. Arlington, VA 22217		10. SOURCE OF FUNDING NUMBERS	
		PROGRAM ELEMENT NO.	PROJECT NO.
		TASK NO.	WORK UNIT ACCESSION NO.
11. TITLE (Include Security Classification) Mutual Admittance Between Slots in Cylinders of Arbitrary Shape			
12. PERSONAL AUTHOR(S) Peterson, A. F. and Mitra, R.			
13a. TYPE OF REPORT Technical	13b. TIME COVERED FROM _____ TO _____	14. DATE OF REPORT (Year, Month, Day) August 1987	15. PAGE COUNT 125
16. SUPPLEMENTARY NOTATION			
17. COSATI CODES		18. SUBJECT TERMS (Continue on reverse if necessary and identify by block number) slot antennas; mutual admittance; conformal array; method of moments; integral equations	
FIELD	GROUP		
19. ABSTRACT (Continue on reverse if necessary and identify by block number)  A numerical procedure to estimate the mutual admittance between finite slots in infinite, conducting cylinders of arbitrary cross-sectional shape is described. The problem formulation involves a Fourier transform and the numerical solution of integral equations. Additional issues addressed include the large amount of required computation, remedies for non-uniqueness problems associated with the integral equations, and the overall accuracy of the procedure. Good agreement is obtained between the numerical results and exact eigenfunction data for slots in circular cylinders. Several other cylindrical shapes are investigated.			
20. DISTRIBUTION / AVAILABILITY OF ABSTRACT <input checked="" type="checkbox"/> UNCLASSIFIED/UNLIMITED <input type="checkbox"/> SAME AS RPT. <input type="checkbox"/> DTIC USERS		21. ABSTRACT SECURITY CLASSIFICATION Unclassified	
22a. NAME OF RESPONSIBLE INDIVIDUAL		22b. TELEPHONE (Include Area Code)	22c. OFFICE SYMBOL

MUTUAL ADMITTANCE BETWEEN  
SLOTS IN CYLINDERS  
OF ARBITRARY SHAPE

A. F. Peterson

R. Mitra



Accession For	
NTIS CR&I	<input checked="" type="checkbox"/>
DTIC TAB	<input type="checkbox"/>
Unannounced	<input type="checkbox"/>
Justification	
by	
Distribution	
Availability Codes	
Dist	Avail and/or Special
A-1	

TABLE OF CONTENTS

1. INTRODUCTION . . . . .	2
2. COUPLING BETWEEN AXIAL SLOTS . . . . .	9
3. COUPLING BETWEEN CIRCUMFERENTIAL SLOTS . . . . .	35
4. REMEDIATION OF THE UNIQUENESS PROBLEM ASSOCIATED WITH CERTAIN INTEGRAL EQUATIONS . . . . .	58
5. COMBINED-FIELD FORMULATION FOR COUPLING BETWEEN AXIAL AND CIRCUMFERENTIAL SLOTS . . . . .	87
6. ADMITTANCE BETWEEN SLOTS IN NONCIRCULAR CYLINDERS . . .	100
7. CONCLUSIONS AND SUGGESTED FUTURE WORK . . . . .	107
8. REFERENCES . . . . .	109
APPENDIX: SOURCE-FIELD RELATIONSHIPS FOR CYLINDERS ILLUMINATED BY AN OBLIQUELY INCIDENT FIELD . . .	112

## FIGURE CAPTIONS

- Figure 1.1 Geometry showing two axial slots and two circumferential slots in a cylinder of arbitrary shape.
- Figure 2.1 Cross section of original cylinder and flat cell model used for numerical calculations.
- Figure 2.2 Geometry of circular cylinder containing two axial slots.
- Figure 2.3 Plot of the norm of the spectral admittance function for an example involving axial slots in a cylinder of  $1.0 \lambda$  radius and slots of dimension  $W = 0.5 \lambda$ . The norm is taken with respect to the circumferential variable.
- Figure 2.4 Plot of the norm of the spectral admittance function for an axial slot example involving a  $0.7582 \lambda$  radius cylinder with slots of dimension  $W = 0.6858 \lambda$ . The norm is taken with respect to the circumferential variable.
- Figure 2.5 Plot of the condition number of the system matrix representing the MFIE for the example with cylinder radius equal to  $0.7582 \lambda$ .
- Figure 3.1 Geometry of circular cylinder containing two circumferential slots.
- Figure 3.2 Plot of the norm of the spectral admittance function for an example involving circumferential slots in a cylinder of  $1.0 \lambda$  radius and slots of dimension  $H = 0.2 \lambda$ . The norm is taken with respect to the circumferential variable.
- Figure 3.3 Plot of the matrix condition number of the system representing the longitudinal MFIE for a  $1 \lambda$  radius cylinder.
- Figure 3.4 Plot of the matrix condition number of the system representing the transverse MFIE for a  $1 \lambda$  radius cylinder.
- Figure 3.5 Plot of the norm of the spectral admittance function for an example involving circumferential slots in a cylinder of  $1.517 \lambda$  radius. Slot dimension  $H = 0.3028 \lambda$ . The norm is taken with respect to the circumferential variable.
- Figure 4.1 Plot of the three dominant eigenvalues of the TE MFIE as a function of  $k_t a$ .
- Figure 4.2 Comparison of the MFIE and exact solutions for the TE current density induced on a circular cylinder of radius  $0.3833 \lambda$ .

- Figure 4.3 Comparison of the MFIE and exact solutions for the TE current density induced on a circular cylinder of radius  $0.3828 \lambda$ .
- Figure 4.4 Comparison of the MFIE and exact solutions for the TE current density induced on a circular cylinder of radius  $0.3826 \lambda$ .
- Figure 4.5 Plot of the three dominant eigenvalues of the TE EFIE as a function of  $ka$ .
- Figure 4.6 Plot of the three dominant eigenvalues of the TE CFIE as a function of  $ka$ .
- Figure 4.7 Comparison of the CFIE and exact solutions for the TE current density induced on a circular cylinder of radius  $0.3826 \lambda$ .
- Figure 4.8 Comparison of the augmented-MFIE and exact solutions for the TE current density induced on a circular cylinder of radius  $0.3826 \lambda$ .
- Figure 4.9 Comparison of the EFIE and exact solutions for the TM current density induced on a circular cylinder of radius  $0.82$ .
- Figure 4.10 Comparison of the EFIE and exact results for the cylinder of Figure 4.9 after three interior strips were added to the 40 strip cylinder model.
- Figure 4.11 Plot of the determinant of the EFIE system matrix for the examples of Figures 4.9 and 4.10, as a function of cylinder radius.
- Figure 4.12 Circular cylinder with locations of interior strips identified.
- Figure 4.13 Plot of the determinant of the EFIE system matrix for the circular cylinder of Figure 4.12, before and after the 16 interior strips were added to the 30 strip model.
- Figure 6.1 Geometry of pie-shaped cylinder.
- Figure A.1 Geometry used for the source-field relationships.

## ABSTRACT

A numerical procedure to estimate the mutual admittance between finite slots in infinite, conducting cylinders of arbitrary cross-sectional shape is described. The problem formulation involves a Fourier transform and the numerical solution of integral equations. Additional issues addressed include the large amount of required computation, remedies for non-uniqueness problems associated with the integral equations, and the overall accuracy of the procedure. Good agreement is obtained between the numerical results and exact eigenfunction data for slots in circular cylinders. Several other cylindrical shapes are investigated.

## 1. INTRODUCTION

Both the proper design of slot arrays and the positioning of multiple antenna arrays on a common surface require an accurate estimate of the mutual coupling between individual slot elements. To date, the analysis of mutual admittance has been undertaken for slots on ground planes [1], on cones [2], [3], on circular cylinders [4]-[8], and on spherical surfaces [9]. Limited attempts have also been made to treat more general surface shapes [10], [11]. These approaches are based on analytical or asymptotic methods, and are not easily generalized to more complicated geometries. In an attempt to extend this type of analysis to arbitrary geometries, the present investigation considers a numerical solution for the mutual coupling between individual slots in an infinite, conducting cylinder of arbitrary cross-sectional shape. In general, numerical solutions involving electrically large three-dimensional structures are cumbersome and inefficient. Furthermore, trade-offs that can greatly improve the efficiency usually do so only at the expense of accuracy in the results. Therefore, one goal of the present study is to identify the degree of accuracy attainable in practice from the numerical procedure and assess the overall efficiency of the approach. Since extensive results have been tabulated for circular cylinders [5], these will be the initial foci for judging the accuracy of the method.

Two cases will be considered: coupling between two circumferential slots and coupling between two axial slots. The slots are assumed to be waveguide-fed apertures excited with the TE<sub>10</sub> waveguide mode, with no higher-order modes included in the model. (A recent investigation has included the effects of

higher-order modes and concluded that the true mutual coupling is generally slightly smaller than that predicted under the above assumption [9].) Under this assumption, the aperture field of the source slot can be expressed as

$$\bar{E} = \hat{z} \left( \frac{2}{H_A W_A} \right)^{1/2} \cos \left( \frac{\pi t}{W_A} \right) p\left(t; -\frac{W_A}{2}, \frac{W_A}{2}\right) p\left(z; -\frac{H_A}{2}, \frac{H_A}{2}\right) \quad (1.1)$$

for the circumferential slot and

$$\bar{E} = \hat{t} \left( \frac{2}{H_A W_A} \right)^{1/2} \cos \left( \frac{\pi z}{W_A} \right) p\left(t; -\frac{H_A}{2}, \frac{H_A}{2}\right) p\left(z; -\frac{W_A}{2}, \frac{W_A}{2}\right) \quad (1.2)$$

for the axial slot, where the origin of the coordinate system is located at the center of the slot, as depicted in Figure 1.1. The "pulse" functions appearing in Equations (1.1) and (1.2) explicitly truncate the support of  $\bar{E}$  to the aperture.

Under the above assumption, the mutual admittance for the circumferential case is defined

$$Y_{AB} = - \left( \frac{2}{H_B W_B} \right)^{1/2} \int_{t_0 - \frac{W_B}{2}}^{t_0 + \frac{W_B}{2}} \int_{z_0 - \frac{H_B}{2}}^{z_0 + \frac{H_B}{2}} \cos \left( \frac{\pi t'}{W_B} \right) J_z(z', t') dz' dt' \quad (1.3)$$

where the integral is taken over the aperture of slot B,  $J_z$  is the current density induced on the cylinder when slot B is short-circuited (closed by a perfect conductor) and slot A is excited by the assumed field of Equation (1.1). The variables  $z_0$  and  $t_0$  specify the distance from the center of the source slot to the center of the secondary slot. Similarly, for the axial case the mutual admittance is defined

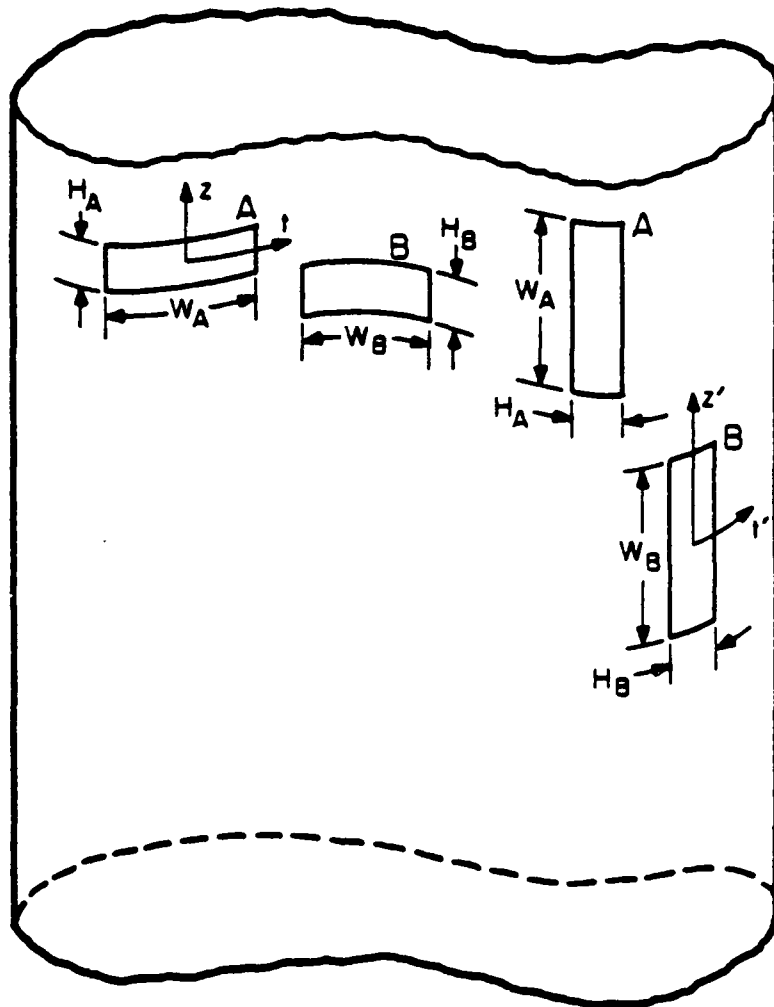


Figure 1.1 Geometry showing two axial slots and two circumferential slots in a cylinder of arbitrary shape.

$$Y_{AB} = - \left( \frac{2}{H_B W_B} \right)^{1/2} \int_{t_0 - \frac{H_B}{2}}^{t_0 + \frac{H_B}{2}} \int_{z_0 - \frac{W_B}{2}}^{z_0 + \frac{W_B}{2}} \cos \left( \frac{\pi z'}{W_B} \right) J_t(t', z') dz' dt' \quad (1.4)$$

where  $J_t$  is the transverse current density induced on the cylinder by the assumed field of Equation (1.2), with slot B short-circuited. The current densities can be found after solving for the fields of an equivalent magnetic source defined

$$\bar{K}_{eq} = \bar{E} \times \hat{n} \quad (1.5)$$

For the circumferential slot field of Equation (1.1),

$$\bar{K}_{eq} = \hat{t} K_t = \hat{t} \left( \frac{2}{H_A W_A} \right)^{1/2} \cos \left( \frac{\pi t}{W_A} \right) p\left(t; -\frac{W_A}{2}, \frac{W_A}{2}\right) p\left(z; -\frac{H_A}{2}, \frac{H_A}{2}\right) \quad (1.6)$$

For the axial slot field of Equation (1.2),

$$\bar{K}_{eq} = \hat{z} K_z = -\hat{z} \left( \frac{2}{H_A W_A} \right)^{1/2} \cos \left( \frac{\pi z}{W_A} \right) p\left(t; -\frac{H_A}{2}, \frac{H_A}{2}\right) p\left(z; -\frac{W_A}{2}, \frac{W_A}{2}\right) \quad (1.7)$$

These equivalent magnetic currents, radiating in the presence of the infinite cylinder, produce the same exterior fields and currents as the original slot with aperture fields described by Equations (1.1) and (1.2). Thus, the problem of computing the mutual coupling between slots A and B reduces to that of finding the currents induced upon a closed, infinite conducting cylinder by a finite impressed source  $\bar{K}_{eq}$ . Once these currents are found, the mutual admittance between slot A and any other slot location can be computed using Equations (1.3) and (1.4).

To simplify the task of determining the currents induced upon an infinite cylinder by a finite source, the problem can be posed in the Fourier transform domain. The Fourier transform is defined

$$F_z \{H(z)\} = \tilde{H}(\gamma) = \int_{-\infty}^{\infty} H(z) e^{-j\gamma z} dz \quad (1.8)$$

The inverse Fourier transform is

$$F_z^{-1} \{\tilde{H}(\gamma)\} = H(z) = \frac{1}{2\pi} \int_{-\infty}^{\infty} \tilde{H}(\gamma) e^{j\gamma z} d\gamma \quad (1.9)$$

Applied to the unknown currents, the Fourier transform converts functions of 'z' to functions of the transform variable 'γ.' Because the cylinder is invariant with respect to z, the unknown current density at each value of γ can be found independently. Thus, the original three-dimensional problem reduces to the superposition of uncoupled two-dimensional problems, which are more amenable to numerical solution.

In spite of the simplification resulting from the decoupling of the equations mentioned above, we are still faced with the task of solving the two-dimensional problem over the infinite continuum spanned by the variable γ. In practice, we are forced to work with a finite number of discrete values of the spatial frequency, i.e.,  $\gamma_0, \gamma_{\pm 1}, \dots, \gamma_{\pm N}$ . As is well known from signal analysis [12], when a Fourier transform is combined with an evenly-spaced sampling process, the result is equivalent to working with the Fourier transform of a periodic extension of the original function of z. We can think of the above approach as being equivalent to replacing the original problem (which involved a single source slot) by one involving a periodic array of source slots. This

analogy allows a better grasp of the approximations introduced by sampling in the transform domain.

The period of the fictitious source array must be sufficiently large so that the coupling between the fictitious slots and slot B will be insignificant compared to the coupling from slot A to slot B. In addition, discrete values of  $\gamma$  must be included up to the point where truncation does not introduce numerical inaccuracy. After solving for the transform currents over a sufficient range of  $\gamma$ , the inverse transform can be computed explicitly according to

$$J(t, z) = \frac{\Delta\gamma}{2\pi} [\tilde{J}(t, 0) + 2 \sum_{n=1}^N \tilde{J}(t, n \Delta\gamma) \cos(n \Delta\gamma z)] \quad (1.10)$$

to produce the spatial currents at the desired locations for the admittance calculation. In Equation (1.10), we have assumed that the original source distribution is centered at  $z=0$  and is symmetric in  $z$ .

Although the current density can be computed directly according to Equation (1.10), the admittance calculations of Equations (1.3) and (1.4) are actually convolutions in the variable  $z$ . Therefore, the  $z$ -integrations required for the admittance calculation can be performed by an additional multiplication in the Fourier transform domain, prior to inverse transformation. One advantage of this alternative procedure is that one numerical integration is eliminated from the computation of  $Y_{AB}$ . A second advantage is that the additional multiplicative factor in the transform domain helps to dampen the higher spatial frequencies and speed the convergence of the inverse Fourier transformation.

In summary, we have posed the mutual coupling problem in an arbitrarily-shaped cylinder in such a manner as to make it amenable to numerical solution.

The equivalence theorem is used to replace the source slot by magnetic currents radiating in the presence of the closed cylinder. The desired three-dimensional problem can be represented by the superposition of two-dimensional problems via the Fourier transform. The equations can be discretized directly in the transform domain, which introduces a fictitious periodicity in the spatial domain. However, the formulation does require that the two-dimensional problem be solved at a number (perhaps a large number depending on the relative location of the source and secondary slot) of spatial frequencies. The extent of the necessary spectrum, the period size, and other aspects concerning the modeling procedure will be determined by numerical experimentation.

In order to implement the above procedure, it is necessary to solve the associated two-dimensional scattering problems at each of the spatial frequencies required. Initially, we consider a numerical solution of the magnetic-field integral equation (MFIE). Chapter 2 describes the MFIE formulation for axial slot coupling, and a similar formulation for circumferential slot coupling is presented in Chapter 3. Unfortunately, the MFIE fails at certain spatial frequencies throughout the range of interest, as preliminary results indicate. Chapter 4 presents a detailed discussion of this problem and considers several remedies. One such remedy involves the combined-field integral equation (CFIE). Results from using a CFIE formulation for both axial and circumferential slots are presented in Chapter 5. Use of the CFIE appears to eradicate the problems associated with the MFIE, but at the expense of additional computational overhead. Good agreement is obtained between the CFIE results and exact eigenfunction values for slots in circular cylinders. Chapter 6 presents additional admittance data for slots in noncircular cylinders.

## 2. COUPLING BETWEEN AXIAL SLOTS

### 2.1 Formulation

The framework for constructing a numerical solution for the mutual admittance between slots was developed in Chapter 1. The remaining task is to find the electric current density induced in the vicinity of the secondary slot by the equivalent magnetic current representing the source slot. For axial slots, only the transverse electric current density  $J_c$  is required for the admittance calculation. A suitable equation for the transverse electric current density is the magnetic field integral equation (MFIE), which enforces the boundary condition that the total magnetic field at the surface of the cylinder is proportional to the electric surface current density according to

$$\hat{n} \times \bar{H} = \bar{J} \quad (2.1)$$

The MFIE can be expressed

$$H_z^{inc}(t, z) = -J_c(t, z) - \hat{z} \cdot \text{curl} \int \hat{e}(t') J_c(t', z') \frac{e^{-jkR}}{4\pi R} dt' dz' \quad (2.2)$$

where

$$R = \sqrt{[x(t) - x(t')]^2 + [y(t) - y(t')]^2 + (z - z')^2} \quad (2.3)$$

and where  $H_z^{inc}$  represents the  $\hat{z}$ -component of the magnetic field produced by the equivalent magnetic current  $K_z$  if the magnetic current was radiating in free space. Equation (2.2) is a convolution in the variable  $z$ , and an application of the Fourier transform in conjunction with the convolution theorem [12] yields

$$\tilde{H}_z^{inc}(t, \gamma) = -\tilde{J}_c(t, \gamma) - \hat{z} \cdot \text{curl} \int \hat{e}(t') \tilde{J}_c(t', \gamma) \tilde{G}(\rho; k, \gamma) dt' \quad (2.4)$$

where [13]

$$\tilde{G}(\rho; k, \gamma) = F_z \left\{ \frac{e^{-jk\sqrt{\rho^2+z^2}}}{4\pi\sqrt{\rho^2+z^2}} \right\}$$

$$= \begin{cases} \frac{1}{4j} H_0^{(2)}(\rho\sqrt{k^2-\gamma^2}) & k^2 > \gamma^2 \\ \frac{1}{2\pi} K_0(\rho\sqrt{\gamma^2-k^2}) & \gamma^2 > k^2 \end{cases} \quad (2.5)$$

and

$$\rho = \sqrt{[x(t) - x(t')]^2 + [y(t) - y(t')]^2} \quad (2.6)$$

Equation (2.4) is identical in form to the conventional two-dimensional integral equation for scattering from a conducting cylinder, with the exception that the wavenumber  $k$  has been replaced by

$$k_t = \begin{cases} \sqrt{k^2-\gamma^2} & k^2 > \gamma^2 \\ -j\sqrt{\gamma^2-k^2} & \gamma^2 > k^2 \end{cases} \quad (2.7)$$

The incident magnetic field can be computed from the expression

$$\tilde{H}_z^{\text{inc}}(t, \gamma) = \frac{k^2 - \gamma^2}{jk\eta} \int_{\text{slotA}} \tilde{K}_z(t', \gamma) \tilde{G}(\rho; k, \gamma) dt' \quad (2.8)$$

where  $\eta$  is the intrinsic impedance of free space,  $\rho$  is defined in Equation (2.6), and  $\tilde{K}_z$  is the Fourier transform of Equation (1.7).

The preceding discussion introduced the idea of replacing the original source slot by a periodic repetition of slots, in order to discretize the transform domain. If the spatial period is  $P_z$ , the sampling interval in the transform domain is fixed at

$$\Delta\gamma = \frac{2\pi}{P_z} \quad (2.9)$$

Equation (2.4) can be solved approximately by converting it to a matrix equation of finite order, using the method of moments [14],[15]. This procedure is illustrated in the following section.

## 2.2 Numerical Solution of the Two-Dimensional Magnetic Field Integral Equation

Equation (2.4) can be solved approximately by converting it to a matrix equation of finite order, using a method of moments [14],[15]. The cylindrical cross-section can be modeled by the superposition of flat strip-cells, as illustrated in Figure 2.1. For convenience, we assume that slot A can be modeled by a small number of the same cells. Each cell in the model can be described by its phase center  $(x,y)$ , its cross-sectional length 'w,' and an orientation angle ' $\Omega$ ' defining the outward normal vector according to

$$\hat{n} = \hat{x} \cos \Omega + \hat{y} \sin \Omega \quad (2.10)$$

If pulse basis functions are used to represent the surface current density  $J_t$ , and Equation (2.4) is enforced at the center of each of the cells in the model, the result is a matrix equation of the form

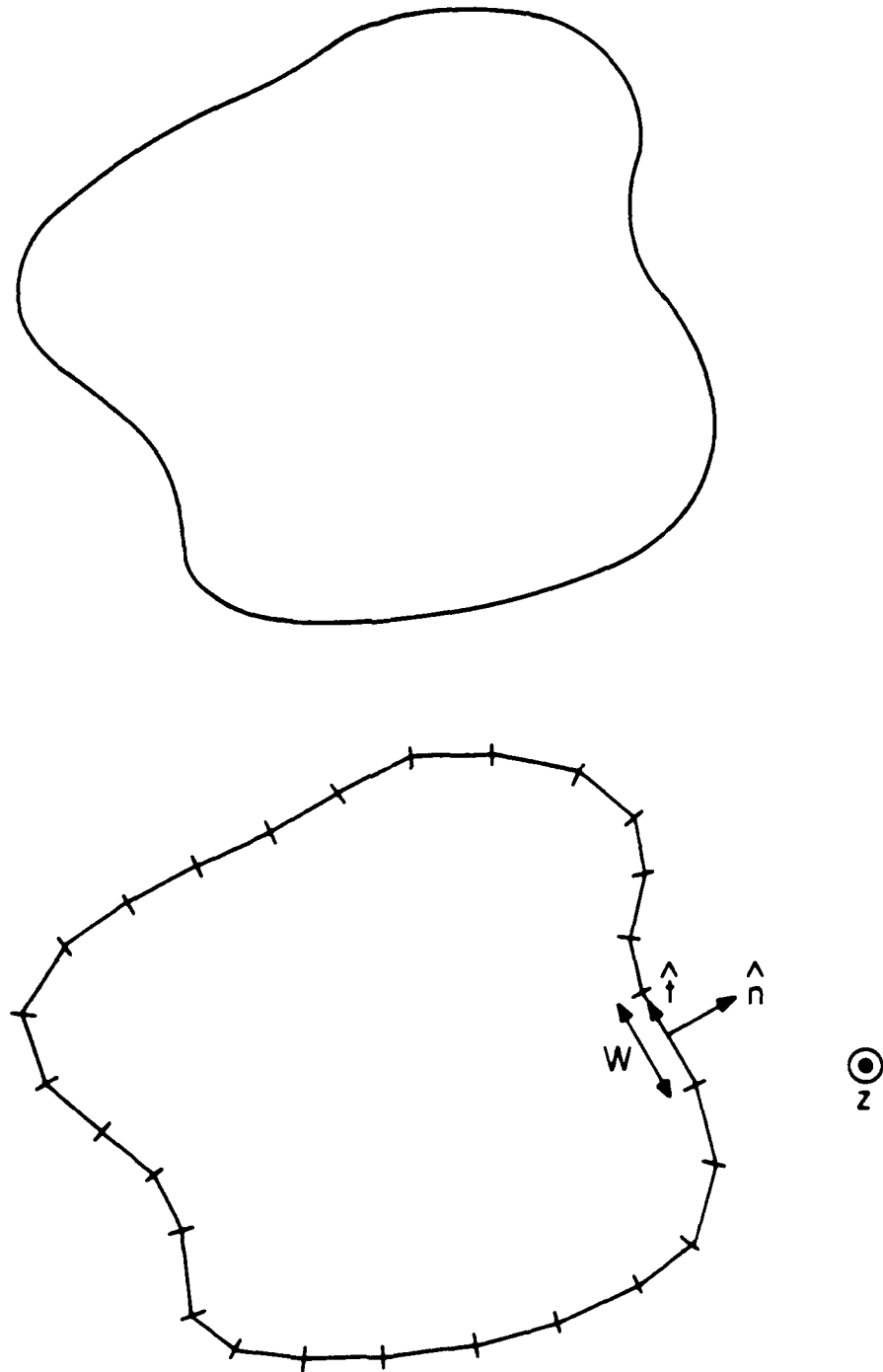


Figure 2.1 Cross section of original cylinder and flat cell model used for numerical calculations.

$$\begin{bmatrix} z_{11} & z_{12} & & \\ & z_{21} & z_{22} & \\ & & \vdots & \\ & & & z_{NN} \end{bmatrix} \begin{bmatrix} j_t^1 \\ j_t^2 \\ \vdots \\ j_t^N \end{bmatrix} = \begin{bmatrix} h_1 \\ h_2 \\ \vdots \\ h_N \end{bmatrix} \quad (2.11)$$

General expressions for source-field relationships are derived in Appendix A, and can be used to construct the matrix elements

$$z_{ii} = -\frac{1}{2} \quad (2.12)$$

$$\begin{aligned} z_{in} = & -\int_{s=-\frac{W_n}{2}}^{\frac{W_n}{2}} \left[ \cos \Omega_n \frac{\Delta x}{R} \right. \\ & \left. + \sin \Omega_n \frac{\Delta y}{R} \right] \tilde{G}'(R; k, \gamma) ds \quad i \neq n \end{aligned} \quad (2.13)$$

where

$$\Delta x = x_i + s \sin \Omega_n \quad (2.14)$$

$$\Delta y = y_i - s \cos \Omega_n \quad (2.15)$$

$$R = \sqrt{\Delta x^2 + \Delta y^2}$$

and

$$\tilde{G}'(R; k, \gamma) = \begin{cases} -\frac{\sqrt{k^2 - \gamma^2}}{4j} H_1^{(2)}(R \sqrt{k^2 - \gamma^2}) & k^2 > \gamma^2 \\ -\frac{\sqrt{\gamma^2 - k^2}}{2\pi} K_1(R \sqrt{\gamma^2 - k^2}) & \gamma^2 > k^2 \end{cases} \quad (2.17)$$

Since closed-form expressions for the integrals of the type appearing in Equation (2.13) are not often available, some form of numerical integration is necessary to accurately evaluate the elements of the moment-method matrix. In this case, many of the matrix elements can be accurately determined by single-point integration. For those elements of the matrix representing closely spaced cells, experimentation determined that single-point evaluation does not produce accurate enough numbers. A Romberg integration algorithm [16] was used to compute the closely-spaced terms. Since the slot excitation is assumed to be constant in the variable  $t$ , the right-hand side is given by

$$h_i = \tilde{V} \sum_{n=1}^{N_A} h_{in} \quad (2.18)$$

where, from Appendix A we have

$$h_{ii} = \frac{-(k^2 - \gamma^2)}{4k\eta} W_i \left\{ \begin{array}{l} 1 - j \frac{2}{\pi} \ln \left( \frac{|k_t| W_i}{6.10482} \right) \quad \gamma^2 \\ - j \frac{2}{\pi} \ln \left( \frac{|k_t| W_i}{6.10482} \right) \quad \gamma^2 > k^2 \end{array} \right. \quad (2.19)$$

and, for  $i \neq n$ ,

$$h_{in} = \frac{-(k^2 - \gamma^2)}{4k\eta} W_n \left\{ \begin{array}{l} H_0^{(2)}(R \sqrt{k^2 - \gamma^2}) \quad k^2 > \gamma^2 \\ j \frac{2}{\pi} K_0(R \sqrt{\gamma^2 - k^2}) \quad \gamma^2 > k^2 \end{array} \right. \quad (2.20)$$

$\tilde{V}$  is the Fourier transform of Equation (1.7) and is given by

$$\tilde{V}(\gamma) = \begin{cases} -\sqrt{\frac{2}{H_A W_A}} W_A \cos\left(\frac{\gamma W_A}{2}\right) \left[\frac{1}{\pi - W_A \gamma} + \frac{1}{\pi + W_A \gamma}\right], & W_A \gamma \neq \pm \pi \\ -\sqrt{\frac{2}{H_A W_A}} \frac{W_A}{2}, & W_A \gamma = \pm \pi \end{cases} \quad (2.21)$$

Note that Equation (2.21) is an even-symmetric function of  $\gamma$ .

In order to simplify the admittance calculation as much as possible, the  $z$ -integration in Equation (1.4) can be performed analytically in the Fourier transform domain. This requires that we weigh the spectrum by an additional factor  $\tilde{W}(\gamma)$ . For axial slots,  $\tilde{W}(\gamma)$  represents the transform of the cosine function from Equation (1.4), and is given as

$$\tilde{W}(\gamma) = \begin{cases} W_B \cos\left(\frac{\gamma W_B}{2}\right) \left[\frac{1}{\pi - W_B \gamma} + \frac{1}{\pi + W_B \gamma}\right], & W_B \gamma \neq \pm \pi \\ \frac{W_B}{2}, & W_B \gamma = \pm \pi \end{cases} \quad (2.22)$$

Both  $\tilde{W}$  and  $\tilde{V}$  are even-symmetric functions of  $\gamma$ , and therefore it is only necessary to work with the positive part of the spectrum. Thus,  $\gamma$  will range from 0 to  $N\Delta\gamma$ , in intervals of  $\Delta\gamma$ . The product of the two-dimensional current density as a function of spatial frequency, the excitation  $\tilde{V}(\gamma)$ , and the additional weighting factor  $\tilde{W}(\gamma)$  will be named the "spectral admittance function"  $\tilde{Y}(t, \gamma)$ . The inverse Fourier transform of  $\tilde{Y}$ , according to

$$Y(t) = \frac{\Delta Y}{2\pi} \left[ \tilde{Y}(t, \gamma) + 2 \sum_{n=1}^N \tilde{Y}(t, n\Delta\gamma) \cos(n\Delta\gamma z) \right] \quad (2.23)$$

produces a spatial admittance function  $Y(t)$ . The admittance between two slots is then found from

$$Y_{AB} = - \left[ \frac{2}{H_B W_B} \right]^{1/2} \int_{t_0 - \frac{W_B}{2}}^{t_0 + \frac{W_B}{2}} Y(t') dt' \quad (2.24)$$

Equation (2.11) must be solved over the range spanned by the transform variable  $\gamma$ . In theory, this range extends from  $-\infty$  to  $+\infty$ , although in practice it is truncated at some finite value. The portion of the spectrum where  $\gamma^2 < k^2$  is known as the "visible region." Throughout the visible region, Equation (2.11) is complex-valued. However, for  $\gamma^2 > k^2$  (the "invisible" region of the spectrum), the matrix elements of Equation (2.11) are real-valued. Thus, for  $\gamma^2 > k^2$ , a significant computational savings can be obtained by treating Equation (2.11) as a real-valued system.

### 2.3 Preliminary Numerical Results

There are three types of "convergence" to be evaluated by numerical experimentation. The first concerns the inverse Fourier transform: How much of the spectrum is necessary when computing Equation (2.23)? In general, this will be a function of the axial dimension of the slots, since the weighting factors  $\tilde{V}(\gamma)$  and  $\tilde{W}(\gamma)$  appearing in Equations (2.21) and (2.22) are both functions of slot dimension. Thus, it may be necessary to include more of the spectrum when computing coupling between shorter slots. The second type of convergence concerns the fictitious periodicity introduced through sampling in the Fourier transform domain: How large does the period have to be to accurately represent a single

source slot? The period will be a function of slot spacing, i.e., a larger period will be necessary when treating larger slot spacings. The third type of convergence involves the numerical solution of the integral equation: How many expansion functions are needed to ensure accurate results?

In an attempt to answer these questions, we consider an example involving axial slots in circular cylinders. Admittance data based upon eigenvalue solutions (available only when the cylinder is circular in shape) have been tabulated [5]. By comparing these data to numerical results, the necessary spectrum and period size can be ascertained. The numerical solution to integral equations has been studied for many years, and a considerable amount of experience suggests that approximately 10 expansion functions per wavelength are required for meaningful results. We will consider the effect of different cell densities in this range.

The initial example involves a circular cylinder with radius equal to one wavelength, containing axial slots of dimensions  $0.2 \times 0.5$  wavelength. The cylinder geometry is shown in Figure 2.2. Table 2.1 shows values of the admittance between slots of different spacings, taken from Reference [5]. These are based upon an eigenfunction analysis, and are the values that should be produced by the numerical approach under ideal circumstances (exact solutions to the integral equation, infinite period, and no truncation of the spectrum). Thus, we will use Table 2.1 as a reference for comparison.

A computer code was developed in FORTRAN to compute the mutual admittance between axial slots, using the procedure discussed above. This program requires that the cylinder geometry be specified in terms of discrete cells, as illustrated

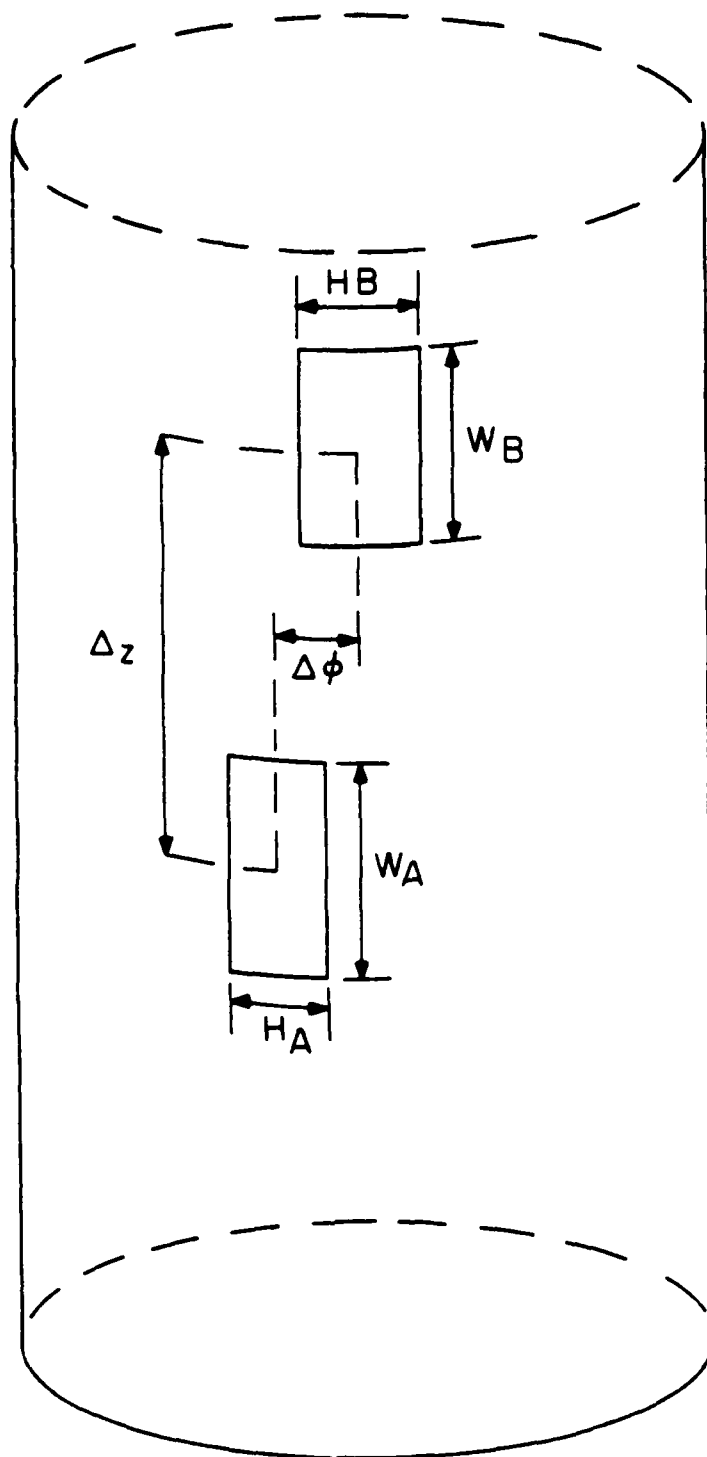


Figure 2.2 Geometry of circular cylinder containing two axial slots.

TABLE 2.1

Eigenfunction solution for the mutual admittance between slots in a cylinder with radius equal to one wavelength. The slots are axial with dimensions  $W = 0.5$  wavelength,  $H = 0.2$  wavelength. The admittance is given in magnitude (decibels) and phase angle (degrees). Taken from Reference [5].

$\Delta z$	$\Delta\phi$	$Y_{AB}$ in dB
$1\lambda$	0	- 87.1 / <u>- 171°</u>
$2\lambda$	0	- 100.0 / <u>- 174°</u>
$4\lambda$	0	- 112.4 / <u>- 175°</u>
$8\lambda$	0	- 124.3 / <u>- 174°</u>
$1\lambda$	$45^\circ$	- 89.2 / <u>2°</u>

in Figure 2.1. For the cylinder of one wavelength radius, consider the use of 88 equal-sized cells to represent the model. This satisfies the 10 cells per wavelength requirement. Although not absolutely necessary, for convenience we represent the source and secondary slot in terms of the same model as the cylinder. In this case, the choice of 88 equal-sized cells constrains the height of the slots to 0.214 wavelength (three cells) instead of 0.200 wavelength. This could be alleviated by the use of non-equal cell sizes, but the difference here is considered slight. (In order to easily treat situations where the source and secondary slot are separated in both the axial and circumferential directions, it may be necessary to use non-equal cell sizes throughout the model.) In this case, the choice of 88 equal-sized cells allows us to treat a circumferential separation of 0 and 45 degrees.

Results for the mutual admittance based on the 88 cell model are tabulated in Tables 2.2 through 2.5. Table 2.6 shows a comparison of results from a 63 cell model (equal-sized cells) with those from the 88 cell model and the eigenfunction data. The results from the 88 cell model appear to be more accurate than those of the 63 cell model. In general, there is excellent agreement between the numerical and eigenfunction results. For slots that are closely spaced in  $z$ , the accuracy does not appear to improve much as the period size is increased. For slots that are separated by several wavelengths along the cylinder axis, the results appear to improve as the fictitious period size is increased.

To determine the necessary spectrum for inverse Fourier transformation, Figure 2.3 shows the spectral admittance function as a function of the transform variable  $\gamma$ . This figure suggests that the spectrum contains little information

TABLE 2.2

Numerical results for the mutual admittance between axial slots as a function of period size and spectrum truncation. The circular cylinder has  $1\lambda$  radius and is modeled with 88 cells. Slot separation:  $\Delta z = 1\lambda$ ,  $\Delta\phi = 0^\circ$  (MFIE solution) The admittance is given in magnitude (decibels) and angle (degrees). Both slots are axial with dimensions  $H = 0.214$  and  $W = 0.5$  wavelength.

$P_z$	$\gamma_{\max} \approx 20$	$\gamma_{\max} \approx 30$
$20.5\lambda$	- 86.59 / <u>-169.0</u>	- 86.63 / <u>-170.3</u>
$40.5\lambda$	- 86.93 / <u>-168.6</u>	- 86.97 / <u>-170.0</u>
$80.5\lambda$	- 86.90 / <u>-168.7</u>	- 86.94 / <u>-170.0</u>

TABLE 2.3

Numerical results for the mutual admittance between axial slots as a function of period size and spectrum truncation. The circular cylinder has  $1\lambda$  radius and is modeled with 88 cells. Slot separation:  $\Delta z = 2\lambda$ ,  $\Delta\phi = 0^\circ$  (MFIE solution) The admittance is given in magnitude (decibels) and angle (degrees). Both slots have  $H = 0.214$  and  $W = 0.5$  wavelength.

$P_z$	$\gamma_{\max} = 20$	$\gamma_{\max} = 30$
$20.5\lambda$	- 100.86 / <u>-172.6</u>	- 100.85 / <u>-171.7</u>
$40.5\lambda$	- 99.59 / <u>-172.7</u>	- 99.58 / <u>-172.5</u>
$80.5\lambda$	- 99.24 / <u>-172.9</u>	- 99.23 / <u>-172.5</u>

TABLE 2.4

Numerical results for the mutual admittance between axial slots as a function of period size and spectrum truncation. The circular cylinder has  $1\lambda$  radius and is modeled with 88 cells. Slot separation:  $\Delta z = 4\lambda$ ,  $\Delta\phi = 0^\circ$  (MFIE solution) The admittance is given in magnitude (decibels) and angle (degrees). Both slots have  $H = 0.214$  and  $W = 0.5\lambda$ .

$P_z$	$\gamma_{\max} = 20$	$\gamma_{\max} = 30$
$20.5\lambda$	- 111.33 / <u>-179.9</u>	- 111.31 / <u>-175.7</u>
$40.5\lambda$	- 109.74 / <u>-177.9</u>	- 109.70 / <u>-174.2</u>
$80.5\lambda$	- 110.96 / <u>-178.8</u>	- 110.92 / <u>-174.3</u>

TABLE 2.5

Numerical results for the mutual admittance between axial slots as a function of period size and spectrum truncation. The circular cylinder has  $1\lambda$  radius and is modeled with 88 cells. Slot separation:  $\Delta z = 1\lambda$ ,  $\Delta\phi = 45^\circ$  (MFIE solution). The admittance is given in magnitude (decibels) and angle (degrees). Both slots have  $H = 0.214\lambda$  and  $W = 0.5\lambda$ .

$P_z$	$\gamma_{\max} = 20$	$\gamma_{\max} = 30$
20.5 $\lambda$	- 88.97 / <u>1.7</u>	- 88.97 / <u>1.7</u>
40.5 $\lambda$	- 88.81 / <u>1.8</u>	- 88.81 / <u>1.8</u>
80.5 $\lambda$	- 88.83 / <u>1.8</u>	- 88.83 / <u>1.8</u>

TABLE 2.6

A comparison of the numerical results for the mutual admittance between axial slots for different models of the cylinder. The circular cylinder has  $1\lambda$  radius. The period is  $40.5\lambda$  and the spectrum is truncated at  $\gamma = 20$ . All slot separations involve  $\Delta\phi = 0^\circ$  (MFIE solution). The admittance is given in magnitude (decibels) and angle (degrees). Both slots have  $H = 0.214\lambda$  and  $W = 0.5\lambda$ .

$\Delta z$	63 cell model	88 cell model	eigenfunction
$1\lambda$	- 87.67 / <u>-167.1</u>	- 86.93 / <u>-168.7</u>	- 87.1 / <u>-171</u>
2	- 100.27 / <u>-171.9</u>	- 99.59 / <u>-172.7</u>	- 100.0 / <u>-174</u>
4	- 109.61 / <u>-178.0</u>	- 109.74 / <u>-177.9</u>	- 112.4 / <u>-175</u>
8	- 120.88 / <u>-2.8</u>	- 125.34 / <u>-6.3</u>	- 124.3 / <u>-174</u>

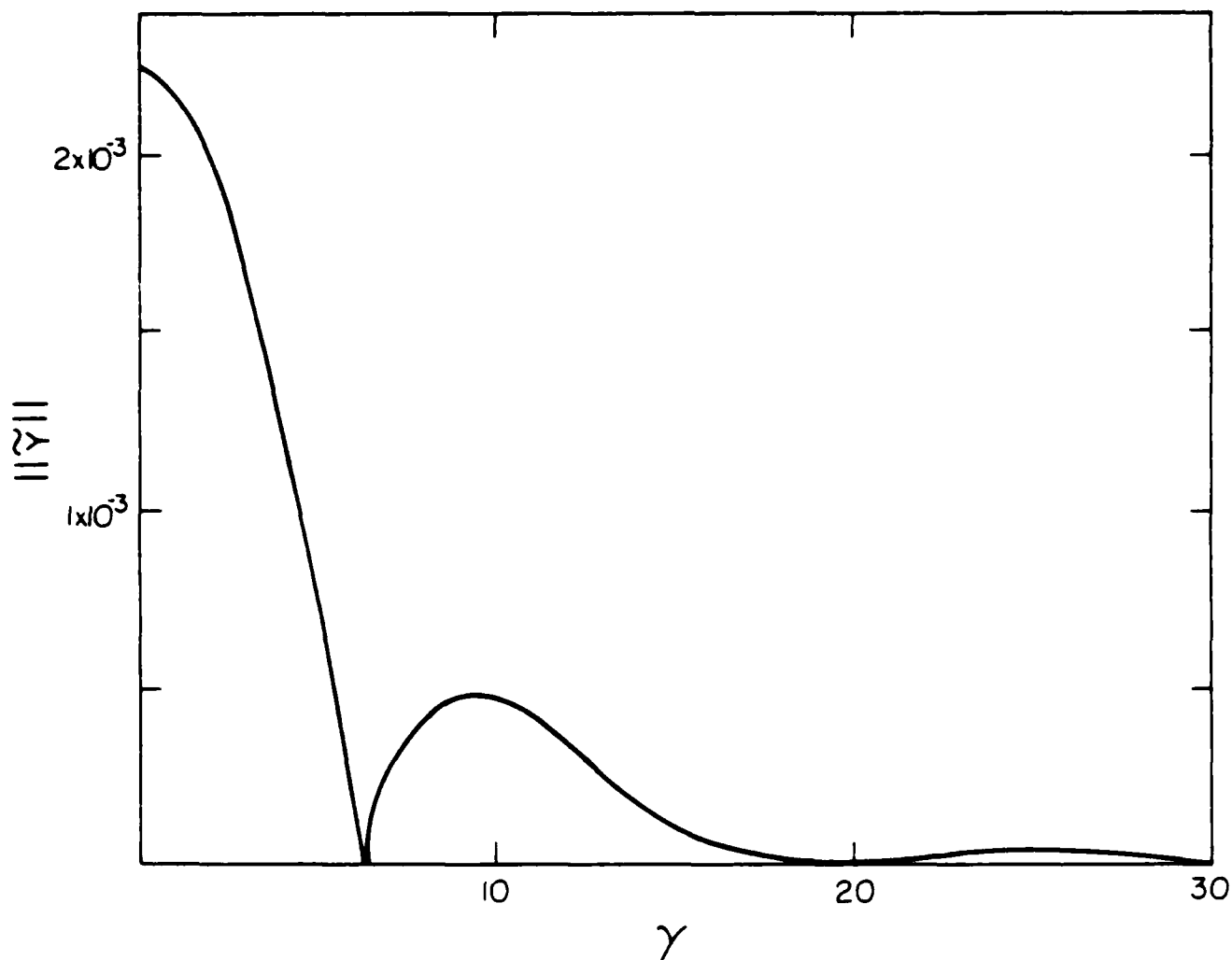


Figure 2.3 Plot of the norm of the spectral admittance function for an example involving axial slots in a cylinder of  $1.0 \lambda$  radius and slots of dimension  $W = 0.5 \lambda$ . The norm is taken with respect to the circumferential variable.

beyond  $\gamma = 20$ . In Tables 2.2 through 2.5, admittance results are presented for the case when the spectrum is truncated at  $\gamma = 20$  and  $\gamma = 30$ . For this example, it is apparent that the additional spectrum causes virtually no change in the calculated admittance values.

To summarize the findings of this initial example, it appears that a cylinder model containing a cell density of about 10 cells per wavelength yields accurate enough solutions to the MFIE for our purpose. Furthermore, for this example the spectrum could be truncated at  $\gamma = 20$  without significant error. It also appears that for slots spaced within several wavelengths in  $z$ , the period size need not be more than 40 wavelengths for reliable solutions. However, for slot spacings greater than 4 wavelengths in  $z$ , we observe poor phase accuracy (see Table 2.6). This may be a result of insufficient period size for that separation. We also observe that the convergence in  $\gamma$  (i.e., the convergence of the admittance for different truncations of the spectrum) is much faster when there is a nonzero  $\Delta\phi$  separation.

Consider an example involving a circular cylinder with radius 0.7582 wavelength. Slot dimensions are  $0.3048 \times 0.6858$  wavelength. A cylinder model consisting of 47 equal-sized cells satisfies the "10 cells per wavelength" condition discussed above. In addition, if the slots are modeled by three adjacent cells, the 47 cell model yields a slot dimension in the model of  $0.3041 \times 0.6858$ , which is reasonably close to the desired size.

Data for the mutual admittance between axial slots for different slot separations are presented in Tables 2.7 to 2.9. Eigenfunction results are only available for one of these cases, that displayed in Table 2.9. The accuracy of

TABLE 2.7

Numerical results for the mutual admittance between axial slots as a function of period size and spectrum truncation. The circular cylinder has radius equal to  $0.7582\lambda$  and is modeled with 47 cells. The slots have  $H = 0.3041\lambda$  and  $W = 0.6858\lambda$ . Slot separation:  $\Delta\phi = 0$ ,  $\Delta z = 1.524\lambda$ . The admittance is given in magnitude (decibels) and angle (degrees). (MFIE solution)

$P_z$	$\gamma_{\max} = 20$	$\gamma_{\max} = 30$
$20.5\lambda$	- 93.02 / <u>14.5</u>	- 93.17 / <u>9.9</u>
$40.5\lambda$	- 95.75 / <u>14.6</u>	- 95.96 / <u>7.6</u>
$80.5\lambda$	- 90.85 / <u>11.3</u>	- 90.95 / <u>7.6</u>

TABLE 2.8

Numerical results for the mutual admittance between axial slots as a function of period size and spectrum truncation. The circular cylinder has radius equal to  $0.7582$  wavelength and is modeled with 47 cells. The slots have  $H = 0.3041\lambda$  and  $W = 0.6858\lambda$ . Slot separation:  $\Delta\phi = 0$ ,  $\Delta z = 3.048\lambda$ . The admittance is given in magnitude (decibels) and angle (degrees). (MFIE solution)

$P_z$	$Y_{\max} = 20$	$Y_{\max} = 30$
$20.5\lambda$	- 107.02 / <u>163.2</u>	- 107.35 / <u>173.7</u>
$40.5\lambda$	- 102.33 / <u>176.8</u>	- 102.34 / <u>-178.3</u>
$80.5\lambda$	- 114.25 / <u>142.8</u>	- 115.88 / <u>163.8</u>

TABLE 2.9

Numerical results for the mutual admittance between axial slots as a function of period size and spectrum truncation. The circular cylinder has radius equal to 0.7582 wavelength and is modeled with 47 cells. The slots have  $H = 0.3041\lambda$  and  $W = 0.6858\lambda$ . Slot separation:  $\Delta\phi = 0$ ,  $\Delta z = 6.096\lambda$ . The admittance is given in magnitude (decibels) and angle (degrees). (MFIE solution) The eigenfunction value of admittance for this slot separation is  $-118.1 / \underline{150^\circ}$ .

$P_z$	$Y_{\max} = 20$	$Y_{\max} = 30$
20.5 $\lambda$	- 109.92 / <u>15.5</u>	- 109.84 / <u>17.3</u>
40.5 $\lambda$	- 102.02 / <u>14.7</u>	- 101.91 / <u>17.1</u>
80.5 $\lambda$	- 111.74 / <u>165.6</u>	- 111.57 / <u>161.7</u>

the numerical results displayed in Table 2.9 is not good. In addition, for all of these slot separations the admittance values do not seem to stabilize as the period size is increased, although truncating the spectrum at  $\gamma = 20$  seems to be adequate. The spectral admittance function is shown in Figure 2.4, and also suggests that truncation at  $\gamma = 20$  is sufficient.

In an attempt to explain the instability of the admittance values with increasing period  $P_z$ , the condition number of the matrix equation solved at each of the spatial frequencies is displayed in Figure 2.5. Near two spatial frequencies in the range of interest, the matrix equation becomes very ill-conditioned. This behavior is characteristic of a problem with the integral equation formulation for this example. It is known that unique solutions exist to the MFIE except at spatial frequencies where cavity resonances can occur [17], [18], and at those frequencies the moment-method matrix will fail to represent the desired scattering problem. For a circular cylinder geometry, these frequencies are related to the resonance frequencies of circular cavities. In fact, for this particular example, the theoretical resonance frequencies occur when  $\gamma = 3.73$  and  $\gamma = 5.42$ . Thus, ill-conditioning is observed in the matrix at exactly the spatial frequencies where cavity resonances are theoretically predicted to occur.

It is interesting that the first example appeared to produce accurate, stable results, in spite of the fact that it theoretically suffers from similar "internal resonance" problems. It seems that the uniqueness problem will not arise unless the sample points in  $\gamma$  coincide almost exactly with the "resonant" spatial frequencies. Apparently, only some examples will be affected by this problem.

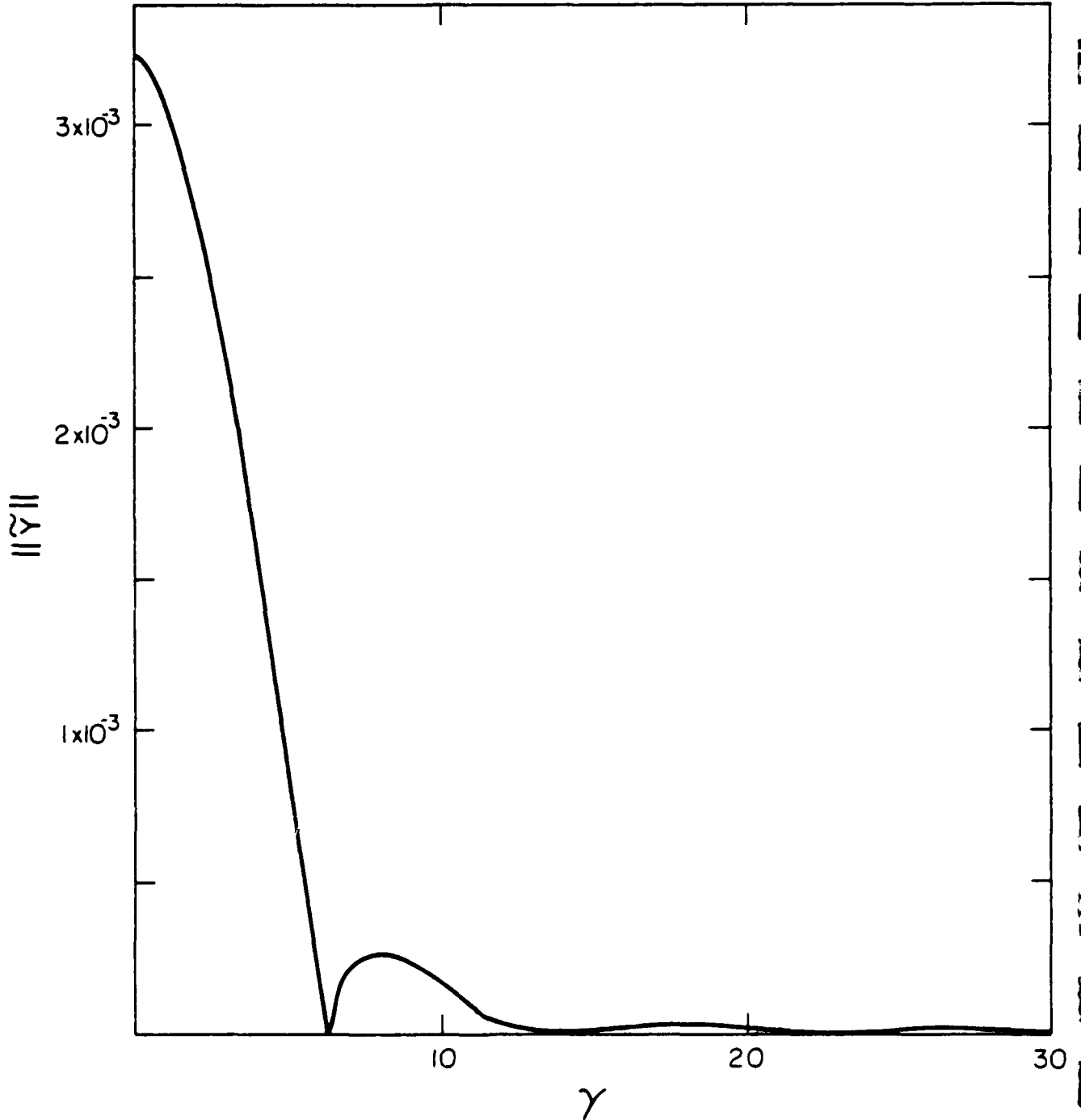


Figure 2.4

Plot of the norm of the spectral admittance function for an axial slot example involving a  $0.7582 \lambda$  radius cylinder with slots of dimension  $W = 0.6858 \lambda$ . The norm is taken with respect to the circumferential variable.

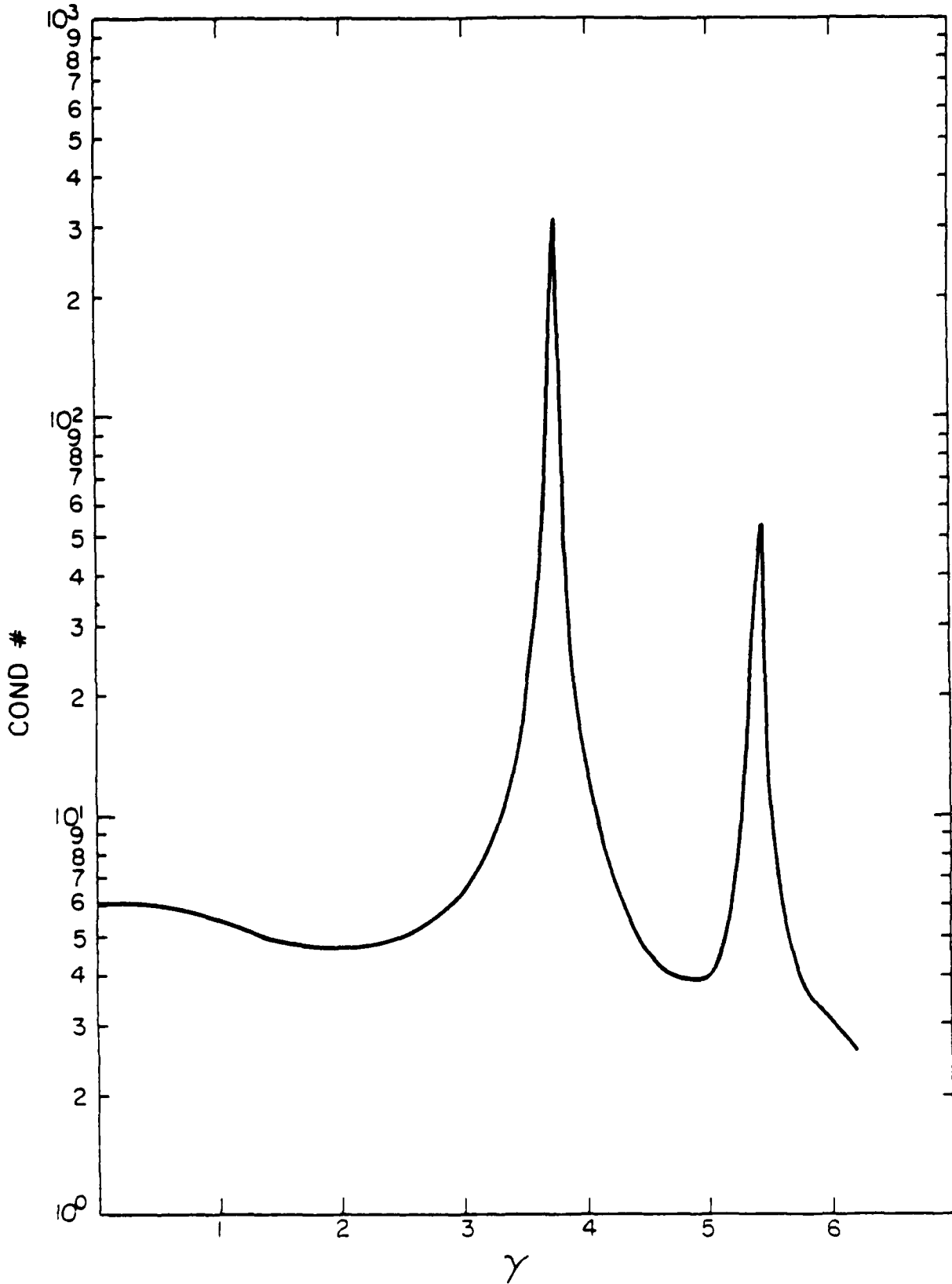


Figure 2.5 Plot of the condition number of the system matrix representing the MFIE for the example with cylinder radius equal to  $0.7582 \lambda$ .

Since the type of numerical formulation employed to solve the coupling problem requires the solution of the integral equations over a fairly wide range of spatial frequencies, it is likely that resonant frequencies will be encountered in most of the cylinder geometries of interest. Thus, it is essential that the uniqueness problem be remediated if the numerical procedure is to be practical. Chapter 4 will address this issue in detail, and discuss several possible remedies to the uniqueness problem. In Chapter 5, one of these remedies is implemented and tested for the previous examples.

#### 2.4 Summary

A numerical formulation is presented for the calculation of mutual admittance between axial slots in arbitrarily-shaped cylinders. Most of this chapter dealt with the numerical solution of the magnetic-field integral equation (MFIE). Examples were used to illustrate the stability and accuracy of the procedure, as well as to evaluate the convergence of the results as different parameters (number of cells in the model, spatial period, and truncation of the spectrum) were varied. Agreement between eigenfunction and numerical results for the first example indicates that the procedure is basically accurate and practical to apply. However, the second example showed that there is a uniqueness problem associated with the MFIE that sometimes affects the results. This problem will be the focus of Chapter 4, where remedies will be evaluated.

### 3. COUPLING BETWEEN CIRCUMFERENTIAL SLOTS

#### 3.1 Formulation

The treatment of coupling between circumferential slots is similar to that of the axial case. A two-dimensional scattering problem must be solved at each spatial frequency needed in the Fourier transform domain. However, the circumferential case is slightly more complicated because the process requires the solution of both  $\hat{t}$  and  $\hat{z}$  components of electric current on the cylinder. Although only the  $\hat{z}$  component is used in the admittance calculation, both components of electric current density appear in the coupled magnetic field integral equations

$$\tilde{H}_z^{\text{inc}}(t, \gamma) = -\tilde{J}_t(t, \gamma) - \hat{z} \cdot \text{curl} \int \hat{t}(t') \tilde{J}_t(t', \gamma) \tilde{G}(\rho; k, \gamma) dt' \quad (3.1)$$

$$\begin{aligned} \tilde{H}_t^{\text{inc}}(t, \gamma) &= \tilde{J}_z(t, \gamma) - \hat{t}(t) \cdot \text{curl} \int \hat{z} \tilde{J}_z(t', \gamma) \tilde{G}(\rho; k, \gamma) dt' \\ &\quad - \hat{t}(t) \cdot \text{curl} \int \hat{t}(t') \tilde{J}_t(t', \gamma) \tilde{G}(\rho; k, \gamma) dt' \end{aligned} \quad (3.2)$$

The "incident" fields on the left-hand side of the equation are given by

$$\tilde{H}_z^{\text{inc}}(t, \gamma) = \frac{\gamma}{kn} \int_{\text{slot A}} \left\{ \frac{\partial}{\partial t} \tilde{K}_t(t', \gamma) \right\} \tilde{G}(\rho; k, \gamma) dt' \quad (3.3)$$

$$\begin{aligned} \text{and} \quad \tilde{H}_t^{\text{inc}}(t, \gamma) &= \frac{k^2}{jkn} \int_{\text{slot A}} \tilde{K}_t(t', \gamma) \tilde{G}(\rho; k, \gamma) dt' \\ &\quad + \frac{\partial/\partial t}{jkn} \int_{\text{slot A}} \left\{ \frac{\partial}{\partial t} \tilde{K}_t(t', \gamma) \right\} \tilde{G}(\rho; k, \gamma) dt' \end{aligned} \quad (3.4)$$

where  $\tilde{G}$  is defined in Equation (2.5), and  $\tilde{K}_t$  is the Fourier transform of Equation (1.6) (taken with respect to the the variable  $z$ ).

The equation for the transverse component of the current is decoupled from the other, and this suggests that we first solve Equation (3.1) for  $J_t$ . Subsequently, the axial component can be found from Equation (3.2). Because the treatment of the circumferential case requires the solution of two integral equations, which translates into the solution of two matrix equations for each value of  $\gamma$ , the process is less efficient than the procedure described in Chapter 2 for axial slots.

### 3.2 Numerical Solution of the Coupled Integral Equations

As explained in Chapter 2, the cylinder under consideration can be modeled by a superposition of  $N$  flat cells, as illustrated in Figure 2.1. Again we consider replacing the unknown current density by an expansion in piecewise constant basis functions and enforcing the equations at the center of each cell in the model.

In addition, suppose that the source slot is represented by the same cells that comprise the model, and the aperture field (the equivalent magnetic source  $\tilde{K}_t$ ) is considered to be piecewise constant in the variable  $t$ . Then the equation to be solved for the transverse component of the electric current density reduces to the matrix form of Equation (2.11) with the exception that

$$h_i = \sum_{n=1}^{N_A} \tilde{v}_n \frac{\gamma}{kn} [\tilde{G}(\rho_1; k, \gamma) - \tilde{G}(\rho_2; k, \gamma)] \quad (3.5)$$

where

$$\rho_1 = \sqrt{\left(x_i - \frac{w}{2} \sin \Omega_n\right)^2 + \left(y_i + \frac{w}{2} \cos \Omega_n\right)^2} \quad (3.6)$$

$$\rho_2 = \sqrt{\left(x_1 + \frac{W_n}{2} \sin \Omega_n\right)^2 + \left(y_1 - \frac{W_n}{2} \cos \Omega_n\right)^2} \quad (3.7)$$

and  $\tilde{V}_n$  denotes the coefficients of a pulse expansion of the equivalent magnetic current density representing slot 'A.' Since the Fourier transform of Equation (1.6) is

$$\tilde{K}_t(t, \gamma) = \sqrt{\frac{2}{H_A W_A}} \cos\left(\frac{\pi t}{W_A}\right) \frac{Y}{2} \sin\left(\frac{\gamma H_A}{2}\right) \quad (3.8)$$

it follows that

$$\tilde{V}_n(\gamma) \cong \sqrt{\frac{2}{H_A W_A}} \frac{Y}{2} \sin\left(\frac{\gamma H_A}{2}\right) \cos\left(\frac{\pi t_n}{W_A}\right) \quad (3.9)$$

where  $t_n$  is the location of cell  $n$  in the source coordinates. Equation (3.5) is derived in Appendix A.

Thus, an  $N \times N$  matrix equation must be solved to yield the approximate solution for the transverse component of the current density. Once this is accomplished (at some value of the spatial frequency  $\gamma$ ), Equation (3.2) can be solved numerically for the  $z$ -component of the current density. If a piecewise constant expansion is used to represent  $J_z$ , and Equation (3.2) is enforced at the center of each cell in the model, the result is a second  $N \times N$  matrix equation of the form

$$\begin{bmatrix} z_{11} & z_{12} & & \\ z_{21} & z_{22} & & \\ & & \dots & \\ & & & z_{NN} \end{bmatrix} \begin{bmatrix} j_z^1 \\ j_z^2 \\ \vdots \\ j_z^N \end{bmatrix} = \begin{bmatrix} h_t^1 \\ h_t^2 \\ \vdots \\ h_t^N \end{bmatrix} \quad (3.10)$$

The right-hand side of Equation (3.10) includes the contribution from the equivalent magnetic current density and the contribution from the transverse current density found from the solution of the first  $N \times N$  matrix. In this case,  $h_t$  is given by

$$h_t^i = \sum_{n=1}^N j_t^n h_{in}^{(1)} + \sum_{n=1}^{N_A} \tilde{v}_n h_{in}^{(2)} \quad (3.11)$$

where

$$h_{in}^{(1)} \cong j\gamma \sin(\Omega_i - \Omega_n) W_n \tilde{G}(\rho_{in}; k, \gamma) \quad i \neq n \quad (3.12)$$

$$h_{ii}^{(1)} = 0 \quad (3.13)$$

$$h_{in}^{(2)} = \frac{k}{jn} \cos(\Omega_i - \Omega_n) \int_{\text{cell}_n} \tilde{G}(\rho; k, \gamma) dt + \frac{1}{jkn} \left\{ \right.$$

$$\left. \left[ -\sin \Omega_i \frac{\Delta x_1}{R_1} + \cos \Omega_i \frac{\Delta y_1}{R_1} \right] \tilde{G}^-(R_1; k, \gamma) - \left[ -\sin \Omega_i \frac{\Delta x_2}{R_2} + \cos \Omega_i \frac{\Delta y_2}{R_2} \right] \tilde{G}^-(R_2; k, \gamma) \right\} \quad (3.14)$$

$$\Delta x_1 = x_i - \frac{W_n}{2} \sin \Omega_n \quad (3.15)$$

$$\Delta y_1 = y_i + \frac{W_n}{2} \cos \Omega_n \quad (3.16)$$

$$\Delta x_2 = x_i + \frac{W_n}{2} \sin \Omega_n \quad (3.17)$$

$$\Delta y_2 = y_i - \frac{W_n}{2} \cos \Omega_n \quad (3.18)$$

$$R_1 = \sqrt{\Delta x_1^2 + \Delta y_1^2} \quad (3.19)$$

$$R_2 = \sqrt{\Delta x_2^2 + \Delta y_2^2} \quad (3.20)$$

The integration appearing in Equation (3.14) can be performed approximately using the approach in Appendix A.  $\tilde{G}(R;k,\gamma)$  is defined in Equation (2.17).

The diagonal matrix elements of Equation (3.10) are given by

$$z_{ii} = \frac{1}{2} \quad (3.21)$$

The off-diagonal elements are

$$z_{in} = - \int_{s = -\frac{W}{2}}^{\frac{W}{2}} (\sin \Omega_i \frac{\Delta y}{R} + \cos \Omega_i \frac{\Delta x}{R}) \tilde{G}(R;k,\gamma) ds \quad (3.22)$$

where  $\Delta x$ ,  $\Delta y$ , and  $R$  are defined in Equations (2.17) to (2.19).

Once the transverse currents are determined over the necessary range, the inverse transform can be computed according to Equation (1.10). However, as discussed previously, it is more efficient to perform the  $z$ -integration in the transform domain. Thus, the additional weighting factor

$$\tilde{W}(\gamma) = \frac{2 \sin \left( \frac{\gamma H_B}{2} \right)}{\gamma} \quad (3.23)$$

should be included in order to account for the convolution with the piecewise-constant from Equation (1.3).

### 3.3 Preliminary Numerical Results

A computer code similar to that described in Chapter 2 was developed to implement the above formulation for circumferential slot coupling. The program

requires that the cylinder be modeled by a superposition of flat cells and also that the source slot be represented by several of the same cells that comprise the model. To verify the accuracy of the procedure, results from this program for coupling between slots in circular cylinders can be compared to published eigenfunction solutions [5].

Consider a circular cylinder having radius of one wavelength and containing circumferential slots of size  $0.2 \times 0.5$  wavelength. The cylinder geometry is shown in Figure 3.1. Eigenfunction solutions for several different slot separations are given in Table 3.1, from reference [5]. The data in Table 3.1 are the values that should be produced by the numerical procedure under ideal conditions, and thus will be used to judge the accuracy of the numerical results. Suppose that the cylinder cross-section is modeled with 88 equal-sized cells, of which seven are used to model the source and secondary slots. The actual slot dimensions used within the numerical procedure are  $0.2 \times 0.4998$  wavelength, and thus the slot size in the model is an accurate representation of the desired slot.

In order to determine the extent of the spectrum necessary for inclusion in the inverse Fourier transform, consider the spectral admittance function produced in the course of numerical calculation. This function is displayed in Figure 3.2. It appears from this figure that the spectrum decays to a negligible value once the spatial frequency reaches  $\gamma = 20$ . To verify this conclusion, Table 3.2 shows the admittance between several slots produced with the spectrum truncated at  $\gamma = 20$  and  $\gamma = 30$ , for a fixed period size. In this case, truncation at  $\gamma = 20$  seems appropriate.

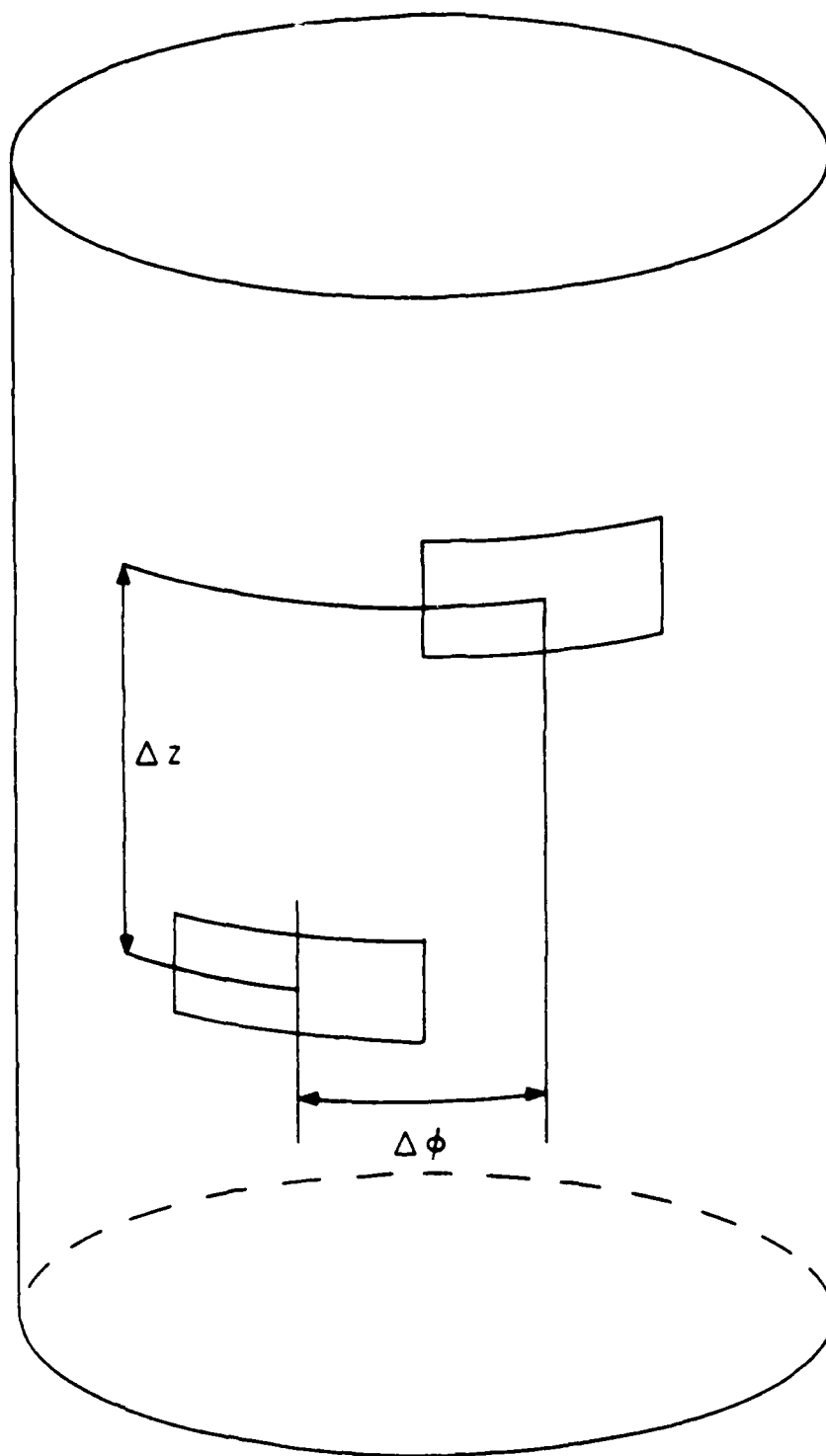


Figure 3.1 Geometry of circular cylinder containing two circumferential slots.

TABLE 3.1

Eigenfunction data for the mutual admittance between circumferential slots in a one-wavelength radius circular cylinder. The slots have  $H = 0.2\lambda$  and  $W = 0.5\lambda$ . The admittance is given in magnitude (decibels) and angle (degrees).

$\Delta z$	$\Delta\phi$	$Y_{AB}$ in dB / <u>degrees</u>
$0.5\lambda$	$0^\circ$	- 67.87 / <u>-117</u>
1.0	0	- 72.54 / <u>67</u>
2.0	0	- 77.46 / <u>68</u>
4.0	0	- 82.22 / <u>66</u>
8.0	0	- 86.65 / <u>62</u>
1.0	45	- 82.30 / <u>-26</u>

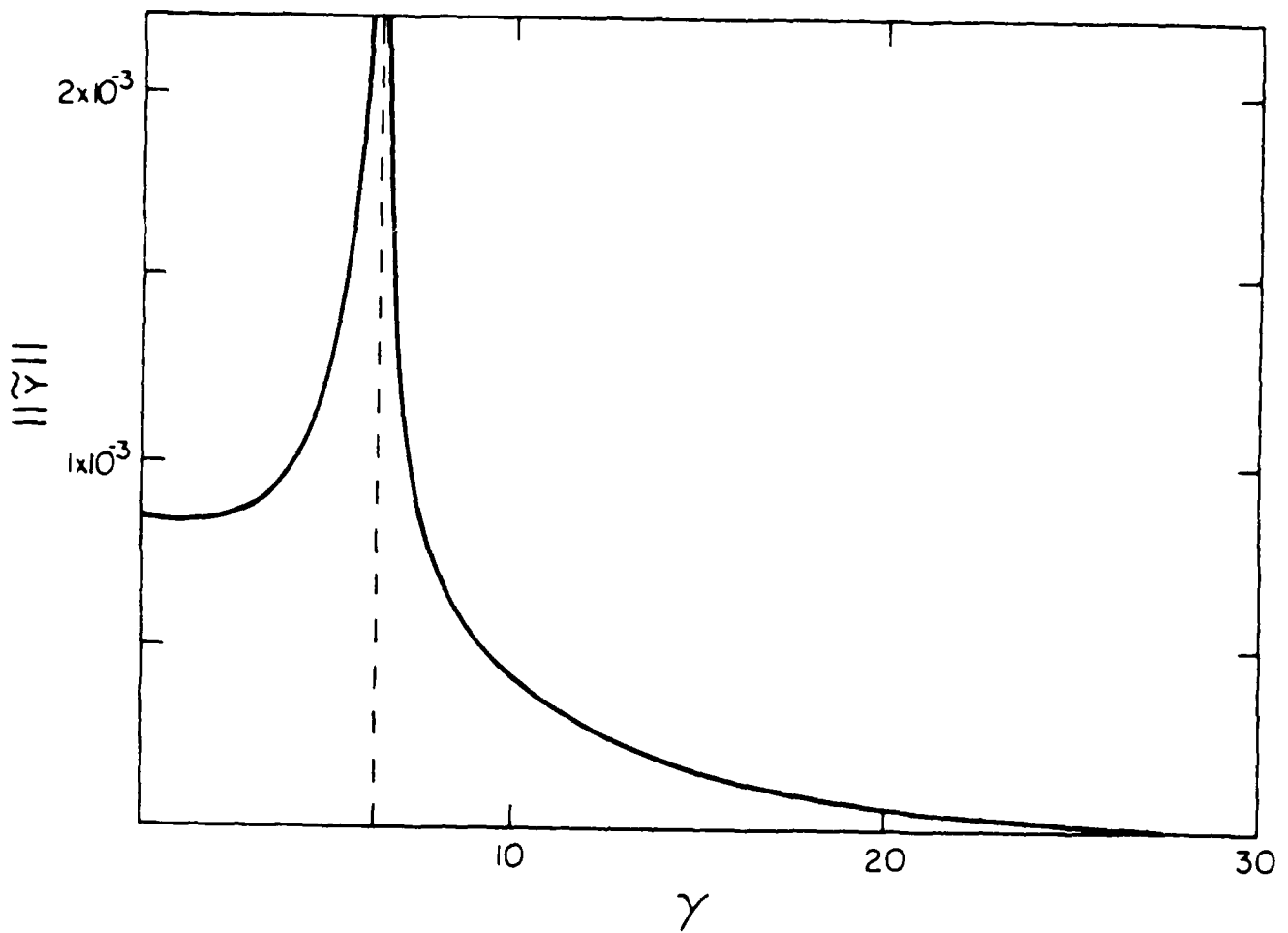


Figure 3.2

Plot of the norm of the spectral admittance function for an example involving circumferential slots in a cylinder of  $1.0 \lambda$  radius and slots of dimension  $H = 0.2 \lambda$ . The norm is taken with respect to the circumferential variable.

TABLE 3.2

Numerical results for the mutual admittance between circumferential slots as a function of spectrum truncation. The circular cylinder has radius of one wavelength and is modeled with 88 cells. The slots have  $H = 0.2\lambda$  and  $W = 0.4998\lambda$ . The period size is  $P_z = 18.5$  wavelengths. The admittance is given in magnitude (decibels) and angle (degrees). (MFIE solution)

$\Delta z$	$\Delta \phi$	$\gamma_{\max} \approx 20$	$\gamma_{\max} \approx 30$
0.5 $\lambda$	0°	- 68.80 / <u>-117.0</u>	- 68.80 / <u>-117.0</u>
1.0	0	- 73.79 / <u>68.7</u>	- 73.84 / <u>68.6</u>
2.0	0	- 80.08 / <u>71.2</u>	- 80.15 / <u>71.0</u>
4.0	0	- 88.25 / <u>74.1</u>	- 88.17 / <u>74.3</u>
8.0	0	- 100.12 / <u>81.9</u>	- 100.38 / <u>81.7</u>
1.0	45	- 83.21 / <u>-48.2</u>	- 83.21 / <u>-48.2</u>

Table 3.3 shows the admittance between slots for three different period sizes. For the range of slot sizes shown in Table 3.3, it appears that a period of about 40 wavelengths is necessary for reasonably "converged" values. For slots separated by four or more wavelengths, the admittance values appear to improve with increasing period, but not tremendously.

The MFIE uniqueness problem discussed in Chapter 2 may also affect the results of the circumferential slot procedure. Here, the process requires the solution of two matrix equations, each of which could be corrupted by the problem. Figures 3.3 and 3.4 show plots of the matrix condition number as a function of  $\gamma$ . Theoretical resonance frequencies are given in Tables 3.4 and 3.5, and these correlate with the values of  $\gamma$  where the condition number degrades. However, apparently the problem is not severe enough in this example to significantly affect the accuracy of the numerical results.

Table 3.6 shows eigenfunction admittance data for circumferential slots of dimension  $0.3048 \times 0.6858$  wavelength in a circular cylinder of radius 1.517 wavelengths. An 83 cell model comprised of equal-sized cells requires that the actual modeled slot dimensions be  $0.3048 \times 0.6891$  wavelength. Results from the numerical procedure are displayed in Tables 3.7 and 3.8. The agreement is reasonable between the numerical and eigenfunction results. The spectral admittance function is displayed in Figure 3.5, and it appears that the spectrum can be adequately truncated at  $\gamma = 20$ .

To test the uniqueness problem for this example, the matrix condition number for each of the two systems arising here was compared to that for theoretical

TABLE 3.3

Numerical results for the mutual admittance between circumferential slots as a function of period size. The circular cylinder has radius of one wavelength and is modeled with 88 cells. The slots have  $H = 0.2\lambda$  and  $W = 0.4998\lambda$ . The spectrum is truncated at  $\gamma = 20$ . The admittance is given in magnitude (decibels) and angle (degrees). (MFIE solution)

$\Delta z$	$\Delta\phi$	$P_z = 18.5\lambda$	$P_z = 40.5$	$P_z = 60.5$
$0.5\lambda$	$0^\circ$	- 68.80 / <u>-117.0</u>	- 68.51 / <u>-116.5</u>	- 68.53 / <u>-116.5</u>
1.0	0	- 73.79 / <u>68.7</u>	- 73.47 / <u>68.2</u>	- 73.25 / <u>67.7</u>
2.0	0	- 80.08 / <u>71.2</u>	- 79.27 / <u>70.6</u>	- 78.83 / <u>71.0</u>
4.0	0	- 88.25 / <u>74.1</u>	- 84.72 / <u>74.6</u>	- 84.62 / <u>74.5</u>
8.0	0	- 100.12 / <u>81.9</u>	- 90.79 / <u>73.5</u>	- 90.40 / <u>78.9</u>
1.0	45	- 83.21 / <u>-48.2</u>	- 82.97 / <u>-38.9</u>	- 82.95 / <u>-34.2</u>

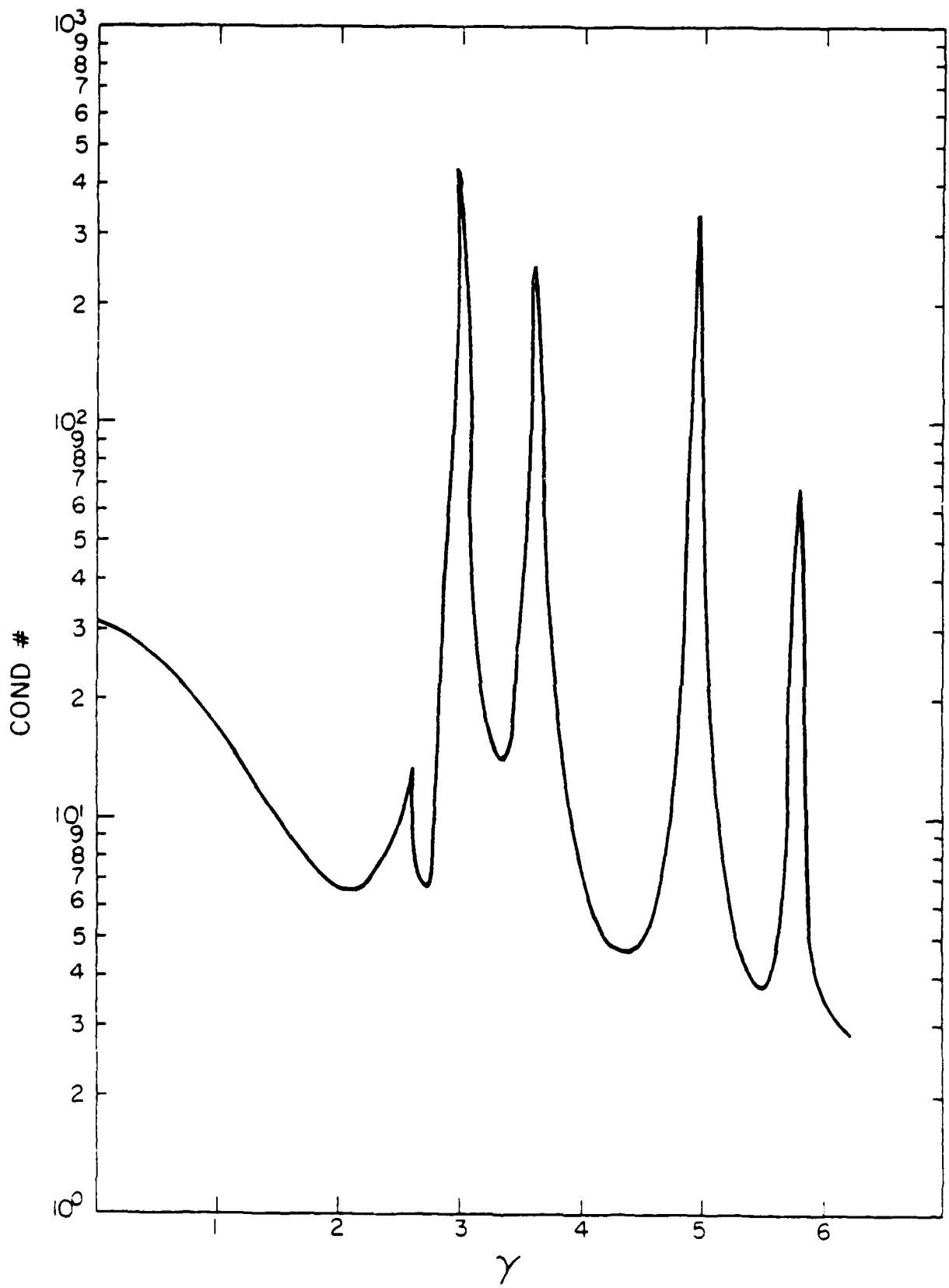


Figure 3.3 Plot of the matrix condition number of the system representing the longitudinal MFIE for a  $1 \lambda$  radius cylinder.

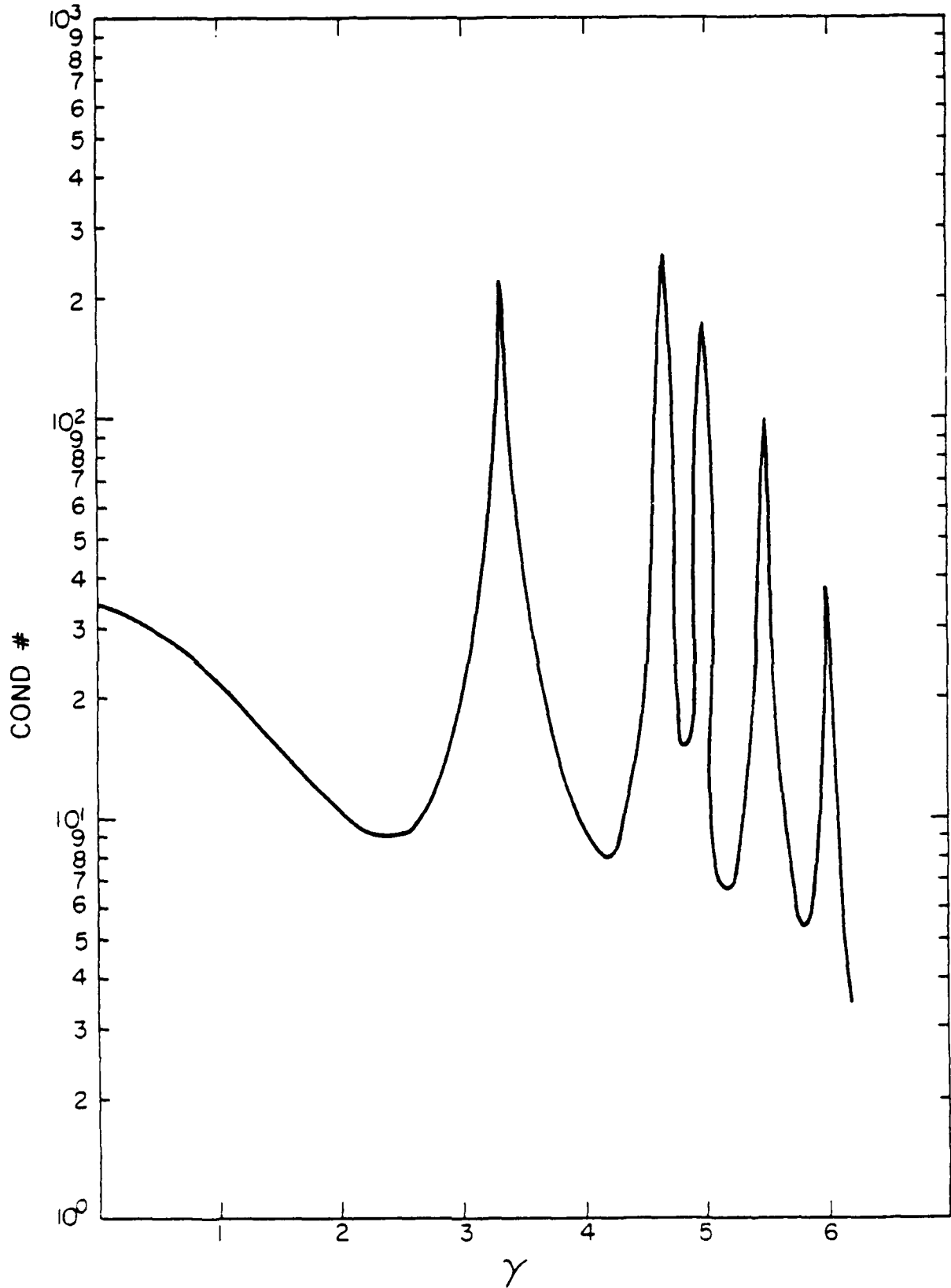


Figure 3.4 Plot of the matrix condition number of the system representing the transverse MFIE for a  $1 \lambda$  radius cylinder.

TABLE 3.4

Theoretical resonance frequencies of the longitudinal MFIE applied to a circular cylinder with  $1\lambda$  radius.

n	$\gamma$
1	3.00
2	3.62
3	4.98
4	5.81

TABLE 3.5

Theoretical resonance frequencies of the transverse MFIE applied to a circular cylinder with radius equal to one wavelength.

n	$\gamma$
1	3.33
2	3.35
3	4.67
4	4.98
5	5.49
6	6.01

TABLE 3.6

Eigenfunction data for the mutual admittance between circumferential slots in a 1.517 wavelength radius circular cylinder. The slots have  $H = 0.3048\lambda$  and  $W = 0.6858\lambda$ . The separation  $\Delta\phi$  is zero. The admittance is given in magnitude (decibels) and angle (degrees).

$\Delta z$	$Y_{AB}$
0.38 $\lambda$	- 62.62 / <u>-72</u>
0.76	- 66.82 / <u>155</u>
1.52	- 71.78 / <u>-117</u>
2.29	- 74.78 / <u>-31</u>
3.05	- 76.89 / <u>54</u>
8.38	- 84.06 / <u>-70</u>
9.14	- 84.61 / <u>15</u>
9.91	- 85.12 / <u>100</u>
10.67	- 85.63 / <u>-175</u>
11.43	- 86.09 / <u>-90</u>

TABLE 3.7

Numerical results for the mutual admittance between circumferential slots as a function of period size. The circular cylinder has radius of one wavelength and is modeled with 83 cells. The slots have  $H = 0.3048\lambda$  and  $W = 0.6891\lambda$ . The spectrum is truncated at  $\gamma = 20$ . The admittance is given in magnitude (decibels) and angle (degrees). (MFIE solution)

$\Delta z$	$P_z = 30.5\lambda$	$P_z = 60.5$	$P_z = 90.5$
0.38 $\lambda$	- 62.93 / <u>-70.2</u>	- 62.84 / <u>-70.9</u>	- 62.85 / <u>-70.9</u>
0.76	- 66.81 / <u>155.1</u>	- 66.74 / <u>154.0</u>	- 66.97 / <u>154.4</u>
1.52	- 73.37 / <u>-117.6</u>	- 72.47 / <u>-116.3</u>	- 72.54 / <u>-116.8</u>
2.29	- 74.57 / <u>-26.0</u>	- 74.57 / <u>-26.9</u>	- 74.79 / <u>-29.0</u>
3.05	- 79.26 / <u>51.3</u>	- 78.37 / <u>54.5</u>	- 77.74 / <u>51.8</u>

TABLE 3.8

Numerical results for the mutual admittance between circumferential slots as a function of period size. The circular cylinder has radius of one wavelength and is modeled with 83 cells. The slots have  $H = 0.3048\lambda$  and  $W = 0.6891\lambda$ . The spectrum is truncated at  $\gamma = 20$ . The admittance is given in magnitude (decibels) and angle (degrees). (MFIE solution)

$\Delta z$	$P_z = 30.5\lambda$	$P_z = 60.5$	$P_z = 90.5$
$8.38\lambda$	- 84.19 / <u>-52.3</u>	- 84.26 / <u>-56.5</u>	- 84.62 / <u>-60.2</u>
9.14	- 86.13 / <u>-14.7</u>	- 85.74 / <u>-4.1</u>	- 86.55 / <u>0.8</u>
9.91	- 87.08 / <u>126.5</u>	- 84.77 / <u>121.0</u>	- 85.38 / <u>108.9</u>
10.67	- 85.56 / <u>159.6</u>	- 87.60 / <u>170.5</u>	- 85.68 / <u>117.7</u>
11.43	- 93.04 / <u>-43.7</u>	- 87.89 / <u>-77.8</u>	- 87.83 / <u>-68.4</u>

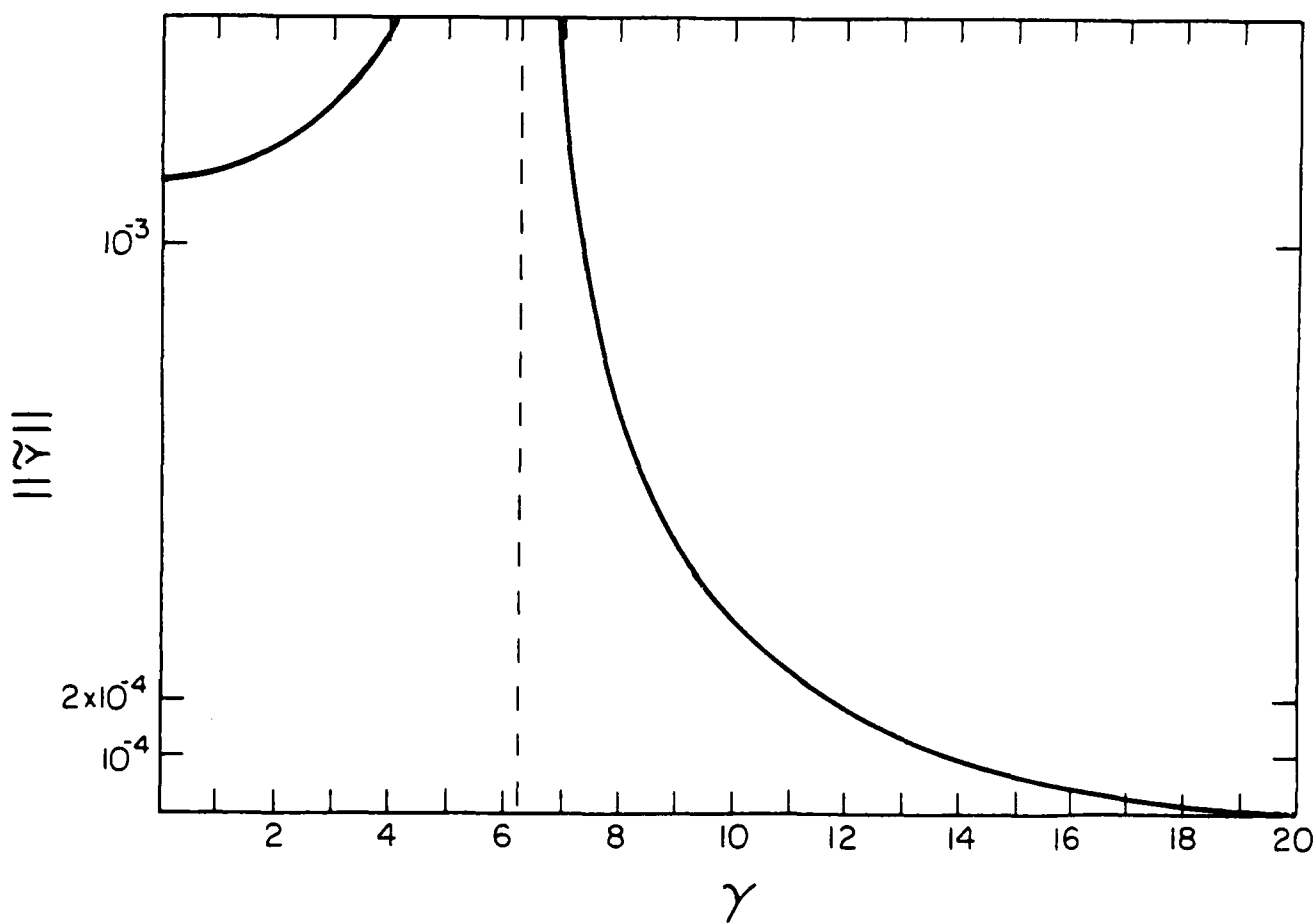


Figure 3.5 Plot of the norm of the spectral admittance function for an example involving circumferential slots in a cylinder of  $1.517 \lambda$  radius. Slot dimension  $H = 0.3028 \lambda$ . The norm is taken with respect to the circumferential variable.

resonance frequencies. These are listed in Tables 3.9 and 3.10. Good correlation is obtained between the theoretical values of  $\gamma$  and spatial frequencies where the condition number degrades. Because of the large number of resonance frequencies arising in this case, it is rather surprising that good agreement is obtained between numerical and eigenfunction results. Since the uniqueness problem will undoubtedly prove to be problematic for many examples of interest, Chapter 4 includes a discussion of the problem and presents several remedies. Chapter 5 discusses the implementation of one remedy, the use of the combined-field integral equation (CFIE) as an alternative to the MFIE. It will be shown that admittance results based upon the CFIE for the above cylinder geometries are in better agreement with eigenfunction results than those obtained from the MFIE.

TABLE 3.9

Theoretical resonance frequencies of the longitudinal MFIE applied to a circular cylinder with radius equal to 1.517 wavelengths, in terms of the spatial frequency  $\gamma$ .

n	$\gamma$
1	2.46
2	2.63
3	2.95
4	3.80
5	4.25
6	4.67
7	5.12
8	5.29
9	5.75
10	6.08

TABLE 3.10

Theoretical resonance frequencies of the transverse MFIE applied to a circular cylinder with radius equal to 1.517 wavelengths, in terms of the spatial frequency  $\gamma$ .

n	$\gamma$
1	1.43
2	2.74
3	2.80
4	3.40
5	3.88
6	4.25
7	4.47
8	4.65
9	5.21
10	5.21
11	5.64
12	5.75
13	5.95
14	6.17

#### 4. REMEDIATION OF THE UNIQUENESS PROBLEM ASSOCIATED WITH CERTAIN INTEGRAL EQUATIONS

##### 4.1 The Interior Resonance Problem

Integral equation formulations have distinctive advantages over other approaches for the analysis of electromagnetic scattering problems. They also suffer certain disadvantages, one of which concerns the uniqueness of their solutions. Generally, a surface integral equation can be used to represent both the interior and exterior electromagnetic problems. In other words, the model used with the equation can represent the interior boundary of a cavity or the exterior surface of a solid scatterer. In contrast to the exterior scattering problem, which involves finding the fields due to an applied source, the cavity problem requires the identification of source-free "cavity modes." Because the cavity problem involves homogeneous equations, the task requires the identification of eigenfrequencies where source-free cavity "resonances" can occur. Thus, at discrete eigenfrequencies of certain integral equations, the solution to an exterior scattering problem is not unique. It is important to note that not all integral equations suffer from this uniqueness problem; in fact, one remedy to the problem is to employ a different integral equation formulation. However, the common equations used for electromagnetic scattering problems (the electric-field and magnetic-field equations, denoted EFIE and MFIE) can be corrupted by the presence of homogeneous solutions corresponding to interior cavity modes. Previous chapters have identified this problem in connection with the solution to the MFIE for two-dimensional scattering.

The nature of what is commonly called "the interior resonance problem" was encountered in connection with integral equations of electromagnetic scattering by Mei and Van Bladel in 1963 [19], [20]. However, several years passed before a clear identification of the uniqueness problem was set forth by Mitzner [21], who recommended the use of a linear combination of the EFIE and MFIE as a remedy. The resulting equation is now denoted as the "combined-field integral equation" (CFIE), and has been discussed in detail by Mautz and Harrington [18]. An alternate integral equation formulation was presented by Bolomey and Tabbara [22], and an extension of their approach was developed by Mautz and Harrington and named the "combined-source" formulation [23]. The basic cause of the EFIE and MFIE uniqueness problems is the lack of an explicit boundary condition that forces the interior fields to vanish. Mittra and Klein discuss the problem in detail and investigate the direct overspecification of the boundary conditions throughout the interior region [17]. An alternate procedure is to augment the original EFIE or MFIE (which involve only the tangential field components) with appropriate constraints on the normal fields. The resulting "augmented-field integral equations" are discussed by Yaghjian [24]. Finally, Sarkar and Rao have discussed the idea of finding the "minimum norm" solution to the original EFIE and MFIE [25].

Although a plethora of remedies has been proposed, all require additional complexity and computational effort over the use of the original EFIE or MFIE formulations. The combined field and source formulations usually produce a matrix equation of the same order as the original (see discussion to follow for a counterexample), but always require more complicated matrix elements than the original formulation. The direct overspecification of the original equation or

the use of the augmented-field formulation requires the solution of an overspecified (not square) matrix equation. The minimum norm procedure also requires a least-square type of solution, and does not yield the true currents on the scatterer.

Although the cause of the "internal resonance" problem has been fairly well-understood for some time in electromagnetics and has also been discussed in the context of integral equations of acoustic scattering [26], [27], the problem does not arise unless the scatterers under consideration are large enough to support cavity resonant fields. Over the past twenty-five years, much of the development work involving integral equations has concentrated on the treatment of electrically small or moderately-sized scatterers. However, advances in computers (including the widespread availability of supercomputers) coupled with improvements in specialized algorithms for the treatment of electrically large structures [28], [29] have made it possible to treat scatterers exceeding several wavelengths in size. Thus, it is likely that the problem will be observed more frequently in the future.

Chapters 2 and 3 presented a procedure for the calculation of currents induced upon an infinite cylinder by a finite source. The formulation involved the Fourier transform and required the solution of two-dimensional integral equations over the entire plane-wave spectrum excited by the source. Thus, the integral equations were to be solved over a continuous range of the transverse dimension. If the scatterer geometry represents resonant cavities at certain locations throughout this range, there is a strong probability that the solution will be corrupted by homogeneous solutions to the integral equations. In fact,

erratic behavior observed in the preliminary results presented in Chapters 2 and 3 has been attributed to the uniqueness problem.

It is apparent that some remedy to the uniqueness problem associated with the MFIE must be found if the procedures described in Chapters 1, 2 and 3 are to be useful for the analysis of coupling between slots in large cylinders. Several remedies have been mentioned above. In order to judge the overall effectiveness and required computational overhead associated with these remedies, this chapter presents a comparison for the type of equations employed in Chapters 2 and 3. Based upon this comparison, the combined-field formulation is judged to be the best candidate of those considered. The CFIE is incorporated into the slot coupling formulation in Chapter 5.

#### 4.2 The Nature of the Uniqueness Problem

To explain the "interior resonance" problem in detail, consider the MFIE formulation for the scattering of a transverse-electric (TE) plane wave from a perfectly conducting cylinder (a two-dimensional problem). The wave is incident on the cylinder from some oblique angle, so that the  $z$ -dependence is of the form

$$e^{j\gamma z}, \quad \gamma^2 + k_t^2 = k^2 \quad (4.1)$$

Chapter 2 presented the integral equation

$$-H_z^{inc}(t) = J_t(t) + \hat{z} \cdot \text{curl} \int \hat{E}(t') J_t(t') G(\rho) dt' \quad (4.2)$$

where

$$G(\rho) = \frac{1}{4j} H_0^{(2)}(k_t \rho) \quad (4.3)$$

and

$$\rho = \sqrt{[x(t) - x(t')]^2 + [y(t) - y(t')]^2} \quad (4.4)$$

(Cavity resonances only occur throughout the "visible region" of the spectrum, and thus we consider only the case  $k^2 > \gamma^2$ .)

In order to study the uniqueness problem, consider the special case of a circular cylinder. Since this special case involves a separable geometry, exact solutions for plane-wave scattering can be found using the separation-of-variables procedure [30]. In addition, analytical expressions for the eigenvalues of the MFIE as a function of the cylinder radius "a" are available and given as

$$\lambda_n^{\text{MFIE,TE}} = \frac{+j\pi k_t a}{2} J_n(k_t a) H_n^{(2)}(k_t a) \quad (4.5)$$

where

$$k_t = \sqrt{k^2 - \gamma^2} \quad (4.6)$$

A plot of the eigenvalues of orders 0, 1, and 2 is presented in Figure 4.1 as a function of  $k_t$ . For small values of  $k_t a$  (low frequency excitation), the eigenvalues lie at 0.5 or 1.0 in the right-half plane. However, as  $k_t a$  increases, they move in a circularlike path that passes through the origin. From Equation (4.5), it is clear that eigenvalues vanish at the zeroes of the Bessel function  $J_n(k_t a)$ . These values  $k_t a$  also correspond to the discrete frequencies where source-free solutions exist for the interior problem. The interior problem represented by this MFIE is the circular cavity having walls that are perfect magnetic conductors [17]. In any case, no unique solution exists to the MFIE if one of its eigenvalues is zero.

In practice, numerical techniques are employed to solve integral equations for geometries that are not separable, i.e., geometries that cannot be treated

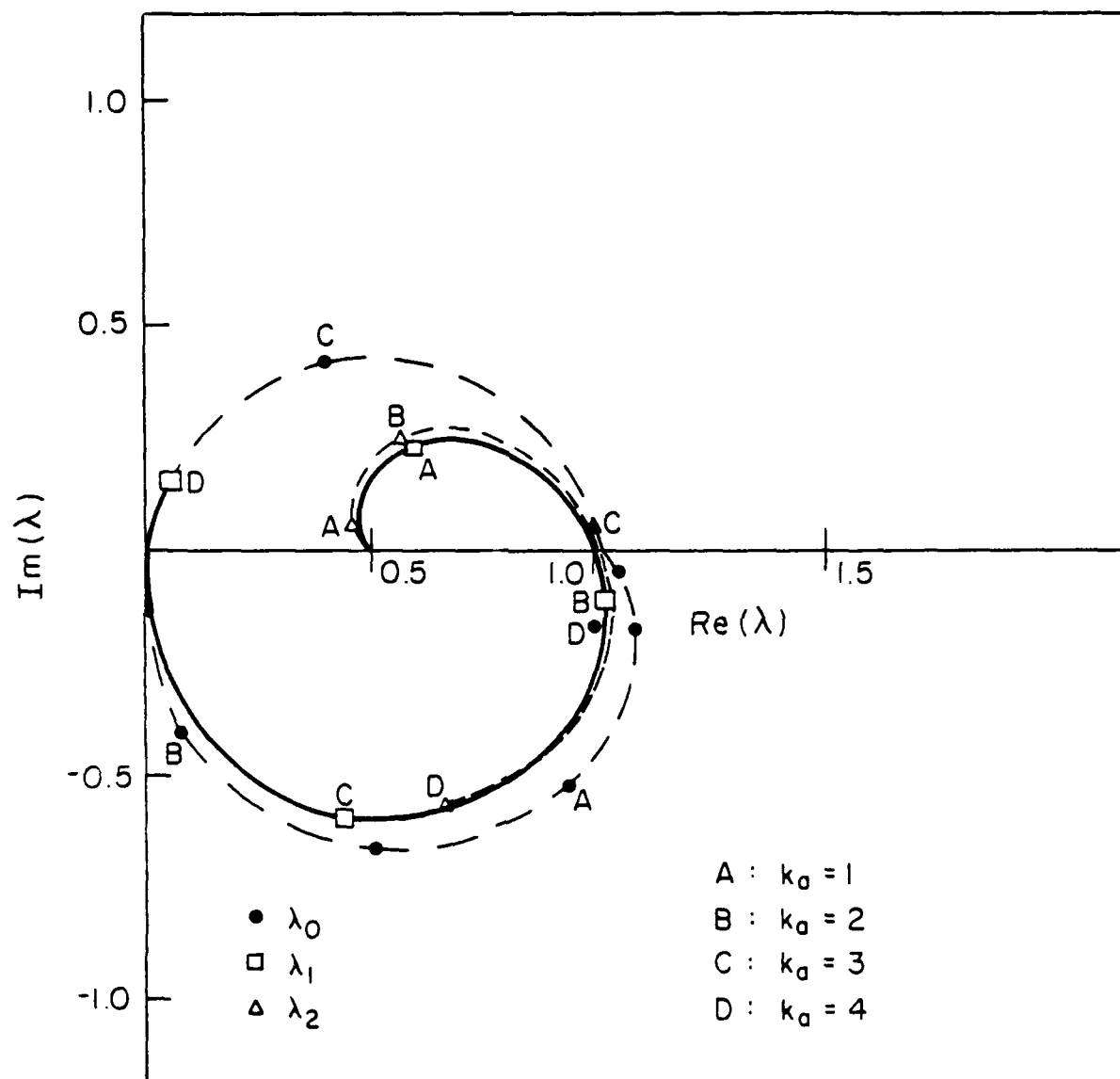


Figure 4.1 Plot of the three dominant eigenvalues of the TE MFIE as a function of  $k_a$ .

analytically. Typically, the method of moments is used to convert the original equation to a matrix equation of finite order [14]. At the discrete values of  $k_t$  where an eigenvalue of the original integral equation vanishes, an eigenvalue of the corresponding matrix equation will also vanish, or at least become very small. This is a consequence of the manner in which eigenvalues are projected from an original continuous operator onto a matrix operator [31]. The numerical solutions obtained from the integral equation will usually degrade in the vicinity of a resonance, as illustrated in Figures 4.2 through 4.4. These figures depict the current density induced upon three circular cylinders of slightly different radius by a plane wave. Exact solutions are shown for comparison. In Figure 4.2, good agreement is observed between the exact and numerical results. In Figure 4.3, the agreement has deteriorated due to the fact that the cylinder is nearly resonant. In Figure 4.4, which represents a cylinder that is internally resonant, large errors are observed in the numerical result.

Since an eigenvalue of the matrix equation will approach the origin near an internal resonance, Mittra and Klein have recommended using the matrix condition number as a flag to indicate potential resonance problems [17]. Several figures have been presented in Chapter 2 and Chapter 3 depicting plots of the matrix condition number as function of the axial wavenumber. Sharp spikes in Figures 2.5, 3.3 and 3.4 indicate the locations of cavity resonances. Since these matrices represent scattering from circular cylinders, it is possible to predict the locations analytically. The spikes in Figures 2.5 and 3.4 represent eigenfrequencies of the MFIE discussed above, and these occur at the zeroes of the Bessel function  $J_n(k_t a)$ . The spikes in Figure 3.3 represent eigenfrequencies of the MFIE presented in Equation (3.2), and these occur at the zeroes of  $J_n'(k_t a)$ .

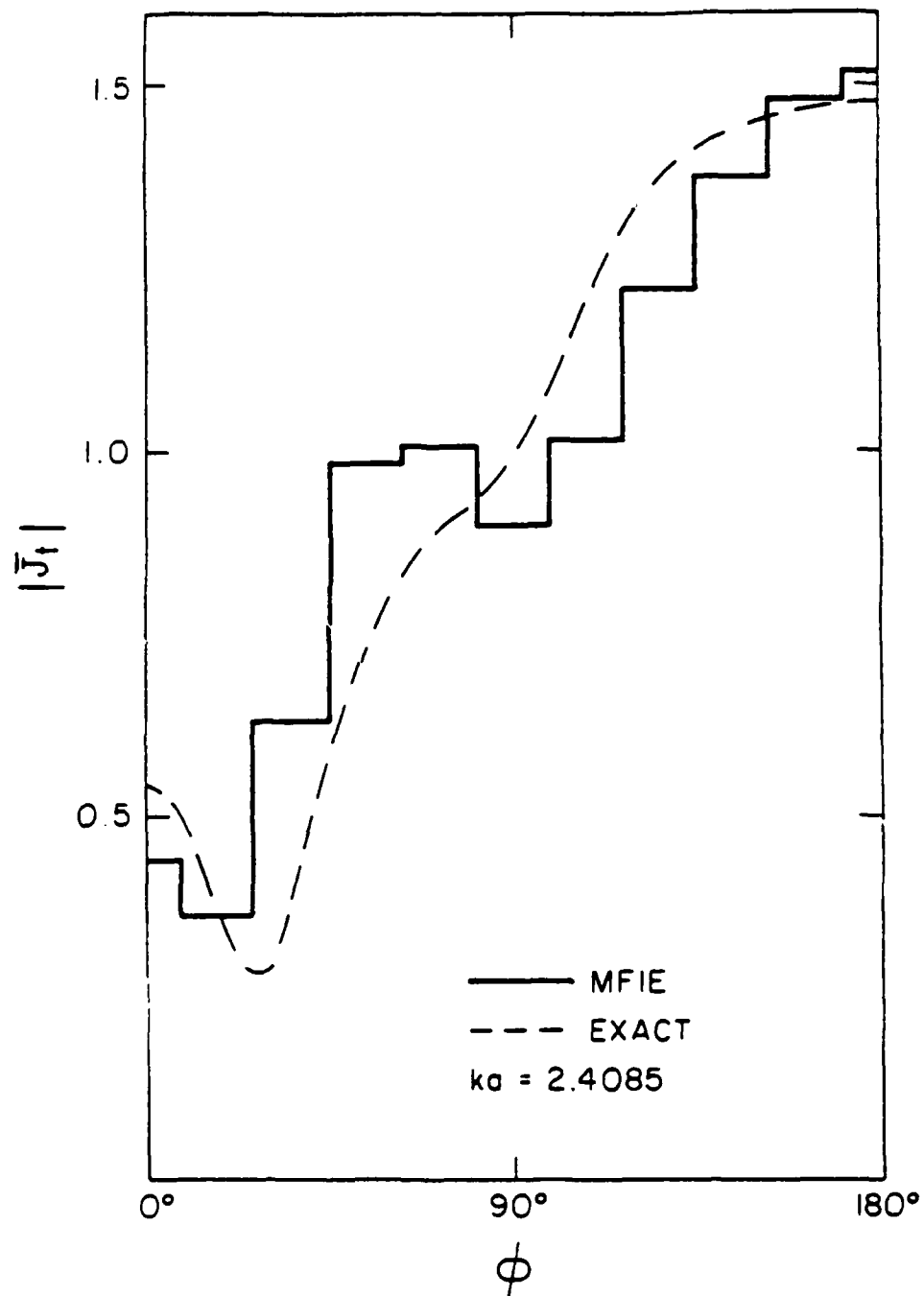


Figure 4.2

Comparison of the MFIE and exact solutions for the TE current density induced on a circular cylinder of radius  $0.3833 \lambda$ .

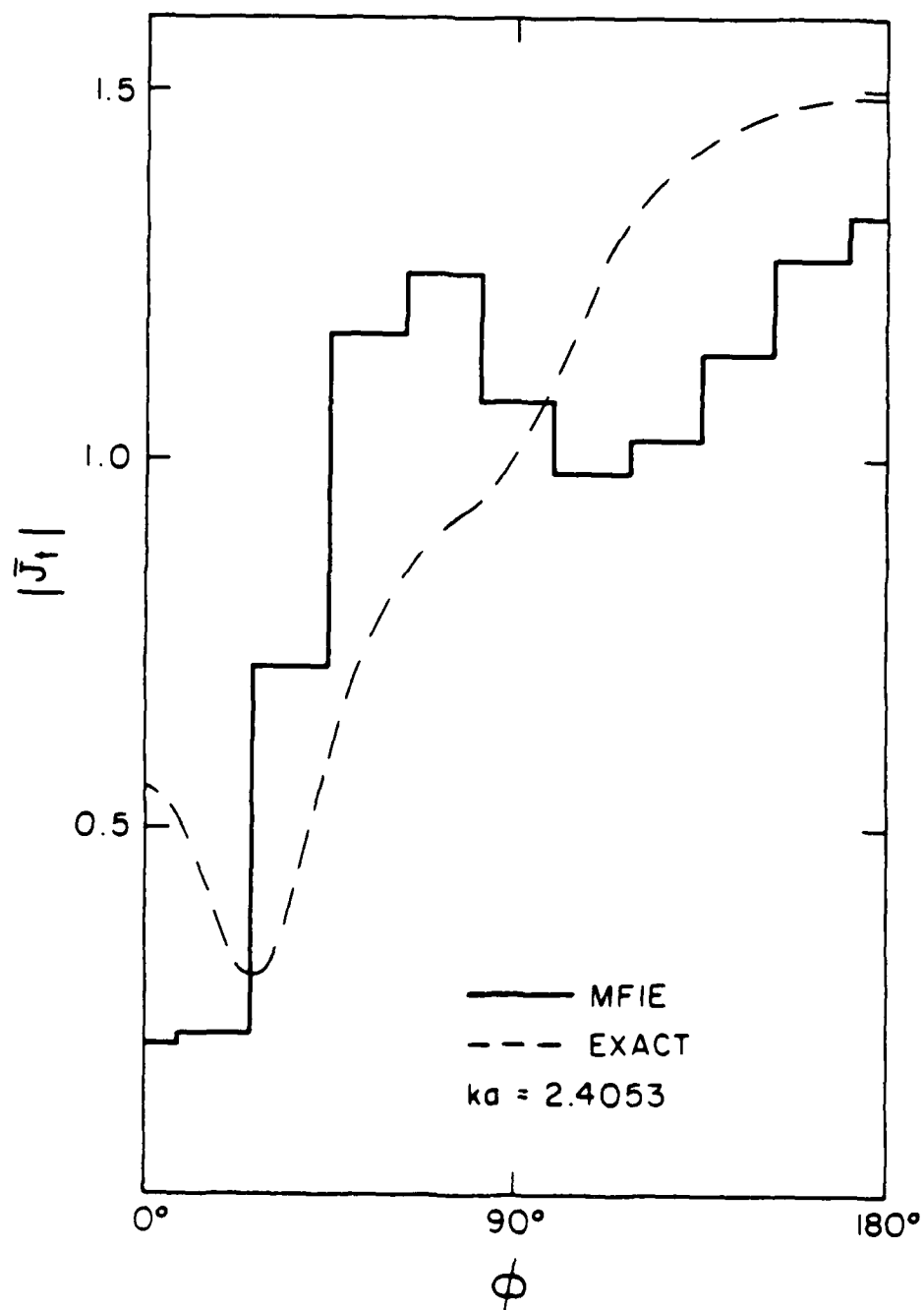


Figure 4.3 Comparison of the MFIE and exact solutions for the TE current density induced on a circular cylinder of radius  $0.3828 \lambda$ .

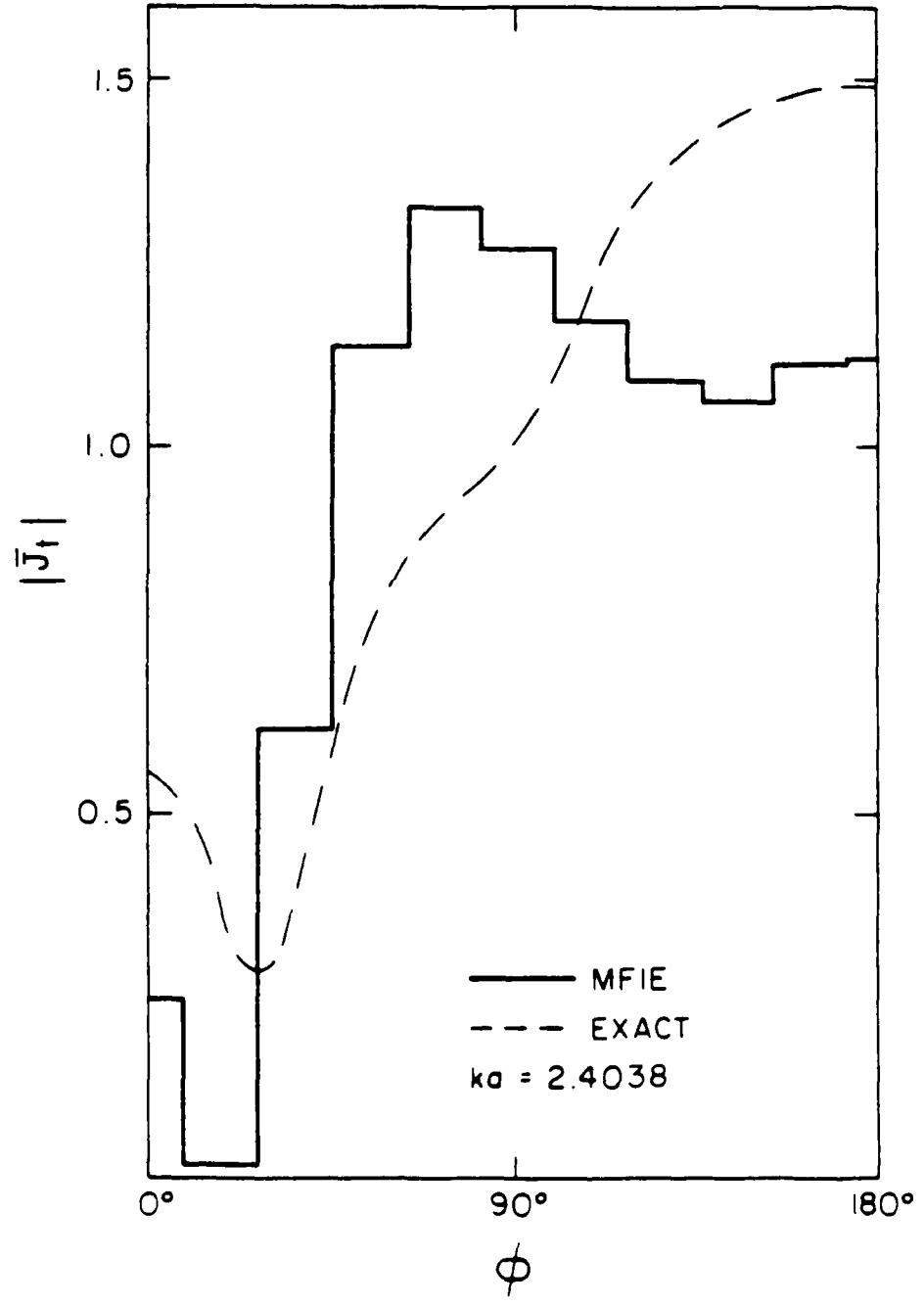


Figure 4.4 Comparison of the MFIE and exact solutions for the TE current density induced on a circular cylinder of radius  $0.3826 \lambda$ .

The EFIE also suffers from the internal resonance problem. As an illustration, consider the EFIE representing the scattering of a TE wave normally incident on a perfectly conducting cylinder. The equation is

$$E_t^{\text{inc}}(t) = -\hat{t} \cdot \frac{(\text{grad div} + k^2)}{jk} \eta \int \bar{J}_t(t') G(\rho) dt' \quad (4.7)$$

where  $G$  is defined in Equation (4.3) and  $\rho$  in Equation (4.4). If applied to circular cylinders having radius  $a$ , the eigenvalues of the integral operator are available and given as

$$\lambda_n^{\text{EFIE,TE}} = \frac{\eta \Pi k a}{2} J_n'(ka) H_n^{(2)}(ka) \quad (4.8)$$

A plot of the eigenvalues of orders 0, 1 and 2 is presented in Figure 4.5, as a function of  $k_t a$ . The character of the EFIE operator is different from that of the MFIE operator, and the EFIE eigenvalues lie along the negative imaginary axis for small  $k_t a$ . The eigenvalues pass through the origin at zeros of the Bessel function  $J_n'(k_t a)$ , and at these eigenfrequencies the EFIE has no unique solution. In this case, these values of  $k_t a$  correspond to the locations of source-free transverse-electric modes in a cavity having perfectly conducting walls.

#### 4.3 The Combined-Field Formulation

Not all integral equations suffer from the uniqueness problem described above. A formulation known as the combined-field integral equation (CFIE) involves the linear combination of the EFIE and MFIE discussed above. For normally incident TE wave scattering from perfectly conducting cylinders, the CFIE takes the form

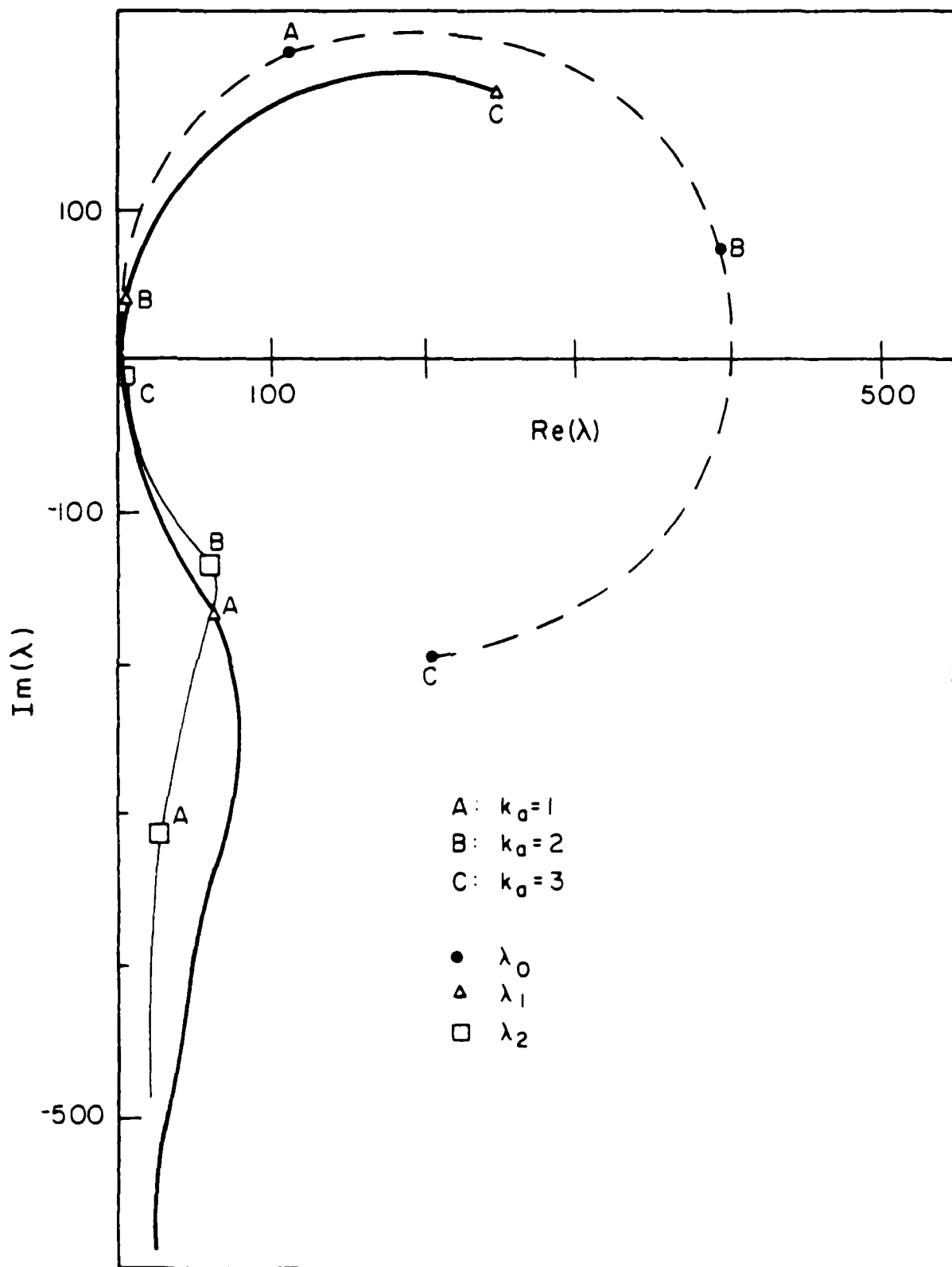


Figure 4.5

Plot of the three dominant eigenvalues of the TE EFIE as a function of  $ka$ .

$$\begin{aligned}
\alpha E_t^{\text{inc}}(t) - (1-\alpha) \eta H_z^{\text{inc}}(t) &= (1-\alpha) \eta J_t(t) \\
+ (1-\alpha) \eta \hat{z} \cdot \text{curl} \int \bar{J}_t(t') G(\rho) dt' \\
- \alpha \eta \epsilon \cdot \left( \frac{\text{grad div} + k^2}{jk} \right) \int \bar{J}_t(t') G(\rho) dt' & \quad (4.9)
\end{aligned}$$

where  $\alpha$  is a parameter used to weigh the electric-field and magnetic-field contributions to the CFIE, and  $G$  has been defined in Equations (4.3) and (4.4). If applied to a circular cylinder of radius  $a$ , the eigenvalues of the CFIE are given as

$$\lambda_n^{\text{CFIE,TE}} = \frac{\eta \Pi k a}{2} H_n^{(2)}(ka) [\alpha J_n'(ka) + j(1-\alpha) J_n(ka)] \quad (4.10)$$

A plot of the three dominant eigenvalues as a function of  $ka$  is presented in Figure 4.6. Assuming that  $\alpha$  is not equal to zero or one, these eigenvalues never vanish, and thus unique solutions to the CFIE exist at all values of  $ka$ .

Although the CFIE has unique solutions, the computational effort required to construct a matrix equation representing the CFIE is roughly double that required for the EFIE or MFIE alone. In most cases, the CFIE matrix equation is of the same order as that of the EFIE or MFIE, and thus no additional effort is required to solve the matrix over that of the original formulations. But this is not always the case. For instance, the MFIE presented in Equation (4.2) for the scattering of obliquely incident waves from a two-dimensional cylinder only involved the  $z$ -component of the  $H$ -field and the  $t$ -component of the electric current density. There is also a  $z$ -component of the current density present in the problem, but it is decoupled from the  $z$ -component of the  $H$ -field and does not appear in the MFIE. The EFIE and CFIE presented in Equations (4.7) and (4.9) are specialized to the case of normally incident waves. For obliquely

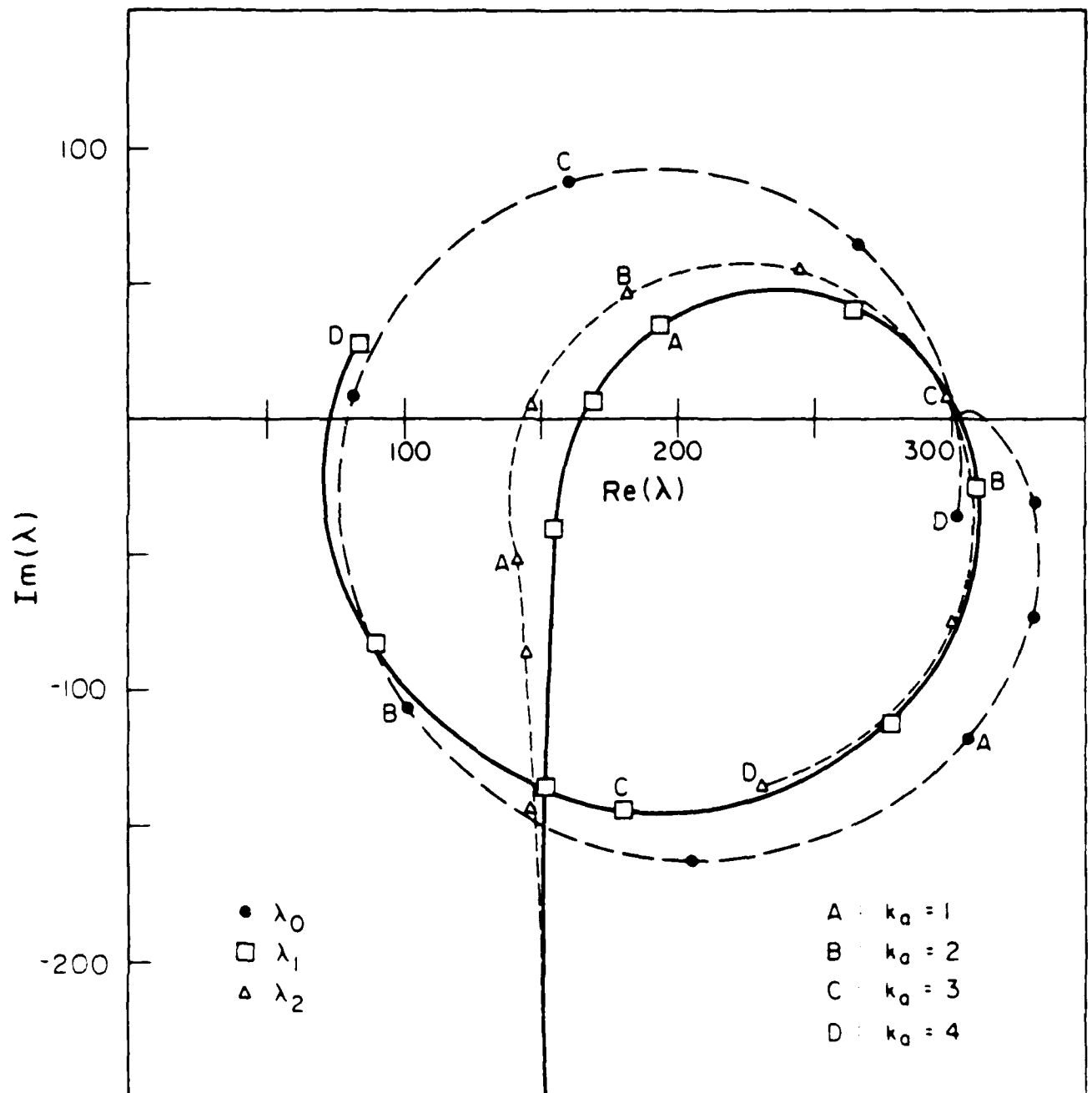


Figure 4.6 Plot of the three dominant eigenvalues of the TE CFIE as a function of  $ka$ .

incident waves, additional components of the fields and current density appear in the equation, doubling its order over that of the original MFIE. In order to implement the procedure of Chapter 2 with the CFIE, it is necessary to double the original order of the matrix equation to be solved at each value of the transform variable  $\gamma$ .

To illustrate the performance of the CFIE, Figure 4.7 presents the CFIE solution for the problem originally presented in Figure 4.4, involving scattering from a circular cylinder at a zero eigenvalue of the original MFIE. Excellent agreement is obtained between the CFIE result and the analytical solution.

#### 4.4 The Augmented-Field Formulation

The EFIE, MFIE, and CFIE formulations discussed above involve boundary conditions imposed on the tangential components of the fields. Other integral equations involving both the tangential and normal field components have been proposed [24]. These equations explicitly enforce the complete set of boundary conditions for a given type of field (E or H) and thus guarantee unique solutions except in a few exceptional situations [24]. These "augmented-field integral equations" deal with either the E-field or the H-field, and have the advantage over the CFIE formulation that the matrix elements are only as complicated as the original EFIE or MFIE formulation. However, when reduced to a matrix form using the method of moments, the system of equations is overdetermined by a factor of 3/2. Thus, they require a special solution algorithm and additional computational time and storage over the original EFIE or MFIE.

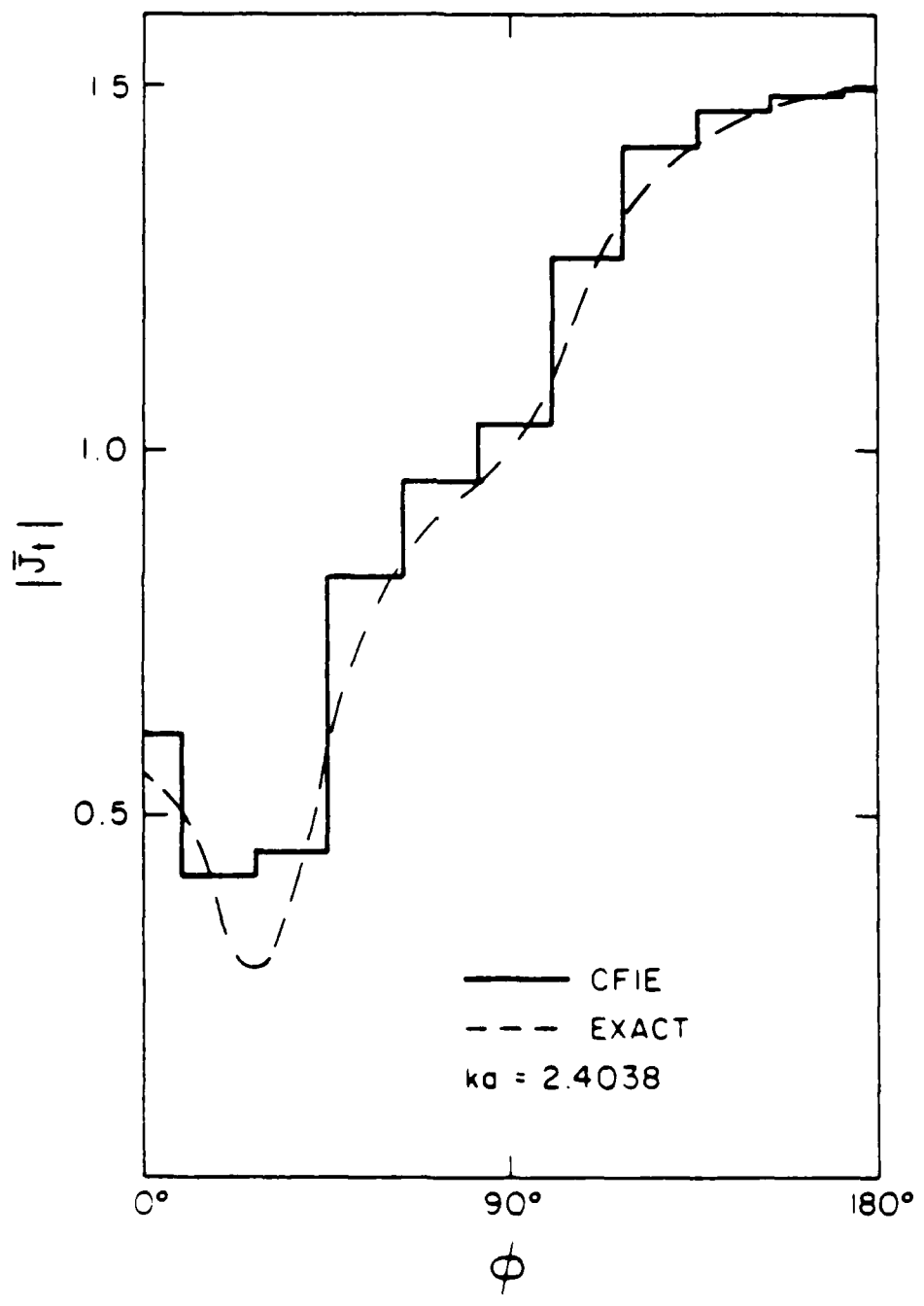


Figure 4.7 Comparison of the CFIE and exact solutions for the TE current density induced on a circular cylinder of radius  $0.3826 \lambda$ .

For example, consider the augmented-magnetic-field equation formulation for TE-wave scattering by perfectly conducting cylinders. For an obliquely incident wave, all three components of the H-field are involved, and both components of electric current density couple to the equations. The system has the form

$$H_z^{inc}(t) = -J_t(t) - \hat{z} \cdot \text{curl} \int \hat{\epsilon}(t') J_t(t') G(\rho) dt' \quad (4.11)$$

$$H_t^{inc}(t) = J_z(t) - \hat{\epsilon} \cdot \text{curl} \int \{ \hat{\epsilon}(t') J_t(t') + \hat{z} J_z(t') \} G(\rho) dt' \quad (4.12)$$

$$H_n^{inc}(t) = -\hat{n} \cdot \text{curl} \int \{ \hat{\epsilon}(t') J_t(t') + \hat{z} J_z(t') \} G(\rho) dt' \quad (4.13)$$

where  $G$  is given in Equation (4.3). When discretized using the method of moments, these equations produce a  $3N \times 2N$  matrix equation, where  $N$  is the number of cells in the cylinder model (see Chapter 2). Expressions for the matrix elements are tabulated in the Appendix. In order to show the accuracy of the procedure, Figure 4.8 presents the augmented-MFIE solution for the previous example of Figures 4.4 and 4.7, involving a circular cylinder excited at a zero eigenvalue of the original MFIE. Excellent agreement is obtained between the exact and numerical results.

In comparison with the CFIE formulation, additional storage is required to implement the augmented-field procedure. The augmented-field approach requires less computational effort than the CFIE, but still considerably more than the original (tangential-field) MFIE. In addition, extra computation is required to process the overspecified system.

#### 4.5 The Combined-Source Formulation

In the formulation of an integral equation, three factors are brought together: an equivalent mathematical source (electric or magnetic current

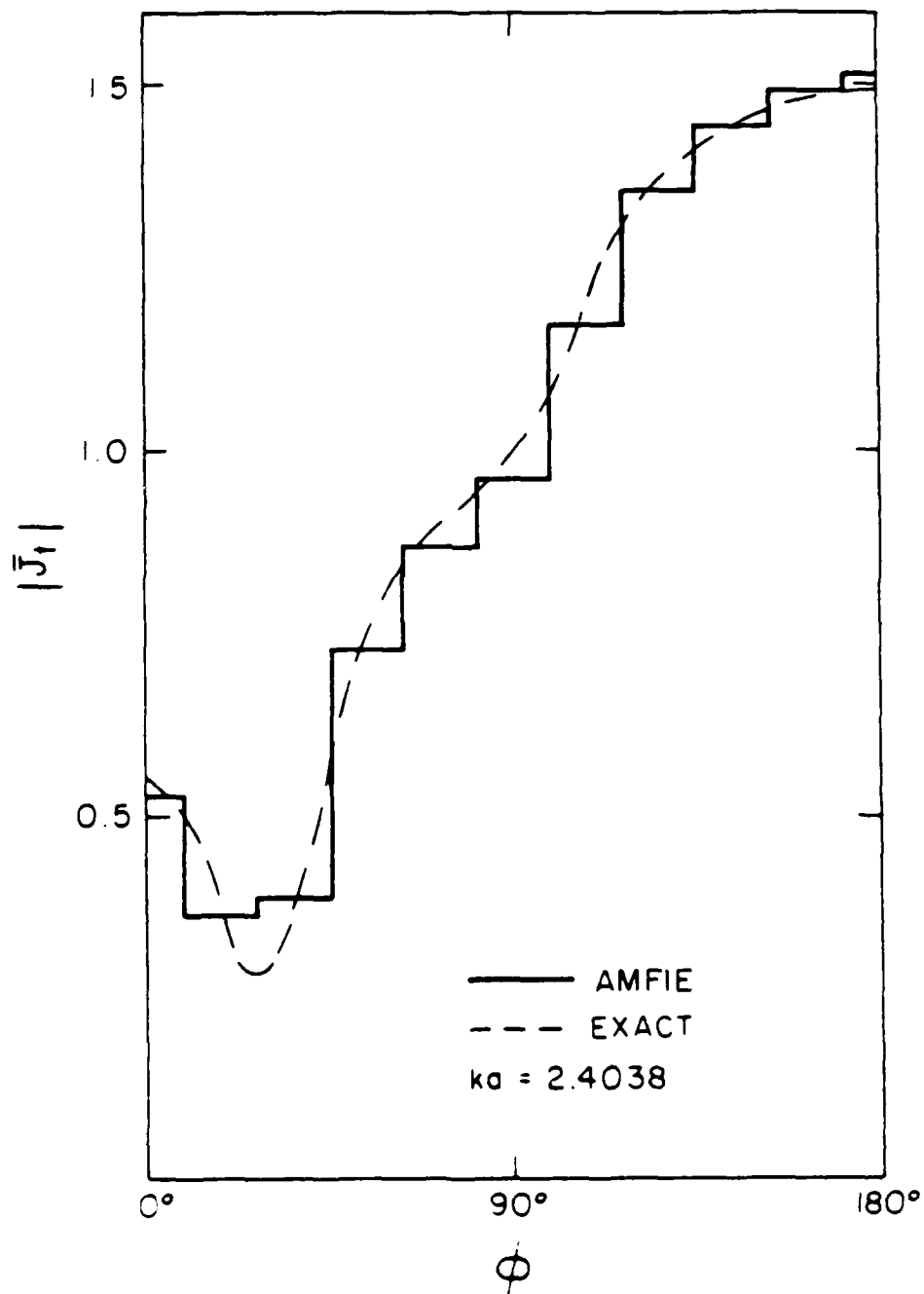


Figure 4.8

Comparison of the augmented-MFIE and exact solutions for the TE current density induced on a circular cylinder of radius  $0.3826 \lambda$ .

density), a source-field relationship (expression for the field at some point in space in terms of an integral over electric or magnetic sources), and a boundary condition on the surface of the scatterer under consideration (such as forcing the tangential E-field at a perfect conductor to vanish). The EFIE, MFIE, CFIE, and augmented-field equations discussed above are formulated in terms of equivalent sources

$$\bar{\mathbf{J}} = \hat{\mathbf{n}} \times \bar{\mathbf{H}} \quad (4.14)$$

$$\bar{\mathbf{K}} = \bar{\mathbf{E}} \times \hat{\mathbf{n}} \quad (4.15)$$

where  $\bar{\mathbf{E}}$  and  $\bar{\mathbf{H}}$  are the fields external to the perfectly conducting scatterer, and  $\bar{\mathbf{J}}$  and  $\bar{\mathbf{K}}$  are the equivalent mathematical electric and magnetic current densities. These equivalent sources are such that the correct fields are produced external to the scatterer, and null fields are produced within the scatterer.

Since we desire to model a perfectly conducting cylinder, it is natural to choose equivalent sources as suggested in Equations (4.14) and (4.15), since the true fields within such a scatterer are zero. However, we could equally represent the true fields external to a scatterer by a different choice of equivalent sources, provided that the field representation within the cylinder did not vanish. Since only the external fields are of interest, the interior fields can be arbitrarily chosen. This arbitrary choice allows a degree of freedom in the selection of equivalent sources, which may be taken to satisfy the constraint

$$\bar{\mathbf{K}} = \beta (\hat{\mathbf{n}} \times \bar{\mathbf{J}}) \quad (4.16)$$

for some nonzero value of  $\beta$ . Mautz and Harrington have shown that this particular choice of equivalent sources may be used with the EFIE for perfectly

conducting scatterers in order to remove the uniqueness problem from the original EFIE [23]. This is possible because no eigencurrents associated with the interior cavity modes satisfy the additional constraint imposed by Equation (4.16).

A drawback to the combined-source approach is that the electric current density  $J$  used within this procedure is not the true electric current density induced upon the scatterer surface. The true electric current density can be found from a secondary calculation once the mathematical sources  $\bar{J}$  and  $\bar{K}$  are identified [23]. However, it is not clear as to how such a choice of equivalent sources might be used in connection with an MFIE, which explicitly requires the true electric current density within the boundary condition built into the integral equation. The matrix equation resulting from a method-of-moments discretization of the combined-source EFIE is of the same order as the original EFIE, but involves more complicated expressions because of additional terms involving equivalent magnetic current density.

#### 4.6 Overspecification at Interior Points

Since the basic "interior resonance" problem is the presence of fields interior to the scatterer geometry at discrete eigenfrequencies, a straightforward solution to the problem is the direct enforcement of a boundary condition throughout the interior region. One such approach has been proposed by Mittra and Klein, who suggest enforcing the condition that the E-field or H-field vanish at a variety of points within the scatterer geometry [17]. Although their original approach requires the overspecification of the boundary conditions and the consequential solution of an overspecified matrix equation, an

alternate procedure has been studied involving the addition of unknowns to balance the additional points [32]. This latter idea has the potential advantage that no special solution algorithm need be incorporated to solve the overdetermined system and that feedback concerning the interior current density (which should vanish if a "good" solution is obtained) is readily available.

The idea of incorporating additional boundary conditions will be explained in the context of the EFIE for transverse-magnetic (TM) scattering from perfectly conducting cylinders. The equation

$$E_z^{\text{inc}}(t) = jk_t \eta \int J_z(t') G(\rho) dt' \quad (4.17)$$

involves the z-component of the electric current density and the z-component of the E-field, and is valid for an arbitrary oblique angle of incidence. G has been defined in Equation (4.3). This surface integral equation suffers from uniqueness problems associated with the TM modes of a perfectly conducting circular cavity. The problem stems from the fact that the internal cavity fields satisfy the boundary condition imposed on the E-field at the scatterer surface, and thus are undesired homogeneous solutions to the EFIE. One possibility for suppressing these cavity fields is to augment the scatterer model (which consists of strips along the desired surface) with the additional perfectly conducting strips throughout the interior. The idea is simply to "short out" any interior fields that might be present.

In practice, this method has the potential advantage that an existing computer program need not be modified in order to remedy the uniqueness problem; only the scatterer model (typically generated external to the computer code that performs the matrix fill and solve) need be changed. The method can also be

used with the MFIE, provided that the interior strips are perfect magnetic conductors instead of perfect electric conductors.

To illustrate the performance of this approach, consider a wave normally incident on a circular cylinder having a circumference of 5.15 wavelengths (near a theoretical cavity resonance). The result due to a straightforward solution of Equation (4.17) in terms of a  $40 \times 40$  matrix is displayed in Figure 4.9 [32]. Clearly, appreciable error is present in the solution due to the cavity resonance. Figure 4.10 displays the result after the cylinder model was augmented with three additional strips [32]. The additional strips have completely eliminated the interior fields from the problem, without a large increase in computational effort.

In order to get a better idea of the actual effect of the additional strips, we could plot the matrix condition number as a function of cylinder size. In practice, it is easier to compute the determinant of the matrix than the true condition number. In most cases, the determinant provides similar information concerning the location of cavity resonances. Figure 4.11 shows a plot of the determinant of the matrix for the examples of Figures 4.9 and 4.10, as the radius of the circular cylinder is varied. There is a sharp null in the determinant in the vicinity of the observed resonance problem, indicative that an eigenvalue of the matrix passes near the origin for that radius. However, the determinant plot for the second matrix (after the model was augmented with three interior strips) also has a sharp null. In fact, aside from a slight shift in the location of the null, the determinant plot looks similar to that for the original matrix. It appears that the additional three strips did not in fact eliminate the resonance, although they did move the location of the resonance enough to eliminate the problem from the example used in Figure 4.10.

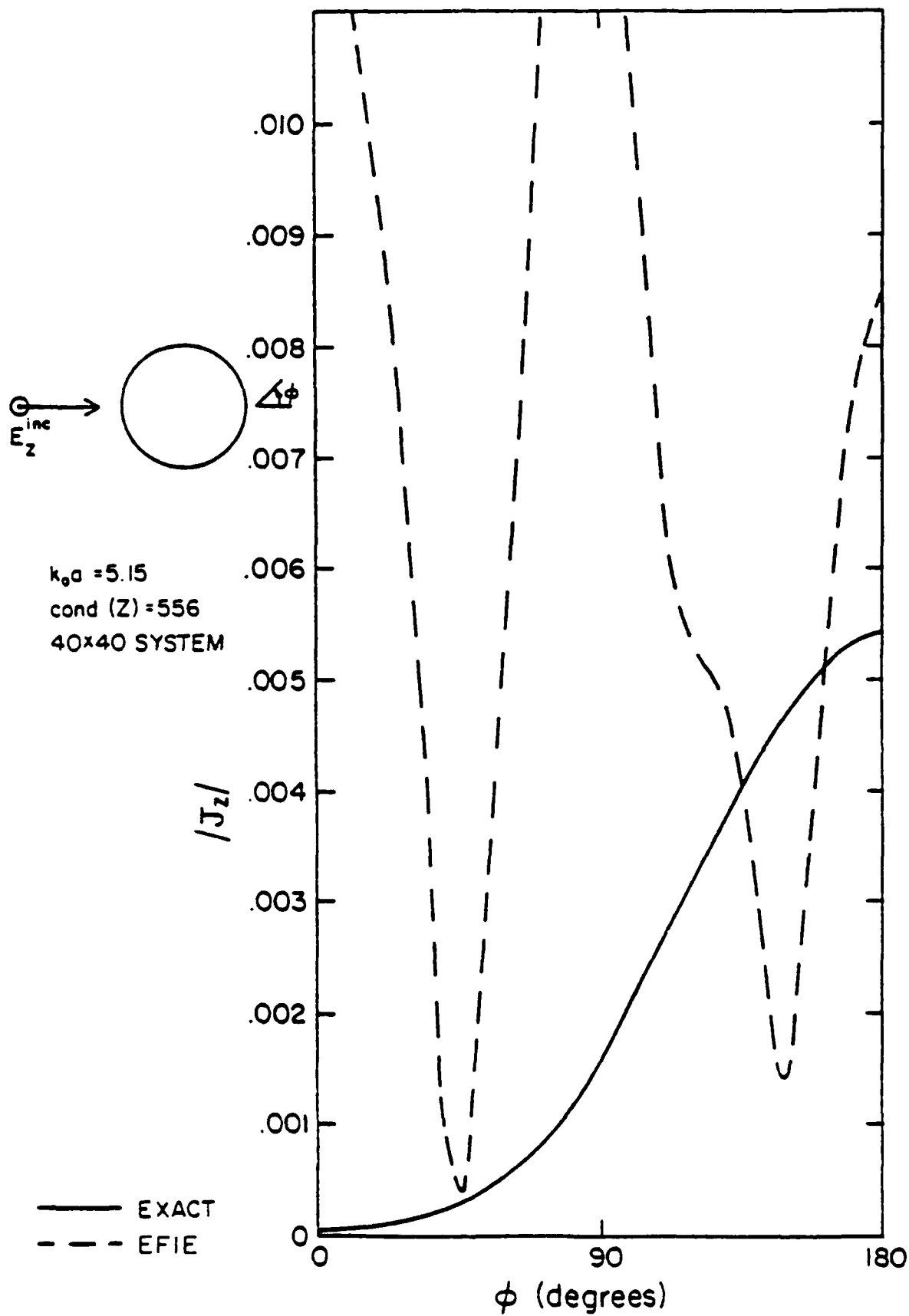


Figure 4.9

Comparison of the EFIE and exact solutions for the TM current density induced on a circular cylinder of radius 0.82.

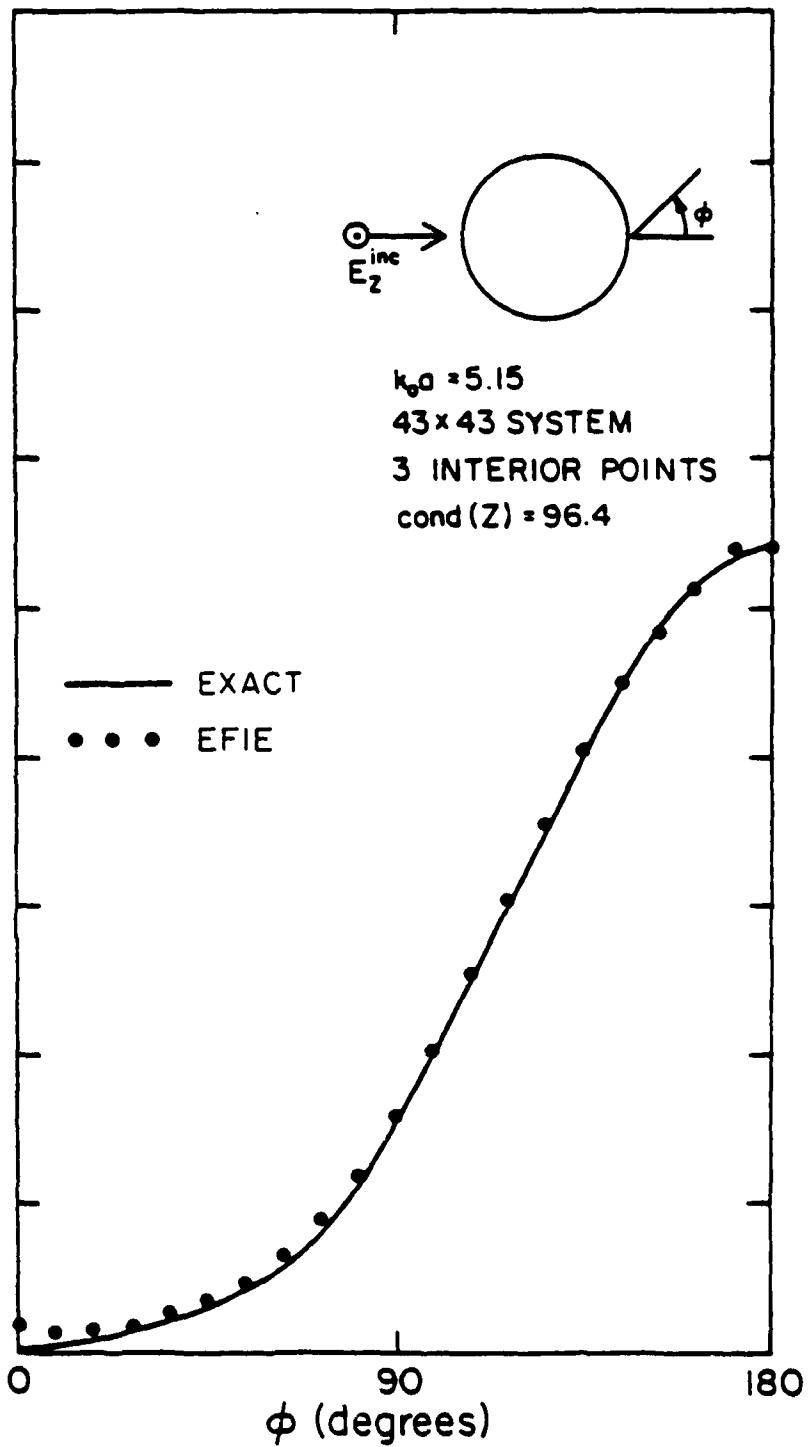


Figure 4.10 Comparison of the EFIE and exact results for the cylinder of Figure 4.9 after three interior strips were added to the 40 strip cylinder model.

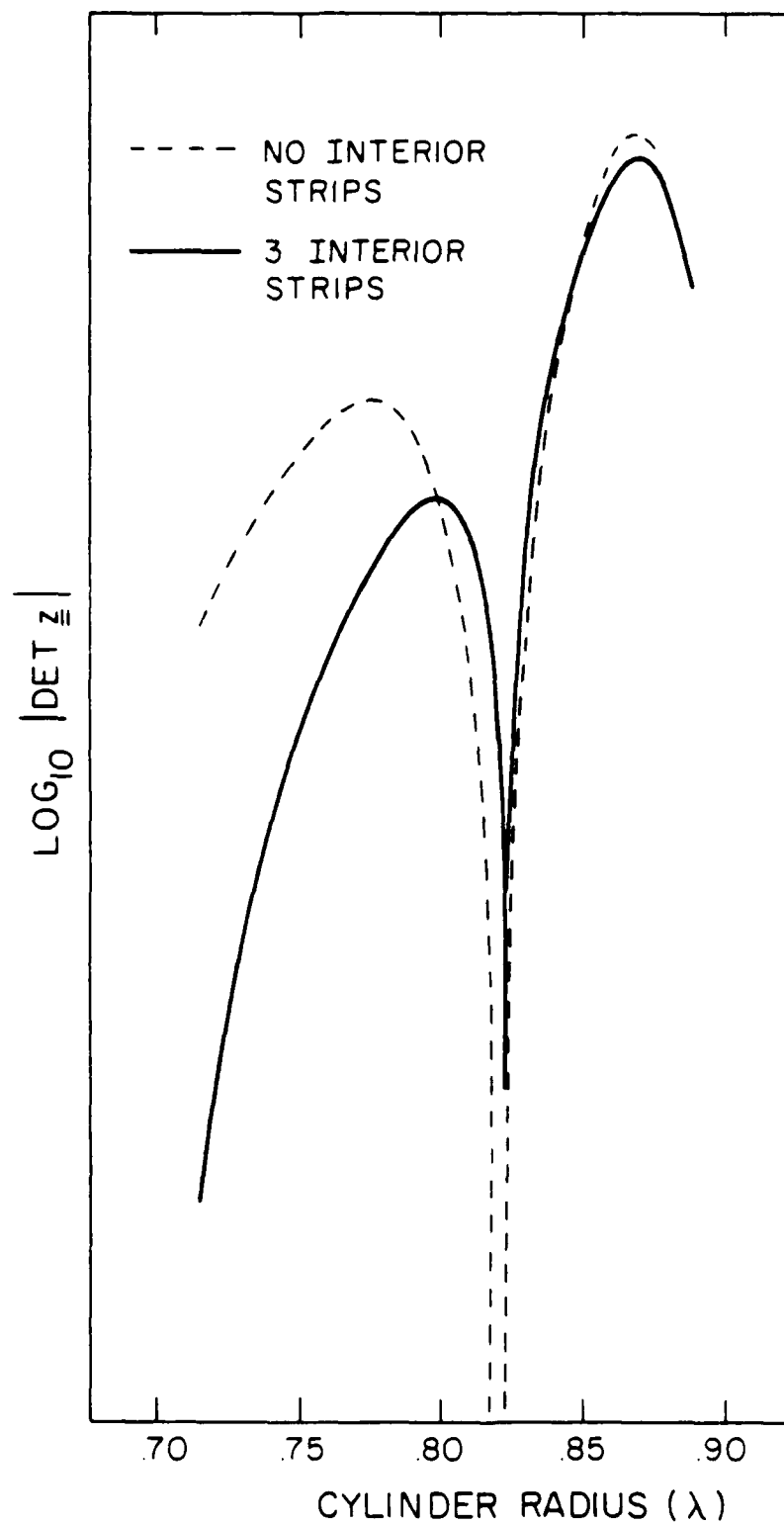


Figure 4.11 Plot of the determinant of the EFIE system matrix for the examples of Figures 4.9 and 4.10, as a function of cylinder radius.

An additional study was carried out to attempt to determine the number of interior strips required to truly eliminate the internal fields. Figure 4.12 depicts a circular cylinder, showing the locations of 16 interior strips. The cylinder surface is modeled with 30 strips. Figure 4.13 shows a plot of the determinant of the matrix before and after the 16 interior strips were added. In this case, the interior strips seem to eliminate the four resonances occurring at the lower frequencies. Unfortunately, it appears that a large density of interior strips is required to actually eliminate cavity resonances in this manner. In practice, the volume of the interior region will increase faster than the surface area, which suggests that a prohibitive number of additional unknowns will be introduced into the problem. Thus, although this procedure can be used to eliminate resonance problems, it will prove to be less efficient for large cylinders than some of the other alternatives outlined above.

#### 4.7 Other Proposed Remedies

Sarkar and Rao have proposed treating the original EFIE and MFIE at eigenfrequencies where they have no unique solutions by a different algorithm that produces the so-called "minimum norm" solution [25]. In theory, this process removes the troublesome eigencurrents from the solution and thus can produce a unique result. Of course, the desired current density might have some contribution from the eigencurrent, and may be incorrect if the resonant eigencurrent is entirely suppressed. For scattering problems, the far-zone fields can be produced (in theory) without the eigencurrent component present; thus, the "minimum norm" procedure can be used for problems where the only desired quantities are the far-zone fields. Unfortunately, the objective under study in

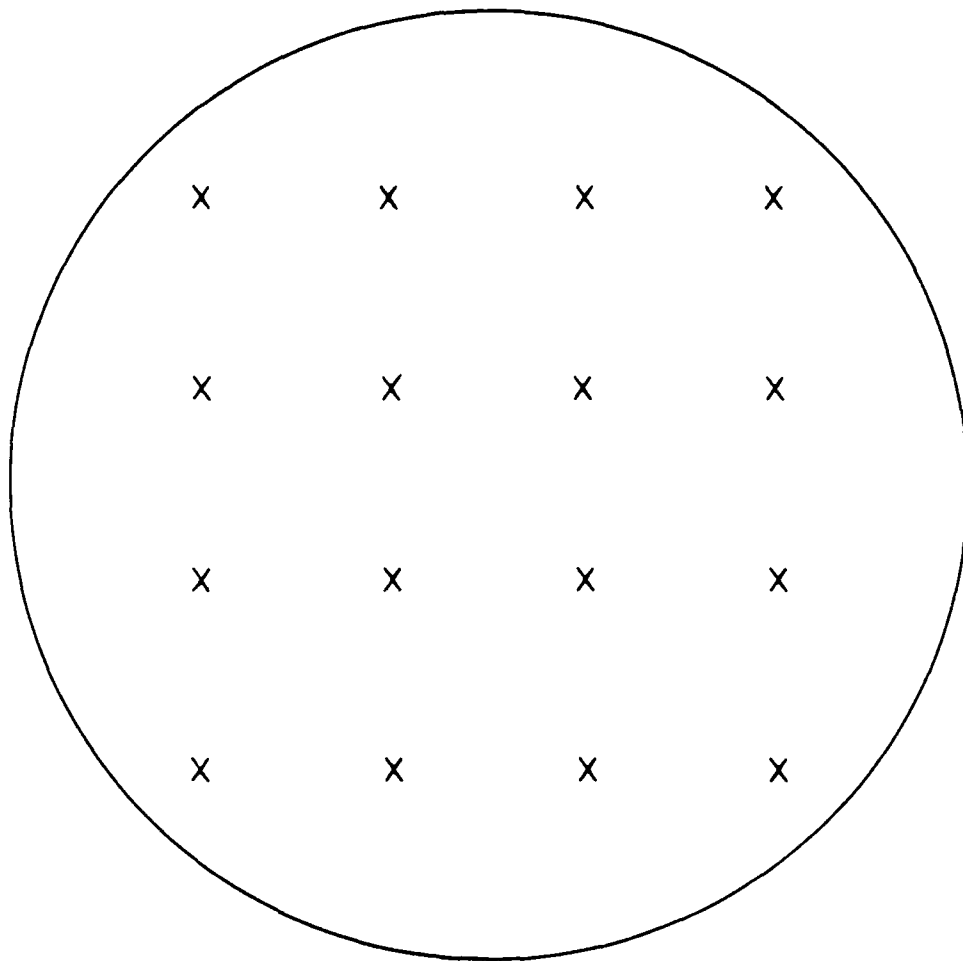


Figure 4.12 Circular cylinder with locations of interior strips identified.

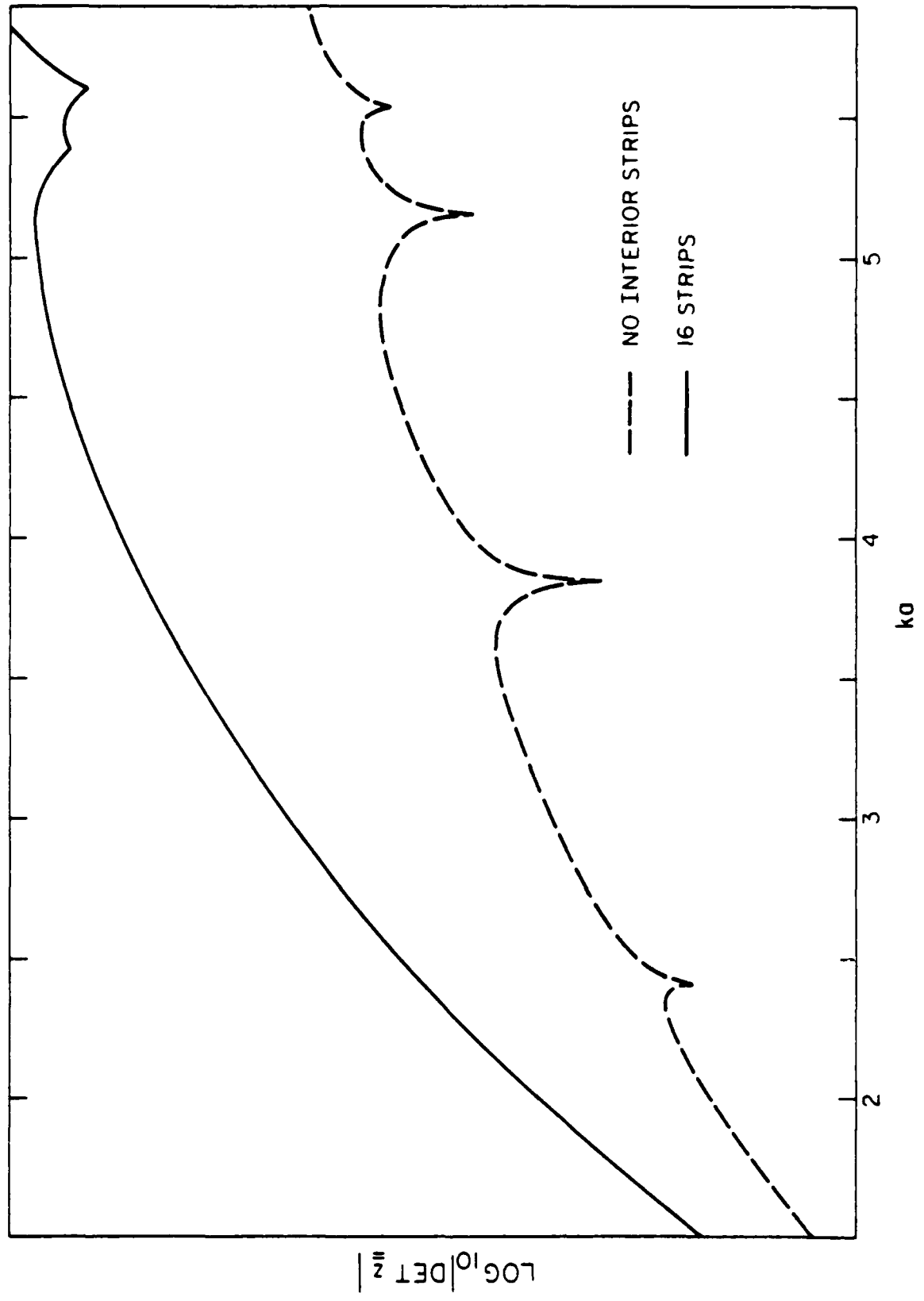


Figure 4.13 Plot of the determinant of the EPIC system matrix for the circular cylinder of Figure 4.12, before and after the 16 interior strips were added to the 30 strip model.

this report involves the computation of the current density on the scatterer. Thus, the "minimum norm" procedure is not satisfactory for the purpose of this investigation.

#### 4.8 Summary

Several remedies to the "interior resonance" problem have been outlined above. From the standpoint of computational efficiency, none of these remedies are as efficient as the original MFIE formulations discussed in Chapters 2 and 3. However, the combined source formulation is not directly compatible with an MFIE, the interior strip approach appears to require too many additional unknowns, and the "minimum norm" procedure yields the incorrect currents on the scatterer. The remaining methods are the CFIE formulation and the augmented-field formulation. The augmented-field formulation will require additional storage over the CFIE and limit the treatment to smaller cylinders. Thus, it appears that the CFIE formulation is the better choice for treating the slots-in-cylinder problem discussed in Chapters 2 and 3. Chapter 5 presents the CFIE implementation for the slot coupling problem.

## 5. COMBINED-FIELD FORMULATION FOR COUPLING BETWEEN AXIAL AND CIRCUMFERENTIAL SLOTS

### 5.1 Combined-Field Formulation for Axial Slot Coupling

An alternate formulation to that presented in Chapter 2 is based on the use of the combined-field integral equation [18], [21] discussed in Chapter 4. Although this procedure requires more computational effort than the MFIE formulation of Chapter 2, it does not suffer from the uniqueness problems that plague the MFIE.

The axial slot coupling problem requires the electric current density induced on a cylinder by a TE excitation. Following the procedure used in Chapter 2, the combined-field equations have the form

$$\begin{aligned} \alpha \tilde{E}_t^{\text{inc}}(t, \gamma) + (1-\alpha) \eta \tilde{H}_z^{\text{inc}}(t, \gamma) &= - (1-\alpha) \eta \tilde{J}_t(t, \gamma) \\ -\eta \left\{ (1-\alpha) \hat{z} \cdot \text{curl} + \alpha \hat{t}(t) \cdot \frac{\text{grad div} + k^2}{jk} \right\} \int \hat{t}(t') \tilde{J}_t(t', \gamma) \tilde{G}(\rho; k, \gamma) dt' \\ - \alpha \eta \hat{t}(t) \cdot \frac{\text{grad div} + k^2}{jk} \int \hat{z} \tilde{J}_z(t', \gamma) \tilde{G}(\rho; k, \gamma) dt' & \quad (5.1) \end{aligned}$$

$$\begin{aligned} (1-\alpha) \eta \tilde{H}_t^{\text{inc}}(t, \gamma) &= (1-\alpha) \eta \tilde{J}_z(t, \gamma) \\ - \eta (1-\alpha) \hat{t}(t) \cdot \text{curl} \int \hat{t}(t') \tilde{J}_t(t', \gamma) \tilde{G}(\rho; k, \gamma) dt' \\ - \eta (1-\alpha) \hat{t}(t) \cdot \text{curl} \int \hat{z} \tilde{J}_z(t', \gamma) \tilde{G}(\rho; k, \gamma) dt' & \quad (5.2) \end{aligned}$$

where  $\tilde{G}(\rho; k, \gamma)$  is defined in Equations (2.5) and (2.6), and  $\alpha$  is a parameter usually taken equal to 0.2. If the cylinder is modeled by a superposition of

flat strips, as depicted in Figure 2.1, and if both components of the current density  $\tilde{J}$  are approximated by a piecewise constant representation over each cell in the model, the CFIE formulation yields the  $2N \times 2N$  matrix equation

$$\begin{bmatrix} \underline{\underline{A}}^{(t)} \\ \underline{\underline{B}}^{(t)} \end{bmatrix} \begin{bmatrix} \underline{\underline{A}}^{(z)} \\ \underline{\underline{B}}^{(z)} \end{bmatrix} = \begin{bmatrix} \underline{\underline{J}}_t \\ \underline{\underline{J}}_z \end{bmatrix} = \begin{bmatrix} \underline{\underline{C}} \\ \underline{\underline{D}} \end{bmatrix} \quad (5.3)$$

having elements

$$A_{mm}^{(t)} = - (1-\alpha) \eta - (1-\alpha) \eta H_z \cdot J_t(0,0) - \alpha E_t \cdot J_t(0,0) \quad (5.4)$$

$$A_{mn}^{(t)} = - (1-\alpha) \eta H_z \cdot J_t(\Delta x, \Delta y) - \alpha E_t \cdot J_t(\Delta x, \Delta y) \quad (5.5)$$

$$A_{mn}^{(z)} = - \alpha E_t \cdot J_z(\Delta x, \Delta y) \quad (5.6)$$

$$B_{mn}^{(t)} = - (1-\alpha) \eta H_t \cdot J_t(\Delta x, \Delta y) \quad (5.7)$$

$$B_{mm}^{(z)} = (1-\alpha) \eta - (1-\alpha) \eta H_t \cdot J_z(0,0) \quad (5.8)$$

$$B_{mn}^{(z)} = - (1-\alpha) \eta H_t \cdot J_z(\Delta x, \Delta y) \quad (5.9)$$

$$C_m = \tilde{VW} \sum_{n=1}^{N_s} \alpha E_t \cdot K_z(\Delta x, \Delta y) + (1-\alpha) \eta H_z \cdot K_z(\Delta x, \Delta y) \quad (5.10)$$

$$D_m = \tilde{VW} \sum_{n=1}^{N_s} (1-\alpha) \eta H_t \cdot K_z(\Delta x, \Delta y) \quad (5.11)$$

where the expressions  $H_z \cdot K_z$ ,  $E_t \cdot K_z$ , etc. are tabulated in the Appendix, and

$$\Delta x = x_m - x_n \quad (5.12)$$

$$\Delta y = y_m - y_n \quad (5.13)$$

The subscripts  $m$  and  $n$  denote the observation and source cells. For convenience, the equivalent magnetic current in the source slot is decomposed into piecewise-constant expansion functions. These source functions are superimposed in Equations (5.10) and (5.11).  $\tilde{V}$  and  $\tilde{W}$  are the weighting factors given in Equations (2.21) and (2.22). Note that the matrix equation must be solved at each value of the transform variable  $\gamma$ , before the admittance can be computed as indicated in Equations (2.23) and (2.24).

## 5.2 Numerical Results for Axial Slot Admittance

The examples for axial slot coupling presented in Section 2.3 will be repeated using the combined-field formulation described above. Note that it is only necessary to use the CFIE formulation over the "visible" portions of the spectrum, i.e.  $\gamma^2 < k^2$ . The MFIE formulation of Chapter 2 will produce unique results for all other values of  $\gamma$ . The first example consisted of a circular cylinder with  $1 \lambda$  radius, containing slots with dimensions  $0.2 \lambda \times 0.5 \lambda$ . Eigenfunction data are presented in Table 2.1. An 88 equal-size cell model is used to represent the cylinder and slot geometries. A plot of the spectral admittance function appears in Figure 2.3. This figure and the experimentation performed in Chapter 2 suggest that the spectrum can be truncated at  $\gamma = 20$  without incurring significant errors.

Table 5.1 shows the CFIE admittance values for two values of the fictitious spatial period. From a comparison with the data presented in Chapter 2, the CFIE results are clearly more accurate than the MFIE values for slot spacings of  $4 \lambda$  and  $8 \lambda$ .

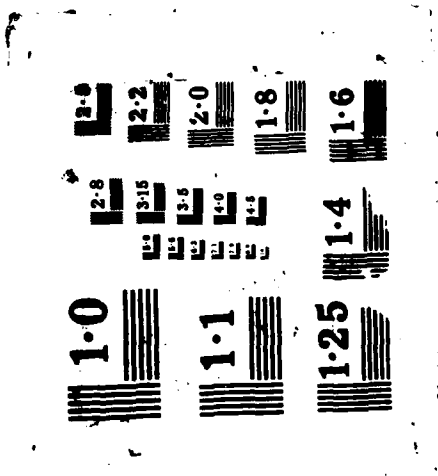
A second example involving a circular cylinder with  $0.7582 \lambda$  radius was examined in Chapter 2 using a 47 cell model to represent the geometry. Slots of dimensions  $0.3048 \lambda$  by  $0.6858 \lambda$  are considered. Tables 2.7 through 2.9 presented MFIE data for admittance, and Table 5.2 presents CFIE data for comparison. Note that the CFIE results change only slightly as the spatial period is varied, in contrast to the large fluctuations in the MFIE data of Chapter 2. Unfortunately, for the slot spacing of  $6 \lambda$ , neither the CFIE or MFIE result for admittance agrees with the eigenfunction value.

### 5.3 Combined-Field Formulation for Circumferential Slot Coupling

The circumferential slot coupling problem requires the solution for the electric current density induced on a cylinder by a transverse magnetic current density. The combined-field equations for this problem as a function of the transform variable  $\gamma$  are

$$\begin{aligned} \alpha \tilde{E}_t^{inc}(t, \gamma) + (1-\alpha) \eta \tilde{H}_z^{inc}(t, \gamma) &= - (1-\alpha) \eta \tilde{J}_t(t, \gamma) \\ &- \eta \left\{ (1-\alpha) \hat{z} \cdot \text{curl} + \alpha \hat{t}(t) \cdot \frac{\text{grad div} + k^2}{jk} \right\} \int \hat{t}(t') \tilde{J}_t(t', \gamma) \\ &- \alpha \eta \hat{t}(t) \cdot \frac{\text{grad div} + k^2}{jk} \int \hat{z} \tilde{J}_z(t', \gamma) \tilde{G}(\rho; k, \gamma) dt' \end{aligned}$$





1.0

1.1

1.25

1.4

1.6

1.8

2.0

2.2

2.8

3.2

3.6

4.0

4.5

TABLE 5.1

A comparison of the numerical results for the mutual admittance between axial slots for different spatial periods. The circular cylinder has  $1 \lambda$  radius and is modeled with 88 cells. The spectrum is truncated at  $\gamma = 20$ . Both slots have  $H = 0.214 \lambda$  and  $W = 0.5 \lambda$ . All slot separations have  $\Delta\phi = 0^\circ$  (CFIE solution). The admittance is given in magnitude (decibels) and angle (degrees.)

$\Delta z$	$\Delta\phi$	$P_z = 20.5 \lambda$	$P_z = 40.5 \lambda$	eigenfunction
$1\lambda$	$0^\circ$	-86.24 / <u>-168.6</u>	-86.22 / <u>-168.6</u>	-87.1 / <u>-171</u>
2	0	-99.16 / <u>-174.8</u>	-99.13 / <u>-174.3</u>	-100.0 / <u>-174</u>
4	0	-111.96 / <u>-176.2</u>	-111.66 / <u>-174.9</u>	-112.4 / <u>-175</u>
8	0	-128.61 / <u>-159.4</u>	-124.32 / <u>-151.0</u>	-124.3 / <u>-174</u>
1	45	-88.31 / <u>-0.4</u>	-88.32 / <u>-0.3</u>	-89.2 / <u>2</u>

TABLE 5.2

A comparison of the numerical results for the mutual admittance between axial slots for different models of the cylinder. The circular cylinder has  $0.7582 \lambda$  radius and is modeled with 47 cells. The spectrum is truncated at  $\gamma = 20$ . All slot separations involve  $\Delta\phi = 0^\circ$  (CFIE solution). The admittance is given in magnitude (decibels) and angle (degrees). Both slots have  $H = 0.3041 \lambda$  and  $W = 0.6858 \lambda$ .

$\Delta z$	$P_z = 40.5 \lambda$	$P_z = 80.5 \lambda$	eigenfunction
$1.524 \lambda$	-91.49 / <u>19.2</u>	-91.50 / <u>19.0</u>	N/A
$3.048 \lambda$	-105.99 / <u>158.9</u>	-105.93 / <u>159.2</u>	N/A
$6.096 \lambda$	-109.72 / <u>177.7</u>	-109.72 / <u>174.5</u>	-118.1 / <u>150</u>

$$\begin{aligned}
& \alpha \tilde{E}_z^{inc}(t, \gamma) + (1-\alpha) \eta \tilde{H}_t^{inc}(t, \gamma) = (1-\alpha) \eta \tilde{J}_z(t, \gamma) \\
& - \eta \left\{ \alpha \hat{z} \cdot \frac{\text{grad div} + k^2}{jk} + (1-\alpha) \hat{t}(t) \cdot \text{curl} \right\} \int \hat{t}(t') \tilde{J}_t(t', \gamma) \tilde{G}(\rho; k, \gamma) dt' \\
& - \eta \left\{ \alpha \hat{z} \cdot \frac{(k^2 - \gamma^2)}{jk} + (1-\alpha) \hat{t}(t) \cdot \text{curl} \right\} \int \hat{z} \tilde{J}_z(t', \gamma) \tilde{G}(\rho; k, \gamma) dt'
\end{aligned} \quad (5.15)$$

where  $\tilde{G}(\rho; k, \gamma)$  is defined in Equations (2.5) and (2.6), and  $\alpha$  is a parameter usually taken equal to 0.2. If the cylinder is modeled by a superposition of flat strips, as depicted in Figure 2.1, and if both components of the current density  $\tilde{J}$  are approximated by a piecewise constant representation over each cell in the model, the CFIE formulation yields the  $2N \times 2N$  matrix equation

$$\begin{bmatrix} \underline{\underline{E}}(t) & \underline{\underline{E}}(z) \\ \underline{\underline{F}}(t) & \underline{\underline{F}}(z) \end{bmatrix} \begin{bmatrix} \underline{\underline{J}}_t \\ \underline{\underline{J}}_z \end{bmatrix} = \begin{bmatrix} \underline{\underline{G}} \\ \underline{\underline{H}} \end{bmatrix} \quad (5.16)$$

having elements

$$E_{mm}^{(t)} = - (1-\alpha) \eta - (1-\alpha) \eta H_z \cdot J_t(0,0) - \alpha E_t \cdot J_t(0,0) \quad (5.17)$$

$$E_{mn}^{(t)} = - (1-\alpha) \eta H_z \cdot J_t(\Delta x, \Delta y) - \alpha E_t \cdot J_t(\Delta x, \Delta y) \quad (5.18)$$

$$E_{mn}^{(z)} = - \alpha E_t \cdot J_z(\Delta x, \Delta y) \quad (5.19)$$

$$F_{mn}^{(t)} = - (1-\alpha) \eta H_t \cdot J_t(\Delta x, \Delta y) - \alpha E_z \cdot J_t(\Delta x, \Delta y) \quad (5.20)$$

$$F_{mm}^{(z)} = (1-\alpha) \eta - (1-\alpha) \eta H_t \cdot J_z(0,0) - \alpha E_z \cdot J_z(0,0) \quad (5.21)$$

$$F_{mn}^{(z)} = - (1-\alpha) \eta H_t \cdot J_z(\Delta x, \Delta y) - \alpha E_z \cdot J_z(\Delta x, \Delta y) \quad (5.22)$$

$$G_m = \tilde{W} \sum_{n=1}^{N_s} \tilde{V}_n \left[ \alpha E_t \cdot K_t(\Delta x, \Delta y) + (1-\alpha) \eta H_z \cdot K_t(\Delta x, \Delta y) \right] \quad (5.23)$$

$$H_m = \tilde{W} \sum_{n=1}^{N_s} \tilde{V}_n [\alpha E_z \cdot K_t(\Delta x, \Delta y) + (1-\alpha) \eta H_t \cdot K_t(\Delta x, \Delta y)] \quad (5.24)$$

where the expressions  $H_z \cdot K_t$ ,  $E_t \cdot K_t$ , etc. are tabulated in the Appendix, and

$$\Delta x = x_m - x_n \quad (5.25)$$

$$\Delta y = y_m - y_n \quad (5.26)$$

$\tilde{V}_n$  and  $\tilde{W}$  are the weighting factors given in Equations (3.9) and (3.23). As was the case with axial slot coupling, the matrix equation must be solved at each value of the transform variable  $\gamma$ .

#### 5.4 Numerical Results for Circumferential Slot Admittance

A circular cylinder having  $1 \lambda$  radius and slots of dimensions  $0.2 \lambda \times 0.5 \lambda$  was considered in Chapter 3. Eigenfunction solutions for admittance are presented in Table 3.1, and data based on the MFIE were presented in Tables 3.2 and 3.3. Table 5.3 presents CFIE data for admittance, using the 88 cell model employed in Chapter 3. Note that the CFIE formulation is only employed over the "visible" portion of the spectrum, i.e.,  $\gamma^2 < k^2$ . The MFIE formulation of Chapter 3 will produce unique results for all other values of  $\gamma$ . The effect of truncating the spectrum at  $\gamma = 20$  is also depicted in Table 5.3. The spectrum for this example is displayed in Figure 3.2.

Chapter 3 considered a second example involving slots in a  $1.517 \lambda$  radius cylinder. The slots were of dimension  $0.3048 \lambda \times 0.6858 \lambda$ , and the cylinder was modeled with 83 cells. Table 3.6 presented eigenfunction data for admittance.

TABLE 5.3

Numerical results for the mutual admittance between circumferential slots as a function of spectrum truncation. The circular cylinder has radius of one wavelength and is modeled with 88 cells. The slots have  $H = 0.2 \lambda$  and  $W = 0.4998 \lambda$ . The spatial period fixed at  $P_z = 40.5 \lambda$ . The admittance is given in magnitude (decibels) and angle (degrees). (CFIE solution)

$\Delta z$	$\Delta \phi$	$\gamma_{\max} \approx 20$	$\gamma_{\max} \approx 30$
$0.5\lambda$	$0^\circ$	$-68.42 / \underline{-118.2}$	$-68.41 / \underline{-118.2}$
1.0	0	$-73.30 / \underline{67.8}$	$-73.35 / \underline{67.7}$
2.0	0	$-78.90 / \underline{70.4}$	$-78.96 / \underline{70.3}$
4.0	0	$-85.17 / \underline{71.6}$	$-85.11 / \underline{71.7}$
8.0	0	$-92.01 / \underline{70.0}$	$-92.06 / \underline{69.9}$
1.0	45	$-82.76 / \underline{-38.1}$	$-82.76 / \underline{-38.1}$

Tables 3.7 and 3.8 presented admittance data based on the MFIE formulation. CFIE data for comparison are presented in Tables 5.4 and 5.5.

CFIE data from these examples agree well with both MFIE and eigenfunction results from Chapter 3. (Neither of the examples of Chapter 3 appears to be affected by the uniqueness problems that the CFIE is intended to remedy; therefore, a significant change in accuracy was not expected.)

#### 5.5 Remarks on Execution Time

Although the programs used to generate the admittance data presented above were tested on several different computers, most of the data was obtained using an AT&T 6300 desktop personal computer with the IBM Professional FORTRAN compiler. The program execution times vary with the period size, the spectrum truncation, and the number of cells in the cylinder model.

The CFIE data presented for axial slot coupling using an 88-cell model, spatial period of  $40.5 \lambda$ , and spectrum truncated at  $\gamma = 20$  required 15 hours of computation. A similar run for circumferential slots required 20 hours. The axial slot data involving a 47-cell model, spatial period of  $40.5 \lambda$ , and  $\gamma_{\max} = 20$  only required about 3 hours of computer time. The circumferential data involving the 83-cell model and spatial period of  $90.5 \lambda$  required about 38 hours of computer time.

#### 5.6 Summary

In an attempt to remediate the uniqueness problems associated with the MFIE formulations of Chapters 2 and 3, a CFIE formulation has been incorporated into

TABLE 5.4

Numerical results for the mutual admittance between circumferential slots as a function of period size. The circular cylinder has radius of one wavelength and is modeled with 83 cells. The slots have  $H = 0.3048 \lambda$  and  $W = 0.6891 \lambda$ . The spectrum is truncated at  $\gamma = 20$ . The admittance is given in magnitude (decibels) and angle (degrees).

(CFIE solution)

$\Delta z$	$P_z = 30.5 \lambda$	$P_z = 60.5$	$P_z = 90.5$
0.38 $\lambda$	-62.95 / <u>-70.7</u>	-62.86 / <u>-71.1</u>	-62.85 / <u>-71.2</u>
0.76	-66.68 / <u>155.4</u>	-66.68 / <u>155.3</u>	-66.69 / <u>155.2</u>
1.52	-72.80 / <u>-117.7</u>	-72.36 / <u>-116.9</u>	-72.23 / <u>-117.1</u>
2.29	-74.45 / <u>-27.4</u>	-74.46 / <u>-28.2</u>	-74.47 / <u>-28.6</u>
3.05	-78.80 / <u>51.5</u>	-78.02 / <u>54.6</u>	-77.76 / <u>54.6</u>

TABLE 5.5

Numerical results for the mutual admittance between circumferential slots as a function of period size. The circular cylinder has radius of one wavelength and is modeled with 83 cells. The slots have  $H = 0.3048 \lambda$  and  $W = 0.6891 \lambda$ . The spectrum is truncated at  $\gamma = 20$ . The admittance is given in magnitude (decibels) and angle (degrees). (CFIE solution)

$\Delta z$	$P_z = 30.5 \lambda$	$P_z = 60.5$	$P_z = 90.5$
8.38 $\lambda$	-85.11 $\angle$ <u>-44.2</u>	-84.77 $\angle$ <u>-54.6</u>	-84.63 $\angle$ <u>-57.8</u>
9.14	-85.03 $\angle$ <u>-5.7</u>	-85.76 $\angle$ <u>5.3</u>	-85.55 $\angle$ <u>7.7</u>
9.91	-87.24 $\angle$ <u>133.0</u>	-86.53 $\angle$ <u>117.8</u>	-86.29 $\angle$ <u>113.9</u>
10.67	-84.97 $\angle$ <u>168.2</u>	-86.21 $\angle$ <u>177.2</u>	-86.16 $\angle$ <u>179.4</u>
11.43	-90.20 $\angle$ <u>-45.5</u>	-88.66 $\angle$ <u>-69.0</u>	-88.26 $\angle$ <u>-74.0</u>

the slot coupling problem. Data have been presented for four cylinder geometries in order to judge the accuracy of the numerical admittance results. In general, the CFIE admittance data appear to be significantly more reliable than the MFIE data presented in Chapters 2 and 3. Use of the CFIE formulation eliminates the large fluctuations in admittance as the spatial period is varied.

For axial slot coupling, the CFIE results are in excellent agreement with the eigenfunction values for slots spaced within 4 wavelengths along the cylinder axis. For slots spaced 6 and 8 wavelengths apart, errors in magnitude or phase are observed in both the MFIE and CFIE solutions. For circumferential slots, excellent agreement was obtained for all the slot separations considered.

Because only a limited number of eigenfunction values were available for comparison [5], we did not attempt an extensive investigation to determine the regions of validity of the slot coupling formulation. The values in error seem to involve coupling below the -115 dB level. For the examples considered here, the coupling only fell below -115 dB for axial slots. Additional study is needed in order to determine whether this represents a fundamental resolution limit or some other problem.

The purpose of comparing the numerical results to eigenfunction data was to validate the computer programs and investigate how large the spatial period and spectrum must be to ensure accurate results. Good agreement for closely-spaced slots suggests that the computer programs are debugged. The extent of the spectrum and spatial period can be determined from the data presented in Chapters 2 and 3. When using cylinder geometries different from those previously studied, these parameters may require additional investigation.

## 6. ADMITTANCE BETWEEN SLOTS IN NONCIRCULAR CYLINDERS

Previous chapters have presented a formulation for the analysis of the mutual coupling between slots in arbitrarily shaped cylinders. Data have been generated for slots in circular cylinders, which facilitated a comparison between numerical data and eigenfunction results for admittance. These comparisons appear to validate the theory and the computer programs, at least for slots that are relatively closely spaced in the  $z$ -dimension. This chapter presents admittance data from the numerical procedure for two cases: slots in square cylinders and slots in pie-shaped cylinders. These examples have been selected to illustrate the flexibility of the procedure. In addition, as these cylinder and slot geometries are simple to describe, these examples permit future comparisons between the numerical data and other data, i.e., that obtained by measurement or other analytical, asymptotic, or numerical methods.

Consider a square cylinder containing axial slots located along the center line of a common face. The cylinder has a side dimension of 1.5 wavelengths, and the slots are of dimension  $0.3 \times 0.5$  wavelength. Sixty equal-sized cells were used to represent the cylinder for numerical analysis. Data for admittance are presented in Table 6.1 for several slot separations. Data for the admittance between circumferential slots in the same square cylinder are presented in Table 6.2. The circumferential slots are of dimension  $0.3 \times 0.5$  wavelength, and are located along the centerline of a common face of the square cylinder. Both Table 6.1 and Table 6.2 illustrate the effect of the fictitious period size on the numerical data, as the results for large slot separations are clearly not accurate for small period sizes.

TABLE 6.1

Numerical results for the mutual admittance between axial slots as a function of period size. The square cylinder has side dimension of 1.5 wavelengths and is modeled with 60 cells. The slots have  $H = 0.3 \lambda$  and  $W = 0.5 \lambda$ . The spectrum is truncated at  $\gamma = 20$ . Slot separation  $\Delta t = 0$ . The admittance is given in magnitude (decibels) and angle (degrees). (CFIE solution)

$\Delta z$	$P_z = 40.5$	$P_z = 80.5$
$1 \lambda$	-83.80 / <u>-150.9</u>	-83.77 / <u>-150.9</u>
2	-96.79 / <u>144.6</u>	-96.66 / <u>145.0</u>
4	-103.87 / <u>166.0</u>	-103.56 / <u>166.2</u>
8	-114.29 / <u>-171.8</u>	-113.68 / <u>-176.7</u>
16	-123.73 / <u>-119.4</u>	-124.60 / <u>-111.6</u>

TABLE 6.2

Numerical results for the mutual admittance between circumferential slots as a function of period size. The square cylinder has side dimension of 1.5 wavelengths and is modeled with 60 cells. The slots have  $H = 0.3 \lambda$  and  $W = 0.5 \lambda$ . The spectrum is truncated at  $\gamma = 20$ . Slot separation  $\Delta t = 0$ . The admittance is given in magnitude (decibels) and angle (degrees). (CFIE solution)

$\Delta z$	$P_z = 40.5$	$P_z = 80.5$
1 $\lambda$	-73.47 / <u>82.8</u>	-72.97 / <u>80.0</u>
2	-82.77 / <u>98.0</u>	-81.63 / <u>88.5</u>
4	-94.43 / <u>25.3</u>	-89.06 / <u>32.3</u>
8	-96.09 / <u>13.1</u>	-89.90 / <u>26.1</u>
16	-103.13 / <u>4.2</u>	-92.51 / <u>25.3</u>

The cross section of a pie-shaped cylinder is depicted in Figure 6.1. Data for the admittance between axial slots and circumferential slots in such a cylinder are presented in Tables 6.3 and 6.4, respectively. In these examples, the cylinder radius  $a$  is equal to 2 wavelengths, and the angle  $\theta$  defining the arclength of the pie shape is 21.827 degrees (refer to Figure 6.1 for the definitions of these parameters). A total of 50 equal-sized cells were used to represent the cylinder for the purpose of numerical analysis. The slots were located along the center line of one of the flat faces of the cylinder, and the dimensions of the slots were  $0.2857 \times 0.5$  wavelength for the axial case, and  $0.3 \times 0.4762$  wavelength for the circumferential case.

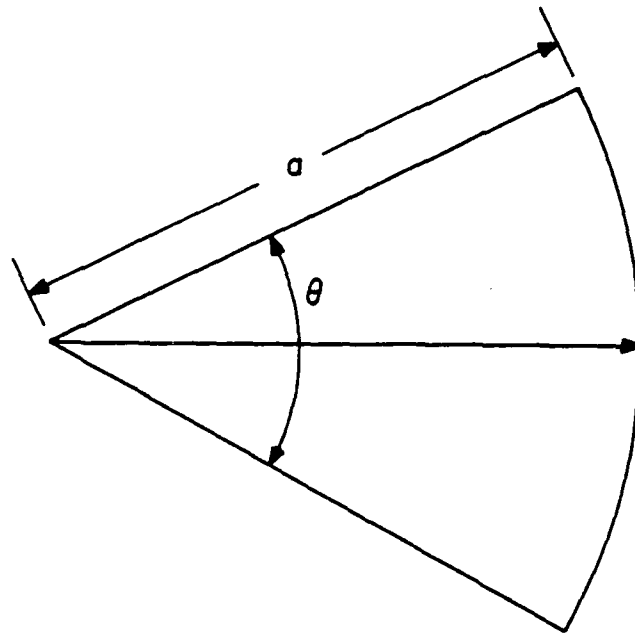


Figure 6.1 Geometry of pie-shaped cylinder.

TABLE 6.3

Numerical results for the mutual admittance between axial slots as a function of period size. The pie-shaped cylinder has  $2\lambda$  radius and an arc length of  $21.83^\circ$ . It is modeled with 50 equal-sized cells. Slot separation:  $\Delta t = 0^\circ$  (CFIE solution). The admittance is given in magnitude (decibels) and angle (degrees). Both slots have  $H = 0.2857$  and  $W = 0.5$  wavelength.

$\Delta z$	$P_z = 40.5 \lambda$	$P_z = 80.5 \lambda$
$1 \lambda$	-82.20 / <u>174.9</u>	-82.20 / <u>174.9</u>
2	-93.92 / <u>-135.8</u>	-93.93 / <u>-135.9</u>
4	-112.35 / <u>104.9</u>	-112.32 / <u>105.4</u>
8	-118.30 / <u>164.2</u>	-117.79 / <u>161.0</u>
16	-147.23 / <u>72.3</u>	-140.83 / <u>-166.4</u>

TABLE 6.4

Numerical results for the mutual admittance between circumferential slots as a function of period size. The pie-shaped cylinder has radius equal to 2.0 wavelengths and an arc length of  $21.83^\circ$ . It is modeled with 50 equal-sized cells. The slots have  $H = 0.3 \lambda$  and  $W = 0.4762 \lambda$ . The slot separation is  $\Delta t = 0^\circ$ . The admittance is given in magnitude (decibels) and angle (degrees). (CFIE solution)

$\Delta z$	$P_z = 40.5 \lambda$	$P_z = 80.5 \lambda$
$1 \lambda$	-73.51 / <u>80.1</u>	-73.39 / <u>79.8</u>
2	-78.60 / <u>86.2</u>	-78.41 / <u>85.6</u>
4	-87.08 / <u>108.9</u>	-86.69 / <u>106.0</u>
8	-95.08 / <u>71.2</u>	-93.57 / <u>69.0</u>
16	-125.22 / <u>-178.6</u>	-108.34 / <u>55.8</u>

## 7. CONCLUSIONS AND SUGGESTED FUTURE WORK

This report describes an investigation of a numerical procedure to estimate mutual admittance between slots in cylinders having arbitrary shape. Since this study was of a preliminary nature, one initial goal addressed the feasibility of formulating the problem in this fashion. The accuracy of the approach has been confirmed by comparisons between numerical data and previously published results. The method does require a large amount of computational effort relative to similar methods that have been proposed for treating restricted geometries. However, none of these alternative approaches can easily treat the arbitrary cylindrical shapes of interest. Therefore, the computational effort is reasonable, at least for cylinders of moderate size. In summary, it appears feasible to treat the slot coupling problem in the manner proposed above.

Initially, the formulation involved the numerical solution of a magnetic-field integral equation (MFIE). However, erratic results were observed and attributed to uniqueness problems with the MFIE. A variety of alternative approaches were investigated, and a combined-field integral equation (CFIE) was selected as a suitable replacement for the MFIE. Although this choice required an increase in computational effort, results based on the CFIE formulation appear stable and accurate.

Because published data for slot admittance were only available for cases involving closely spaced slots, questions remain concerning the validity of this

numerical formulation for the admittance between widely spaced slots. Future work should address this issue, perhaps by generating additional eigenfunction data for circular cylinders with which to validate the procedure over a wide range of parameters. In addition, it is desirable to investigate slots in non-circular cylinders for validation purposes, perhaps by comparing numerical data to measured results. Data for slots in noncircular cylinders have been provided to facilitate such a comparison.

## 8. REFERENCES

- [1] C. G. Commatas and J. N. Sahalos, "Mutual coupling and radiation patterns of two slots asymmetrically located on a square plate," IEEE Trans. Antennas Propagat., vol. AP-31, pp. 531-535, May 1983.
- [2] K. E. Golden, G. E. Stewart, and D. C. Pridmore-Brown, "Approximate techniques for the mutual admittance of slot antennas on metallic cones," IEEE Trans. Antennas Propagat., vol. AP-22, pp. 43-48, January 1974.
- [3] S. W. Lee, "Mutual admittance of slots on a cone: solution by ray technique," IEEE Trans. Antennas Propagat., vol. AP-26, pp. 768-773, November 1978.
- [4] G. E. Stewart and K. E. Golden, "Mutual admittance for axial rectangular slots in a large conducting cylinder," IEEE Trans. Antennas Propagat., vol. AP-19, pp. 120-122, January 1971.
- [5] S. W. Lee, S. Safavi-Naini, and R. Mittra, "Mutual admittance between slots on a cylinder," Electromagnetics Laboratory Report No. 77-8, UILU-ENG-77-2549, Dept. of Electrical and Computer Engineering, University of Illinois, Urbana, IL., March 1977.
- [6] S. W. Lee and S. Safavi-Naini, "Approximate asymptotic solution of surface field due to a magnetic dipole on a cylinder," IEEE Trans. Antennas Propagat., vol. AP-26, pp. 593-598, July 1978.
- [7] T. S. Bird, "Comparison of asymptotic solutions for the surface field excited by a magnetic dipole on a cylinder," IEEE Trans. Antennas Propagat., vol. AP-32, pp. 1237-1244, November 1984.
- [8] T. S. Bird, "Accurate asymptotic solution for the surface field due to apertures in a conducting cylinder," IEEE Trans. Antennas Propagat., vol. AP-33, pp. 1108-1117, October 1985.
- [9] K. Inami, K. Sawaya, and Y. Mushiake, "Mutual coupling between rectangular slot antennas on a conducting concave spherical surface," IEEE Trans. Antennas Propagat., vol. AP-30, pp. 927-933, September 1982.
- [10] P. H. Pathak and N. Wang, "Ray analysis of mutual coupling between antennas on a convex surface," IEEE Trans. Antennas Propagat., vol. AP-29, pp. 911-922, November 1981.
- [11] S. W. Lee, "A review of GTD calculation of mutual admittance of slot conformal array," Electromagnetics, vol. 2, pp. 85-127, 1982.
- [12] C. D. McGillem and G. R. Cooper, Continuous and Discrete Signal and System Analysis. New York: Holt, Rinehart and Winston, Inc., 1974.

- [13] I. S. Gradshteyn and I. M. Ryzhik, Table of Integrals, Series, and Products. New York: Academic Press, 1980, pp. 472.
- [14] R. F. Harrington, Field Computation by Moment Methods. Malabar, Fla.: R. E. Krieger, 1982 Reprint.
- [15] M. G. Andreasen, "Scattering from parallel metallic conducting cylinders with arbitrary cross sections," IEEE Trans. Antennas Propagat., vol. AP-12, pp. 746-754, 1964.
- [16] W. Cheney and D. Kincaid, Numerical Mathematics and Computing. Monterey, CA: Brooks/Cole Publishing, 1980.
- [17] R. Mittra and C. A. Klein, "Stability and convergence of moment method solutions," in Numerical and Asymptotic Techniques in Electromagnetics, ed. R. Mittra. New York: Springer-Verlag, 1975.
- [18] J. R. Mautz and R. F. Harrington, "H-field, E-field, and combined-field solutions for conducting bodies of revolution," A. E. U., vol. 32, pp. 157-163, 1978.
- [19] K. K. Mei and J. G. Van Bladel, "Scattering by perfectly-conducting rectangular cylinders," IEEE Trans. Antennas Propagat., vol. AP-11, pp. 185-192, March 1963.
- [20] M. G. Andreasen, "Comments on 'Scattering by conducting rectangular cylinders,'" IEEE Trans. Antennas Propagat., vol. AP-12, pp. 235-236, March 1964.
- [21] K. M. Mitzner, "Numerical solution of the exterior scattering problem at eigenfrequencies of the interior problem," Digest of the 1968 Radio Science Meeting, Boston, MA, p. 75, September 1968.
- [22] J. C. Bolomey and W. Tabbara, "Numerical aspects on coupling complementary boundary value problems," IEEE Trans. Antennas Propagat., vol. AP-21, pp. 356-363, May 1973.
- [23] J. R. Mautz and R. F. Harrington, "A combined-source formulation for radiation and scattering from a perfectly conducting body," IEEE Trans. Antennas Propagat., vol. AP-27, pp. 445-454, July 1979.
- [24] A. D. Yaghjian, "Augmented electric- and magnetic-field equations," Radio Science, vol. 16, pp. 987-1001, November 1981.
- [25] T. K. Sarkar and S. M. Rao, "A simple technique for solving E-field integral equations for conducting bodies at internal resonances," IEEE Trans. Antennas Propagat., vol. AP-30, pp. 1250-1254, November 1982.
- [26] H. A. Schenk, "Improved integral equation formulation for acoustic radiation problem," J. Acoust. Soc. Am., vol. 44, pp. 41-58, 1968.

- [27] F. H. Fenlon, "Calculation of the acoustic radiation field at the surface of a finite cylinder by the method of weighted residuals," Proc. IEEE, vol. 57, pp. 291-306, March 1969.
- [28] A. F. Peterson and R. Mittra, "Method of conjugate gradients for the numerical solution of large body electromagnetic scattering problems," J. Opt. Soc. Am. A, vol. 2, pp. 971-977, June 1985.
- [29] A. F. Peterson and R. Mittra, "Iterative based computational methods for electromagnetic scattering from individual or periodic structures," IEEE J. Oceanic Engineering, Special Issue on Electromagnetic and Acoustic Scattering, (to appear April, 1987).
- [30] R. F. Harrington, Time-harmonic Electromagnetic Fields. New York: McGraw-Hill, 1961.
- [31] A. F. Peterson, "Eigenvalue projection theory for linear operator equations of electromagnetics," Electromagnetic Comm. Lab. Tech. Rep., University of Illinois, Urbana, IL (in preparation).
- [32] A. F. Peterson and R. Mittra, "On the method of conjugate gradients for scattering by PEC cylinders," Electromagnetics Lab. Tech. Rep. 84-3, UILU-ENG-84-2540, University of Illinois, Urbana, IL, January 1984.

**APPENDIX: SOURCE-FIELD RELATIONSHIPS FOR CYLINDERS ILLUMINATED BY  
AN OBLIQUELY INCIDENT FIELD**

The following is a compilation of formulas for the various field components produced by a single strip-cell of constant current density radiating in space. These expressions are used when calculating the moment-method matrix elements for cylindrical scattering problems, under the condition that the z-dependence of the excitation is

$$e^{jyz} \tag{A.1}$$

Thus, the incident field may be a plane wave impinging on the scatterer from an oblique angle (not perpendicular to the cylinder axis). This particular z-dependence also arises if a Fourier transformation in z is used to replace a three-dimensional problem involving an infinite cylinder by the superposition of two-dimensional problems.

Figure A.1 illustrates the geometry under consideration. The strip-cell of unit current density is centered at the origin, is of cross-sectional length 'W,' and is oriented so that its outward normal vector makes a polar angle ' $\phi$ ' with the  $\hat{x}$  axis (outward must be defined in the context of a closed cylinder with an inside and outside; our strip is considered to be one of a number modeling such a cylinder). The field components of interest are the  $\hat{z}$  and  $\hat{T}$  components of the electric ( $\vec{E}$ ) and magnetic ( $\vec{H}$ ) fields at some observation point (x,y), where  $\hat{T}$  is the tangent vector to a similar strip with outward normal vector given by the polar angle ' $\psi$ .' The source may be the  $\hat{z}$  or  $\hat{t}$  component of magnetic or electric current density. We consider only the case in which the current density is constant on the strip.

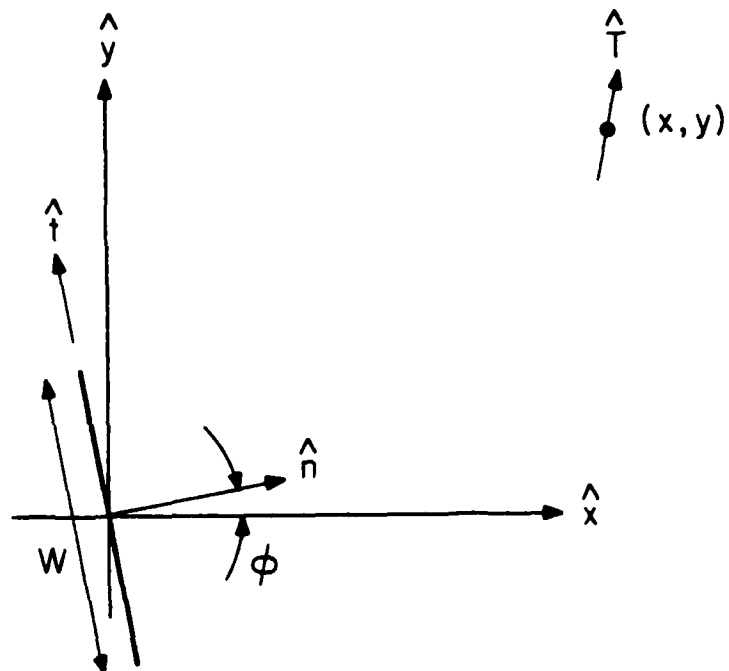


Figure A.1 Geometry used for the source-field relationships.

The notation employed will identify both the source component and the field component. For example,  $H_z \cdot J_z$  denotes the  $\hat{z}$ -component of the  $\bar{H}$ -field produced by the  $\hat{z}$ -component of electric current density. Appropriate expressions for the fields produced by sources are found in terms of the vector potentials  $\bar{A}$  and  $\bar{F}$

$$\bar{H} = \text{curl } \bar{A} + \frac{\text{grad div} + k^2}{jk\eta} \bar{F} \quad (\text{A.2})$$

$$\bar{E} = \eta \frac{\text{grad div} + k^2}{jk} \bar{A} - \text{curl } \bar{F} \quad (\text{A.3})$$

where the vector potentials are defined

$$\bar{A}(x, y) = \int_{s=-W/2}^{W/2} [\hat{z} J_z(s) + \hat{t} J_t(s)] \tilde{G}(R; k, \gamma) ds \quad (\text{A.4})$$

$$\bar{F}(x, y) = \int_{s=-W/2}^{W/2} [\hat{z} K_z(s) + \hat{t} K_t(s)] \tilde{G}(R; k, \gamma) ds \quad (\text{A.5})$$

and

$$\tilde{G}(R; k, \gamma) = \begin{cases} \frac{1}{4j} H_0^{(2)}(R \sqrt{k^2 - \gamma^2}), & k^2 > \gamma^2 \\ \frac{1}{2\pi} K_0(R \sqrt{\gamma^2 - k^2}), & \gamma^2 > k^2 \end{cases} \quad (\text{A.6})$$

$$R = \sqrt{(x + s \sin \phi)^2 + (y - s \cos \phi)^2} \quad (\text{A.7})$$

In Equation (A.6), H refers to the Hankel function and K the modified Bessel function of the second kind.

Because of the assumed  $e^{i\gamma z}$  dependence, any derivatives with respect to  $z$  in the 'curl,' 'grad,' and 'div' operations are replaced by multiplications with ' $j\gamma$ .' In some cases, derivatives will be transferred to the Green's function in

Equation (A.6), and we note that

$$\tilde{G}(R; k, \gamma) = \begin{cases} -\frac{\sqrt{k^2 - \gamma^2}}{4j} H_1^{(2)}(R \sqrt{k^2 - \gamma^2}), & k^2 > \gamma^2 \\ -\frac{\sqrt{\gamma^2 - k^2}}{2\pi} K_1(R \sqrt{\gamma^2 - k^2}), & \gamma^2 > k^2 \end{cases} \quad (\text{A.8})$$

For explicit calculations, the vectors  $\hat{e}$  and  $\hat{T}$  are defined

$$\hat{e} = -\hat{x} \sin \phi + \hat{y} \cos \phi \quad (\text{A.9})$$

$$\hat{T} = -\hat{x} \sin \psi + \hat{y} \cos \psi \quad (\text{A.10})$$

The  $\hat{z}$ -component of the  $\bar{H}$ -field produced at  $(x, y)$  by a  $\hat{z}$ -component of magnetic current density on the strip of Figure A.1 is given by

$$H_z \cdot K_z(x, y) = \frac{k^2 - \gamma^2}{jk\eta} \int_{s=-W/2}^{W/2} \tilde{G}(R; k, \gamma) ds \quad (\text{A.11})$$

where  $\tilde{G}$  is defined in Equation (A.6). A closed-form expression for Equation (A.11) is not available, and in general it must be evaluated numerically.

However, in many cases it can be approximated by

$$H_z \cdot K_z(x, y) \approx \frac{(k^2 - \gamma^2)}{jk\eta} W \tilde{G}(\rho; k, \gamma), \quad \rho \neq 0 \quad (\text{A.12})$$

where

$$\rho = \sqrt{x^2 + y^2} \quad (\text{A.13})$$

and

$$H_z \cdot K_z(0, 0) \approx -\frac{(k^2 - \gamma^2)}{4k\eta} W \begin{cases} 1 - j \frac{2}{\pi} \ln \left( \frac{W \sqrt{k^2 - \gamma^2}}{6.10482} \right), & k^2 > \gamma^2 \\ -j \frac{2}{\pi} \ln \left( \frac{W \sqrt{\gamma^2 - k^2}}{6.10482} \right), & \gamma^2 > k^2 \end{cases} \quad (\text{A.14})$$

Equation (A.14) is obtained by integrating a small-argument form of the Hankel or modified Bessel function of Equation (A.6). The type of approximation employed here is accurate within a few percent as long as the strip size does not exceed about a tenth of a wavelength.

The  $\hat{z}$ -component of the  $\bar{H}$ -field produced by a  $\hat{t}$ -component of unit magnetic current density on the strip of Figure A.1 may be obtained from the expression

$$H_z \cdot K_t(x,y) = \frac{1}{jk\eta} \hat{z} \cdot \text{grad div } \bar{F}_t \quad (\text{A.15})$$

which reduces to

$$H_z \cdot K_t(x,y) = \frac{Y}{k\eta} \frac{\partial}{\partial t} \int_{s=-W/2}^{W/2} \bar{G}(R;k,\gamma) ds \quad (\text{A.16})$$

and finally, to the closed-form expression

$$H_z \cdot K_t(x,y) = \frac{Y}{k\eta} [\bar{G}(R_1;k,\gamma) - \bar{G}(R_2;k,\gamma)] \quad (\text{A.17})$$

where

$$R_1 = \sqrt{\left(x - \frac{W}{2} \sin \phi\right)^2 + \left(y + \frac{W}{2} \cos \phi\right)^2} \quad (\text{A.18})$$

$$R_2 = \sqrt{\left(x + \frac{W}{2} \sin \phi\right)^2 + \left(y - \frac{W}{2} \cos \phi\right)^2} \quad (\text{A.19})$$

No  $\hat{z}$ -component of the  $\bar{H}$ -field is generated by a  $\hat{z}$ -component of electric current density; thus,

$$H_z \cdot J_z(x,y) = 0 \quad (\text{A.20})$$

A  $\hat{t}$ -component of  $\bar{J}$  does produce a  $\hat{z}$ -component of  $\bar{H}$ , according to

$$H_z \cdot J_t(x,y) = \left( \cos \phi \frac{\partial}{\partial x} + \sin \phi \frac{\partial}{\partial y} \right) \int_{s=-W/2}^{W/2} \tilde{G}(R;k,\gamma) ds \quad (\text{A.21})$$

For a point  $(x,y)$  away from the strip, this expression becomes

$$H_z \cdot J_t(x,y) = \int_{s=-W/2}^{W/2} \left[ \cos \phi \frac{\Delta x}{R} + \sin \phi \frac{\Delta y}{R} \right] \tilde{G}(R;k,\gamma) ds \quad (\text{A.22})$$

where

$$\Delta x = x + s \sin \phi \quad (\text{A.23})$$

$$\Delta y = y - s \cos \phi \quad (\text{A.24})$$

and

$$R = \sqrt{\Delta x^2 + \Delta y^2} \quad (\text{A.25})$$

$\tilde{G}$  is defined in Equation (A.8). In general, Equation (A.22) must be evaluated numerically.

As the observation point  $(x,y)$  approaches the strip from the outward side (as defined by ' $\phi$ '), a limiting procedure can be used to compute

$$H_z \cdot J_t(0,0) \Big|_{\text{outside}} = -\frac{1}{2} \quad (\text{A.26})$$

If  $(x,y)$  approached the strip from the inside, a similar procedure produces

$$H_z \cdot J_t(0,0) \Big|_{\text{inside}} = \frac{1}{2} \quad (\text{A.27})$$

The transverse component of the  $\bar{H}$ -field produced by a  $\hat{z}$ -component of a magnetic current density may be obtained from the expression

$$H_t \cdot K_z(x,y) = \frac{Y}{k\eta} \hat{T} \cdot \text{grad } F_z \quad (\text{A.28})$$

This reduces to

$$H_t \cdot K_z(x,y) = \frac{Y}{k\eta} \int_{s=-W/2}^{W/2} \left[ \frac{-\Delta x}{R} \sin \psi + \frac{\Delta y}{R} \cos \psi \right] \tilde{G}(R;k,\gamma) ds \quad (\text{A.29})$$

where  $\Delta x$ ,  $\Delta y$ , and  $R$  are defined in Equations (A.23) to (A.25), and  $\tilde{G}$  is defined in Equation (A.8). In general, Equation (A.29) must be evaluated numerically. For the special case when the observation point  $(x,y)$  happens to lie on the source strip, the field vanishes and

$$H_t \cdot K_z(0,0) = 0 \quad (\text{A.30})$$

The transverse H-field produced by a transverse magnetic current is given by the expression

$$H_t \cdot K_t(x,y) = \frac{1}{jk\eta} \hat{T} \cdot (\text{grad div} + k^2) \bar{F}_t \quad (\text{A.31})$$

which can be expanded to produce

$$\begin{aligned} H_t \cdot K_t(x,y) = & \frac{1}{jk\eta} \left\{ \left( -\sin \psi \frac{\Delta x_1}{R_1} + \cos \psi \frac{\Delta y_1}{R_1} \right) \tilde{G}(R_1;k,\gamma) \right. \\ & - \left. \left( -\sin \psi \frac{\Delta x_2}{R_2} + \cos \psi \frac{\Delta y_2}{R_2} \right) \tilde{G}(R_2;k,\gamma) \right\} \\ & + \frac{k}{j\eta} \cos(\psi - \phi) \int_{s=-W/2}^{W/2} \tilde{G}(R;k,\gamma) ds \end{aligned} \quad (\text{A.32})$$

where

$$\Delta x_1 = x - \frac{W}{2} \sin \phi \quad (\text{A.33})$$

$$\Delta y_1 = y + \frac{W}{2} \cos \phi \quad (\text{A.34})$$

$$R_1 = \sqrt{\Delta x_1^2 + \Delta y_1^2} \quad (\text{A.35})$$

$$\Delta x_2 = x + \frac{W}{2} \sin \phi \quad (\text{A.36})$$

$$\Delta y_2 = y - \frac{W}{2} \cos \phi \quad (\text{A.37})$$

$$R_2 = \sqrt{\Delta x_2^2 + \Delta y_2^2} \quad (\text{A.38})$$

Although the remaining integral in Equation (A.32) cannot be reduced to a closed-form expression, the approximation employed previously to convert Equation (A.11) to Equations (A.12) and (A.13) may be used for computational purposes.

The transverse  $\bar{H}$ -field produced by a  $\hat{z}$ -component of electric current density is given by

$$H_t \cdot J_z(x, y) = \hat{T} \cdot \left( \hat{x} \frac{\partial A_z}{\partial y} - \hat{y} \frac{\partial A_z}{\partial x} \right) \quad (\text{A.39})$$

which reduces to

$$H_t \cdot J_z(x, y) = \int_{s=-W/2}^{W/2} \left[ \sin \psi \frac{\Delta y}{R} + \cos \psi \frac{\Delta x}{R} \right] \tilde{G}(R; k, \gamma) ds \quad (\text{A.40})$$

where  $\Delta x$ ,  $\Delta y$ , and  $R$  are defined in Equations (A.23) and (A.25). Again, numerical integration must be used to accurately evaluate Equation (A.40). When the observation point lies on the strip, a limiting argument similar to that employed in Equations (A.26) and (A.27) can be used to show that the transverse  $\bar{H}$ -field an infinitesimal distance outside the strip is given by

$$H_t \cdot J_z(0, 0) \Big|_{\text{outside}} = \frac{1}{2} \quad (\text{A.41})$$

The transverse  $\bar{H}$ -field an infinitesimal distance inside the strip is

$$H_t \cdot J_z(0,0) \Big|_{\text{inside}} = -\frac{1}{2} \quad (\text{A.42})$$

The transverse  $\bar{H}$ -field produced by a  $\hat{t}$ -component of electric current density can be found from the expression

$$H_t \cdot J_t(x,y) = -j\gamma \hat{T} \cdot (\hat{x} \cos \phi + \hat{y} \sin \phi) A_t \quad (\text{A.43})$$

which reduces to

$$H_t \cdot J_t(x,y) = j\gamma \sin(\psi - \phi) \int_{s=-W/2}^{W/2} \tilde{G}(R;k,\gamma) ds \quad (\text{A.44})$$

The integral can also be approximated according to the procedure outlined in Equations (A.12) and (A.13), if desired. When the observation point approaches the strip, the expression vanishes. Therefore,

$$H_t \cdot J_t(0,0) = 0 \quad (\text{A.45})$$

The above equations describe the magnetic field produced by a constant electric or magnetic current density. Expressions for the electric field produced by the same sources can be found directly from the above expressions using the principle of duality. These formulas are given as follows:

$$E_z \cdot J_z(x,y) = \eta^2 H_z \cdot K_z(x,y) \quad (\text{A.46})$$

$$E_z \cdot J_t(x,y) = \eta^2 H_z \cdot K_t(x,y) \quad (\text{A.47})$$

$$E_z \cdot K_z(x,y) = 0 \quad (\text{A.48})$$

$$E_z \cdot K_t(x,y) = -H_z \cdot J_t(x,y) \quad (\text{A.49})$$

$$E_t \cdot J_z(x,y) = \eta^2 H_t \cdot K_z(x,y) \quad (\text{A.50})$$

$$E_t \cdot J_t(x,y) = n^2 H_t \cdot K_t(x,y) \quad (\text{A.51})$$

$$E_t \cdot K_z(x,y) = -H_t \cdot J_z(x,y) \quad (\text{A.52})$$

$$E_t \cdot K_t(x,y) = -H_t \cdot J_t(x,y) \quad (\text{A.53})$$

END

10-87

DITIC